Title	High speed photodiode and 90° optical hybrid for 2 μm optical communication systems
Authors	Ye, Nan
Publication date	2016
Original Citation	Ye, N. 2016. High speed photodiode and 90° optical hybrid for 2 μm optical communication systems. PhD Thesis, University College Cork.
Type of publication	Doctoral thesis
Rights	© 2016, Nan Ye. - http://creativecommons.org/licenses/by-nc-nd/3.0/
Download date	2025-06-06 17:16:04
Item downloaded from	https://hdl.handle.net/10468/3514

Title	High speed photodiode and 90° optical hybrid for 2 μm optical communication systems.
Author(s)	Ye, Nan
Publication date	2017
Original citation	Other, A. N. Year. Title. PhD Thesis, University College Cork.
Type of publication	Doctoral thesis
Rights	© 2016,Nan Ye http://creativecommons.org/licenses/by-nc-nd/3.0/
Embargo information	No embargo required

University College Cork, Ireland
Coláiste na hOllscoile Corcaigh

High speed photodiode and 90° optical hybrid for 2 μm optical communication systems

by

Nan Ye

THESIS SUBMITTED TO

NATIONAL UNIVERSITY OF IRELAND, CORK

FOR THE DEGREE OF

Doctor of Philosophy

TYNDALL NATIONAL INSTITUTE, DEPARTMENT OF PHYSICS

NATIONAL UNIVERSITY OF IRELAND, CORK

IRELAND

April 2016

RESEARCH SUPERVISOR: Brian Corbett, Frank Peters

HEAD OF DEPARTMENT: Prof. John McInerney

I declare that this thesis contains my own work and has not been submitted for another degree, either at University College Cork or elsewhere.

Nan Ye

Acknowledgements

First of all, I would like to express my great gratitude to my supervisor, Brian Corbett who kindly offers guidance, criticism, advice, and encouragement for the completion of my Ph.D. study. This work is funded by the financial support from MODEGAP FP7 EU project which is also managed by Brian Corbett. Moreover, Frank Peters, Peter O'Brien, Fatima Gunning give their help by means of suggestions and management for the device design, package, and subsystem-level test within this project.

In the photonics center, many colleges contributed their efforts to the accomplishment of my experiment work documented in this thesis. Here, I feel sincerely indebted to Hua Yang, James O'Callaghan, KoHsin Lee, Vladimir Djara, Dan O'Connell, Carmel Murphy, Mahbub Akhter, Carmel Kelleher, Krimo Khalfi, and Vince Lodge for the suggestions and process step operations during the component manufacture; John Justice, Padraic Morrissey, William Cotter for the advice regarding the simulation of the optical passive devices, Agnieszka Gocalinska for the epitaxial growth of all the photodiode and optical hybrid materials; Wei Han, Xin Wang, Noreen Nudds, Marc Rensing, Nicola Pavarelli, Yan Zhao, Cormac Eason and Brad Snyder for the circuit design, chip bonding and device package; Hongyu Zhang, Naoise MacSuibhne, Jian Zhao, Niamh Kavanagh for the assistance in the high speed characterization and Brendon Roycraft, William Cotter, Jun Lin, Ian Mathews, Aidan Daly, Farzan Gity and Zhiheng Quan for the training and advice on the measurement.

Thanks to the hands from other colleges in Tyndall, my research work has been promoted a lot. Especially, the guards at the front desk "helped" gently to let me finish the experiment no later than the mid night!

I should also appreciated the support from the partner in the project like Zhihong Li from Optoelectronics Research Centre (ORC) in the University of Southampton providing the TDFA and HaoShuo Chen in Eindhoven University of Technology (Tu/e) offering suggestions about the data fitting analysis.

Acknowledgements

Finally, mangy thanks should go to my friends and family, especially my parents ShuMei Wu and Deming Ye for selfless loving concerns, firm trust on me, and support without any complaint all over the time.

Abstract

The continued increasing use of the Internet drives the need to enlarge the transport capacity of optical networks. Current Wavelength Division Multiplexing (WDM) technologies are limited as the conventional waveband (C-band) provides a bandwidth of around 35 nm associated with the minimum-loss window of standard single mode fibre. In order to maximize the capacity using these wavelengths, more and more effort has to be exerted by the equipment providers to increase capacity and suppress cross talk between adjacent channels. To overcome this capacity saturation around 1.55 µm, the next generation optical networks require technological developments in new wavelength regions. This will not only extend the current effective transmission band but also address limitations such as loss and non-linearity of silica-core fibers. The waveband at 2 µm can be recognized as a potential candidate due to the low loss window in Hollow Core Photonic Band Gap Fibers (HCPBGF) and the gain bandwidth from Thulium Doped Fiber Amplifier (TDFA). Furthermore this waveband can take advantage of the previous research and development ideas based on 1.55 µm while extending the technologies related to materials and processing for the passive and active components. To satisfy the system-level applications at this new wave band, opto-electronics devices at 2 µm should be developed.

In this thesis, we present the building blocks regarding material optimization, device design, process development and performance characterizations of high speed photodiodes and associated 90° optical hybrids at 2 µm. To get the high speed signal from the optical carrier, the photodiode properties of 3dB-cut-off frequency, dark current and photoresponse at this wavelength have been addressed. To achieve higher transmission efficiency per single wavelength, a 90° optical hybrid needs to be developed for a balanced receiver to permit the implementation of advanced modulation formats such as Quadrature Phase Shift Keying (QPSK).

For the photodiodes, edge-coupled device based on InGaAs/InGaAs strained quantum wells shows small signal bandwidth more than 10 GHz, responsivity of around 0.38 A/W at 2 µm with a leakage of 2.55 nA at -1 V bias. The surface-illuminated photodiodes based on a strain-relaxed InGaAs absorbing layer sandwiched by AlInGaAs claddings has also been realized on InP substrate with the help of

Abstract

parabolic grading buffer. The layer thicknesses, p-doping profile as well as the sidewall passivation process were optimized. The 50-µm diameter mesa demonstrates high Radio Frequency (RF) bandwidth up to around 10 GHz while maintaining 2 µm photoresponse approaching 1 A/W with a small leakage of 0.52 µA. 15 Gbit/s eye diagram and Bit Error Rate (BER) of 10^{-12} are demonstrated with the same type of photodiode. All types of the photodiode devices have been packaged with the support from the package group for high speed test to prove the ability to work in the real optical communication system.

For the optical 90° hybrids, design of large spot size diluted waveguide, dimension optimization of 4×4 Multiple Mode Interference (MMI) coupler, and monolithic integration test structure involving hybrid and Mach-Zehnder Interferometer (MZI) are achieved. The quadrature phase condition around 2 µm was measured from the outputs of the device for the first time demonstrating a phase deviation around ±10°, Common Mode Rejection Ratio (CMRR) > 15.6 dB and an excess loss of 2.2 dB. The devices have displayed the potential to be applied in real 2 µm optical communication systems while the photodiode is also useful in gas sensing area such as carbon dioxide mapping of the atmosphere on the earth.

Content

Content

Content

List of Tables

List of Figures

List of Acronyms

A

ASE=Amplified Spontaneous Emission

AR=Anti-reflective

AC=Alternative-Current

B

BER=Bit Error Rate

BCB=Benzocyclobutene

BOE=Buffered Oxide Etchant

C

C-band=Conventional waveband

CMRR=Common Mode Rejection Ratio

CMOS=Complementary Metal–Oxide–Semiconductor

CV=Capacitance-Voltage

CPW=Coplanar Waveguide

D

DWDM=Dense Wavelength Division Multiplexing

DDR=Dual-Depletion Region

DVS-BCB=Divinyl siloxane-benzocyclobutene

DC= Direct-Current

E

EDFA=Erbium Doped Fiber Amplifier

EBR=Error bit rate

F

FP=Fabry-Perot

FSR=Free Spectral Range

List of Acronyms

G

GSMBE=Gas Source Molecular Beam Epitaxy

GS=Ground-Signal

H

HCPBGF=Hollow Core Photonic Band Gap Fibers

HVPE=Hydride Vapor Phase Epitaxy

I

ITU=International Telecommunication Union

I=In-phase

IMEC=Interuniversity Microelectronics Centre

IV=Current-Voltage

ICP=Inductively Coupled Plasma

J

K

L

LPMOCVD=Low Pressure Metal Organic Chemical Vapour Deposition

M

MMI=Multiple Mode Interference

MZI=Mach-Zehnder Interferometer

MOCVD=Metal Organic Chemical Vapour Deposition

MBE=Molecular Beam Epitaxy

MQW=Multiple Quantum Well

MZM=Mach–Zehnder Modulator

N

O

List of Acronyms

OFDM=Orthogonal Frequency Division Multiplexing

OSA=Optical Spectrum Analyser

OOK=On-Off-Key

P

PDM=Polarization Division Multiplexing

PD=Photodiode

PL=Photoluminescence

PECVD=Plasma Enhanced Chemical Vapour Deposition

PR=Photoresist

PPG= Pulse Pattern Generator

Q

QPSK=Quadrature Phase Shift Keying

QAM=Quadrature Amplitude Modulation

Q=Quadrature

QW=Quantum Well

SOI=Silicon-on-insulator

QWI=Quantum Well Intermixing

OSNR=Optical Signal to Noise Ratio

R

RF=Radio Frequency

PECVD= Plasma-Enhanced Chemical Vapour Deposition

RC= Resistance-Capacitance

S

SMF=Single Mode Fibre

SNR=Signal-to-Noise-Ratio

SSMBE=Solid Source Molecular Beam Epitaxy

SEM=Scanning Electron Microscopy

SMA= SubMiniature version A

T

TDFA=Thulium Doped Fibre Amplifier

TIA=Trans-Impedance Amplifier

TE=Transverse-Electric

TM=Transverse-Magnetic

U

UK=United Kingdom

USA=United States of America

UV=Ultraviolet

V

W

WDM=Wavelength Division Multiplexing

X

Y

Z

List of used parameters

E_g- Band gap energy of the material.

π- the ratio of a circle's circumference to its diameter, value- 3.14159.

R- the total resistance involving both 50 Ω load resistor and serial resistance of the photodiode.

C- is the total capacitance containing the natural junction capacitance and parasitic capacitance of the pad.

f_{-3dB}- -3dB cut-off frequency of the photodetector.

λ_0- free space wavelength.

k_0- free space wave number.

N_{eff}- effective index of the transmission mode.

η- coupling efficiency.

α- propagation loss.

n_r- the (effective) refractive index of the ridge waveguide.

n_c- the refractive index of the cladding region.

W_m- the physical width of the multimode waveguide.

W_e- the effective width of the multimode waveguide.

L_π- the beat length of the two lowest-order modes.

Chapter 1 Introduction

1.1 Background

The increasing bandwidth requirement from the increasing web page and video flows of the Internet is driving the increasing transmission capacity in the commercial optical networks. As a result, the current networks based on Wavelength Division Multiplexing (WDM) techniques meet a real challenge from the limited spectrum width of 35 nm in the C-band and physical boundaries such as loss and nonlinearity of the single mode fibre.

Due to the minimum-loss window of the single mode fibre and optical gain region of the Erbium Doped Fiber Amplifier (EDFA), the conventional band (C-band) which is typically used in the commercial systems and networks only provides an available bandwidth around 35 nm (1530~1565 nm). While, the latest Dense Wavelength Division Multiplexing (DWDM) standard (G.694.1) from ITU has clarified that the minimum channel spacing was down to 12.5 GHz corresponding to approximated 0.1 nm in wavelength domain around 1.55 μm [1]. Those limitations make the equipment suppliers suffer from frequency saturation as well as carrier stability maintenance which promotes the desires for another appropriate wavelength region.

Also, in the past decades, researchers concentrated on the improvement of single carrier capacity over standard Single Mode Fibre (SMF). By utilizing coherent detection, various modulation formats like Quadrature Amplitude Modulation (QAM), Polarization Division Multiplexing (PDM), and Orthogonal Frequency Division Multiplexing (OFDM) have been successfully achieved to enlarge the capacity of a single channel [2]. However, the fundamental properties of standard SMF still play the main role to limit the capacity extension potentials for the total system transmission [3]. Silica-based optical fibre suffers not only from the loss whose average value is 0.22 dB/km at 1.55 μm [4] but also from the nonlinear dependence of refractive index and the intensity of the light guided in the fibre [5]. New transmission medium needs to be introduced into the fibre to further decrease the loss and suppress the nonlinearity of the SMF.

Therefore, next generation optical networks are searching for the break-through regarding a new wavelength region as well as transporting in a new type of optical fibre to extend the numbers of available channels if the same scheme of WDM is applied.

Recently, WDM transmissions on wavelengths around 2 μm in Hollow Core Photonic Band Gap Fibers (HC-PBGFs) has attracted more attention showing the potential to satisfy the above-mentioned requirements [2]. Due to the physical properties of HC-PBGFs, an ultra-low attenuation of ~0.1 dB/km could be estimated by shifting the channels from the C-band to 2 μm [6]. Compared to standard SMF, HC-PBGFs also demonstrate much lower nonlinearity [7] as well as near-vacuum latency [8] which are appealing in long haul network deployment in addition with a gain bandwidth spanning over 100 nm from the 2 μm Thulium Doped Fibre Amplifiers [9].

To achieve large transport capacity at 2 μm optical communication system, photonic devices need to be designed and fabricated to work at this new wave band. As a core active component in charge of optical-electrical signal conversion at the receiving end, the photodiode (PD) requires optimization with respect to the high Radio Frequency (RF) working bandwidth, small leakage current under reverse bias while maintaining high photoresponse in 2 μm spectrum range. In order to further extend data transmission rate of one single channel, advanced modulation format such as Quadrature Phase Shift Keying (QPSK) or QAM should be applied on single carrier wavelength. This needs a 90° optical hybrid which should be designed around this particular wavelength to separate the In-phase (I) and Quadrature (Q) part of the signal for coherent detection. In the following sections, we are going to summarize the state-of-art works on these devices from the published literature.

1.2 Review of the state of art work

2 micron photodiodes have been widely used for carbon-based gas sensing such as environment monitoring regarding the greenhouse effect. This is due to its working range covering the absorption peak of CH_4, CO and CO_2 which is located at the spectrum region of 1.5~2.5 µm [10]. To efficiently use this special absorption property, sensor systems require high Signal-to-Noise-Ratio (SNR) specially relied on the low photodetector leakage current. This is subjected to the dislocations in the absorber due to the lattice constant misfit between the absorption layer and the substrate. In addition , due to the low loss window of HC-PBG fibres appearing around 2 µm wavelength, renewed attention on telecommunication application which has a strong connection with high speed characters of the photodiode dominated by the natural capacitance of the p-n junction and transition time of the carrier over the intrinsic layer. Optimizations mainly regarding material design and growth have been developed to decrease the leakage and improve the Radio Frequency (RF) bandwidth of the device. To summarize the evolution of the related technologies, review of the published papers will be presented in the following section with the key parameters listed in Table 1.1.

1.2.1 InGaAs photodectors at 2 µm range

Photodiodes around the region of 2 µm have been successfully achieved based on the InGaAs/InP material system by taking advantages of fast epitaxy growth rate through Hydride Vapor Phase Epitaxy (HVPE) or Metal Organic Chemical Vapor Deposition (MOCVD) associating with mature device fabrication technologies. By use of Indium-rich component to narrowly tailor the band gap of the $In_xGa_{1-x}As$ absorption layer, the photo-response of the photodiode could cover the above-mentioned wavelength band. The large lattice mismatch between the high-Indium-content intrinsic layer and the substrate was released by introducing a buffer layer by special schemes such as composition-grading [11] [12] [13] or fixed-compound interface layers [14].

For the surface normal photodetector with the input light illuminating on the top/bottom absorption window, a thick absorption region is necessary for the sufficient photo-absorption as the light propagation path is overlapped with the material growth

direction. A buffer layer is typically adopted to maintain the quality of the thick intrinsic layer by precluding the upward diffusion of the mismatched dislocations generated from the lattice-misfit between the high-indium absorption layer and the substrate. Up to now, ternary III-V materials such as InGaAs, InAsP, and InAlAs have been used to establish the buffer layer by composition grading one of the binary components.

Due to the convenience of controlling the group III ratio, the $In_{1-x}Ga_xAs$ system is widely applied for the growth of high quality epitaxial layers. Especially, to establish the buffer region for the long wavelength photodetector, changing the lattice parameter is easier to achieve by avoiding the competition of group V elements on the surface within the epitaxial process [12].

In 1986, $In_{0.72}Ga_{0.28}As/In_{0.72}Al_{0.28}As$ heterojunction photodiodes with a photoresponse cut-off wavelength extending out to 2.4 μm were fabricated by A. J. Moseley et $al.$ in Plessey Research (Caswell) Ltd. at UK by applying a ~10 μm-thick n^+ $In_{1-x}Ga_xAs$ buffer layer in a linearly composition-graded scheme until $In_{0.72}Ga_{0.28}As$. On top of the buffer, a constant-composition 4 μm-thick $In_{0.72}Ga_{0.28}As$ layer was then grown (n-type, ~1×10^{16} cm^{-3}) followed by a p-type $In_{0.72}Al_{0.28}As$ layer. 100 micron-diameter mesa devices exhibited a photoresponsivity of 1.31-1.58 A/W corresponding to the peak efficiency as high as 95 % over the 1.7-2.05 μm with the dark current down to 35 nA at the bias of -0.5 V [15]. The schematic of the device structure can be seen from Figure 1.1.
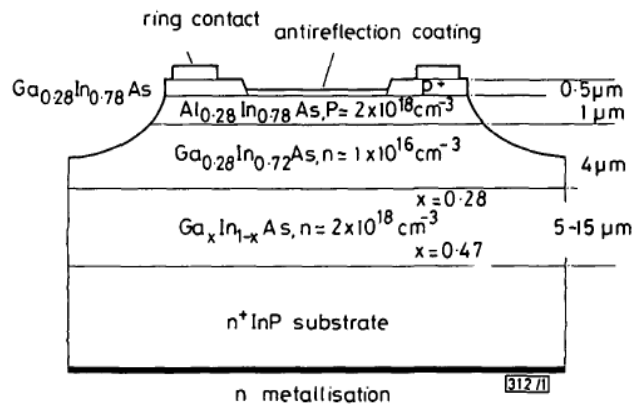
Figure 1.1: *Schematic of the cross section for the 2 micron photodiode from Plessey Research (Caswell) Ltd.* [15].

In 1988, a homojunction p-n photodiodes with spectral response as long as ~2.65 μm was achieved by Ramon U. Martinelli, *et al*. at the David Sarnoff Research Center, USA using $In_{0.82}Ga_{0.18}As$ on n-doped InP substrate. A linearly-graded $In_xGa_{1-x}As$ layer with x ranging from 0.53 to 0.81 over about 20 μm accommodated the 2% lattice mismatch between the substrate and the absorber. At room temperature, the leakage density of the device was 32 mA/cm^2 at the voltage bias of -2 V. At the same reverse bias, the 5 μm thick $In_{0.82}Ga_{0.18}As$ layer (net donor density ~2×10^{15} cm^{-3}) realized a device photoresponsity of 1.25-1.55 A/W (quantum efficiency: 70-75%) over the wavelengths of 2.1-2.6 μm [16].

Buffer layers in the $InAs_yP_{1-y}$ system has been used to achieve a smooth morphological surface [11] as well as larger band gap energy comparing to the intrinsic absorption layer which promotes the reduction of the device leakage [17]. Also, light across a broader spectral range is able to pass through the buffer layer (back side-illuminated) or the p-cap region (top side-illuminated) to be absorbed by the photodetector. The increased lattice constant along the growth sequence starting from the substrate keeps the compressive strain which protects the following epitaxy layers from cracking [18].

In 1992, involving the compound of $In_{0.72}Ga_{0.28}As$ (E_g= 0.57 eV or λ_g = ~2.2 μm) as the absorption layer, Abhay Joshi, *et al.* at the Discovery Semiconductors, USA developed the top-illuminated planar photodiodes with the buffer layer of graded $InAs_yP_{1-y}$ (n-doped) [19]. As it is demonstrated in Figure 1.2, compositionally abrupt interfaces within the buffer layer suppressed the diffusion of misfit dislocations to minimize the unintentional background doping of the intrinsic layer [20, 21]. Another $InAs_{0.33}P_{0.67}$ layer was grown on top of the absorber to achieve the anode. The active region was defined by p+-Zn diffusion and then passivated with a coating of Silicon Nitride. With material growth optimization, the device could present a diode ideality factor of ~1.3 at 20 °C and an unintentional background doping of ~8×10^{15} cm^{-3} in the intrinsic layer. The leakage density of the 50 μm diameter mesa was ~50.93 mA/cm^2 at -5 V and the photoresponsivity was up to 1.2 A/W (quantum efficiency: ~72 %) at the input wavelength of 2.05 μm [21, 22].
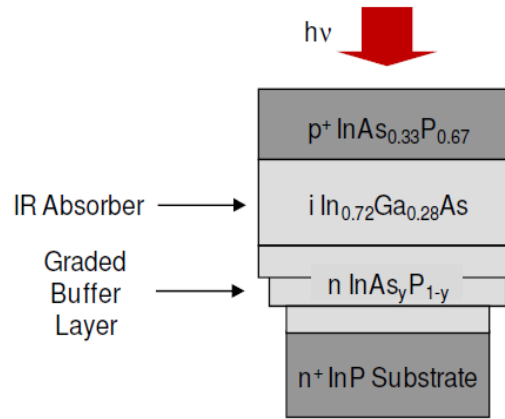
Figure 1.2: *Schematic of the cross section for the 2 micron photodiode from Discovery Semiconductors, Inc.* [19].

With the $In_{0.82}Ga_{0.18}As$ content in the intrinsic layer, M. D'Hondt, *et al*. at the University of Ghent-Interuniversity Microelectronics Centre (IMEC), Belgium fabricated the planar photodiode similar to the structures from Reference No.19 by use of 4 μm thick $InAs_yP_{1-y}$ buffer layer graded in composition over 20 steps from y=0 to y=0.61. The not-intentionally-doped device with 2-μm thick $In_{0.82}Ga_{0.18}As$ absorbing layer resulted in a response of 1.11 A/W at 2 μm corresponding to a quantum efficiency of 66 % [23]. One buffer layer may not be sufficient to fully suppress the device dark current generating from the lattice mismatching, which expects for more complex strain-releasing scheme. By the combination of a 2.5 μm thick $InAs_yP_{1-y}$ content-graded buffer (y is from 0 to 0.5), 1 μm thick fixed-component $InAs_{0.5}P_{0.5}$ buffer and 0.9 μm thick superlatice strained InAsP/InGaAs buffer followed by the 4 μm $In_{0.8}Ga_{0.2}As$ absorber, M.A. di Forte-Poisson in the Laboratoire Central de Recherches Thomson-CSF, France achieved the 2.4 μm InGaAs/InAsP/InP double-heterojunction photodiode with the epitaxial layers grown by Low Pressure Metal Organic Chemical Vapour Deposition (LPMOCVD) on n+-doped InP substrate. The planar type device displayed a leakage density of 0.8 mA/cm^2 (300 K) at -1 V bias and unintentional doping level of 2×10^{16} cm^{-3} deduced from the CV test results [24].

$In_xAl_{1-x}As$ can be approximately lattice-fitted to $In_xGa_{1-x}As$ under the same content of indium (x) with a bandgap energy larger than the $InAs_yP_{1-y}$ material system which is more suitable for the back-side-illuminated photodetector. The lattice constant of this system could be adjusted to the range matched to InP and to InAs [13].

In addition, applying this material system can successfully get rid of the related issue of controlling the fluxes of the V component for accurate epitaxy growth [25].

In 2008, with a 3 μm thick n-doped linearly-graded $In_xAl_{1-x}As$ (x is from 0.53 to 0.8) as the buffer layer on (100) oriented semi-insulating (S. I.) InP substrate, a 2.42 micron mesa type photodetector working at room temperature has been successfully developed by Yonggang Zhang, *et al.* in Shanghai Institute of Microsystem and Information Technology, Chinese Academy of Sciences. Hetero-junction structure involving 2.5-μm thick $In_{0.8}Ga_{0.2}As$ absorber and $In_{0.8}Al_{0.2}As$ cap layer were grown by Gas Source Molecular Beam Epitaxy (GSMBE). When it is biased at -10 mV, the sample leakage density is 8.15×10^{-2} mA/cm^2 with a doping level of 1×10^{17} cm^{-3} in the absorption layer at 290 K [13]. The schematic of the device in cross section view is shown in Figure 1.3 as follows,
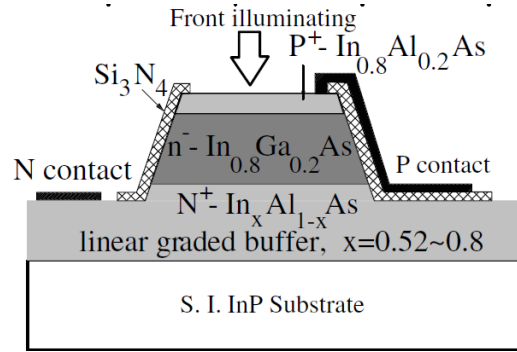
Figure 1.3: *Schematic for the 2 micron photodiode based on InAlAs buffer from the group in Shanghai Institute of Microsystem and Information Technology, Chinese Academy of Science* [13].

Optimizations were carried out on several aspects such as using high-level Be doping in the composition-graded buffer layer rather than Si, applying n-on-p structure for launching the light close to the depletion region in the case of back-illumination [26], increasing the indium content up to 0.9 in both absorption and cap layer to extend the cut-off wavelength as long as 2.9 μm [27], utilizing new buffer schemes like continuous-grading and step-grading for better material metamorphy [28]. In 2014, with the similar linearly-graded buffer structure adjusting the Al mole fraction from 0.52 to 0.83 and grown by Solid Source Molecular Beam Epitaxy (SSMBE), Yetkin Arslan, *et al.* from the Middle East Technical University, Turkey demonstrated a wet-

etched mesa photodiode with a cut-off wavelength of 2.6 μm, leakage density of 4.8×10^{-4} mA/cm^2 (25 mV, 180 K) and quantum efficiency of ~52 % at 2.5 μm. The thickness of the buffer layer was reduced to 1.5 μm which was effective to suppress the defect doping density down to 9×10^{14} cm^{-3} in the intrinsic absorption layer [29].

As mentioned above, most of the epitaxy layers for 2 μm photodiode were grown on InP substrate. If the GaAs substrate is considered, the epitaxial layers in InGaAs material system would face the challenge of larger lattice mismatch within the intrinsic absorber and the substrate. However, it is still very attractive to obtain the devices on such substrate due to the robust mechanical property, high crystalline quality, as well as low cost of the GaAs substrate. Especially, commercial gallium arsenide substrate is able to reach as large as 6 inch allowing larger product volume to further reduce the production cost per device unit[30].

In 2002, P. Merken *et al*. from IMEC, Belgium published a homo-junction In$_{0.78}$Ga$_{0.22}$As n-on-p photodiode on top of 5 μm Al$_{0.22}$In$_{0.78}$As buffer on a 3 inch semi-insulating GaAs substrate grown by Molecular Beam Epitaxy (MBE). Back-side illuminated 320×256 focal-plane array were fabricated with the single 25×25 μm^2 pixel displaying a dark current in the order of $10^{-8} \sim 10^{-7}$ A (leakage density–1.6~16 mA/cm^2) at the bias of -0.1 V at 300 K and responded to those wavelengths from 1.3 to 2.3 μm [31]. Later in 2003, standard metamorphic InGaAs or IR-transparent InAlAs buffers were applied with different thicknesses varying from 2.3 to 7.3 μm demonstrating the leakage reducing with wider-gap buffer as well as thicker buffer thickness which are associated with the accommodation of those generation-recombination centers referring to threading dislocation defects. Also, as it is shown in Fig. 1.4, the active junction structure adopted a p-graded layer following 2 μm InGaAs absorption region were optimized for the applications in the temperature of 250 K and sandwiched by highly doped n and p cap. For the n-on-p device with 7.3 μm thick InAlAs buffer, the sensitive range could be extended up to 2.4 μm with a quantum efficiency of >30% at 2.0 μm and 46% at 1.6 μm without anti-reflective (AR) coating [14].
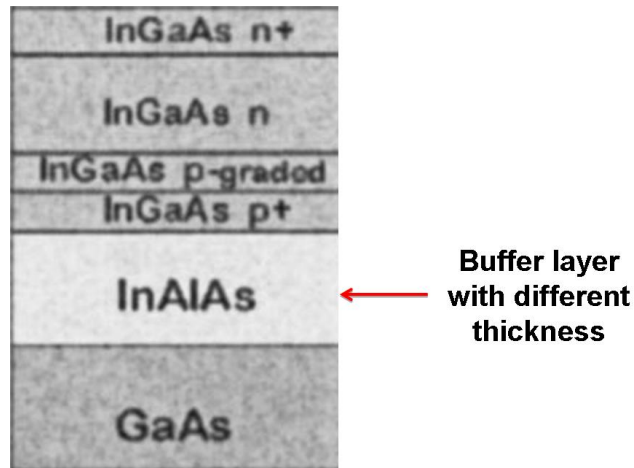
Figure 1. 4: *Schematic for the n-on-p structure of the 2µm photodiode based on InAlAs buffer from IMEC* [14]

In 2014, L. Zhou, *et al.* in Shanghai Institute of Microsystem and Information Technology, Chinese Academy of Sciences released a 2.6 µm $In_{0.83}Ga_{0.17}As/In_{0.83}Al_{0.17}As/In_xAl_{1-x}As$ photodetector grown on n+-type GaAs substrate by GSMBE system. To accommodate the +5.9 % lattice misfit between the intrinsic absorption layer and the substrate, a 1.9 µm thick continuously-graded $In_xAl_{1-x}As$ (x is from 0.1 to 0.83) buffer in combination with a 0.6 micron constant-composition $In_{0.83}Al_{0.17}As$ buffer were utilized as that is shown in Figure 1.5. The wet-etched mesa device showed a dark current density of 3.23 mA/cm^2 at -10 mV as well as 50% cut-off wavelength as long as 2.58 µm at 300 K [32].
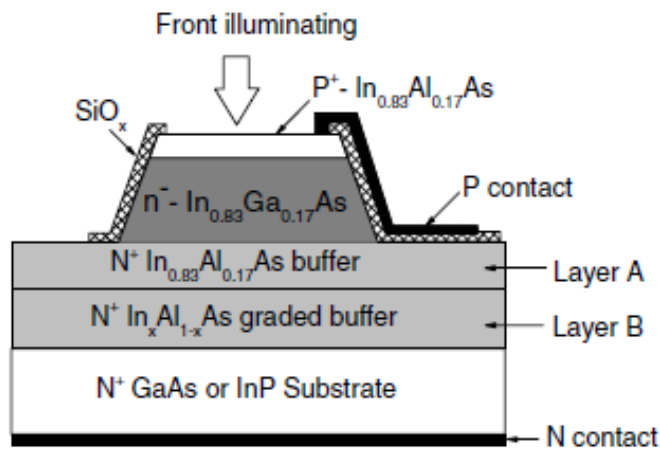
Figure 1.5: *Schematic for the $In_{0.83}Ga_{0.17}As/In_{0.83}Al_{0.17}As/In_xAl_{1-x}$ As surface normal photodiode* [32].

One of the most attractive properties of the InGaAs material is the large carrier mobility which plays the main role for the high speed detector requiring short traverse time across the intrinsic region under reverse bias.

On 2008, Abhay Joshi and Don Becker in Discovery Semiconductors, USA reported the top-illuminated $In_{0.72}Ga_{0.28}As/InAs_yP_{1-y}$ photodiode with the 3-dB cut-off frequency up to 6 GHz in use of the scheme of Dual-Depletion Region (DDR). A photo-responsivity of 1.34 A/W at 2.05 μm wavelength and a dark current of 400 nA were measured at -5 V bias [33]. Later, a 2 micron high speed photodiodes based on extended InGaAs was also developed in the same company on the InP substrates (2012). The dislocation defects in the $In_{0.72}Ga_{0.28}As$ absorber was qualified by an unintentional background doping of $8 \times 10^{15}\,cm^{-3}$ leading to a diode ideality factor of <1.3 at room temperature. By the integration of the trans-impedance amplifier (TIA), the detector demonstrated a small signal bandwidth of 6 GHz mainly suffering from the capacitance of the p-i-n junction (0.45 pF) [10].

1.2.2 2 μm photodiodes based on the material containing Sb

The band edge of the materials containing Sb could be extended to longer wavelengths. The working wavelength of GaInAsSb can cover the near-and mid-infrared wavelengths ranging from 1.7 to 4.3 μm while maintain lattice-matching property to the GaSb substrates.

In 2006, M. H. M. Reddy, *et al*. in the University of Iowa, USA demonstrated a photodetector with a 2 μm-thick $Ga_{0.79}In_{0.21}As_{0.19}Sb_{0.81}$ intrinsic layer grown by MBE. An unintentionally p-doping level of ~5×10^{16} cm^{-3} in the intrinsic layer, 90% of the maximum response over a range of 2-2.4 μm and a maximum responsivity of 1.19 A/W between 2.2 and 2.35 μm related to a quantum efficiency of 65 % were obtained. [34]. H. Shao, *et al*. in Columbia University, USA published a GaInAsSb/AlGaAsSb heterojunction p–i–n photodetectors grown by solid source molecular beam epitaxy (year 2008). Valved crackers were introduced to further release the lattice-matching between GaInAsSb absorber and the GaSb substrates. A rectangular mesa device (320 μm×140 μm) with a $Al_{0.25}Ga_{0.75}As_{0.03}Sb_{0.97}$ (0.5 μm) as the n-type layer (5×10^{17} cm^{-3}) and a 2.5 µm unintentionally-doped (p-type, 1×10^{16} cm^{-3}) $In_{0.24}Ga_{0.76}As_{0.21}Sb_{0.79}$ as an intrinsic layer were fabricated displaying a breakdown voltage of 32 V, 50 % cut-off wavelength up to 2.57 µm and a leakage density of 4.0 mA/cm^2 at room temperature. The peak responsivity from the top side illumination is 1.16 A/W at the wavelength of 2.36 µm corresponding to an external quantum efficiency of 63 % [35]. B. Liang, *et al*. from Carleton University, Canada developed a 2-2.8 μm vertically stacked multiple-junction PIN GaInAsSb/GaSb photodetectors in 2011. The intrinsic absorption region consisted of five periods p$^+$/p$^-$/n$^+$ $Ga_{0.7}In_{0.3}As_{0.273}Sb_{0.727}$ based on GaSb (100) substrate with a 200 nm GaSb buffer layer in between. A response quantum efficiency (RQE，product of internal quantum efficiency and external quantum efficiency) of 52-69 % was obtained [36].

Benefiting from the lattice-matching property of the InGaAs/GaAsSb type II quantum wells, the high epitaxy growth quality can be achieved for the long wavelength photodetectors based on InP substrate. In addition, longer wavelength absorption is possible due to the indirect transition of the light-induced electrons to the conductive band of the adjacent layers which achieves an effective bandgap reduction compared to the native bandgaps of the well and barrier material [37].

In 2009, Hiroshi Inada *et al.* from the transmission Devices R&D Laboratories, Japan exhibited a p-i-n photodiode covering the wavelengths up to 2.5 μm with a 250-pair InGaAs (5nm)/GaAsSb (5nm) type II quantum wells structure as the intrinsic layer grown on S-doped InP (100) substrate by solid source MBE. A 1.3 μm thick InGaAs layer was used as the cap layer. A planar circular mesa device in the diameter of 140 μm showed a leakage density of 0.92 mA/cm^2 (140 nA, -1 V) and responsivity of 0.6 A/W at 2.2 μm [38]. Later on 2011, with 100-pairs $In_{0.34}Ga_{0.66}As$ (7 nm)/$GaAs_{0.25}Sb_{0.75}$ (5 nm) strain compensated type-II quantum wells as the intrinsic absorption layer, Baile Chen, *et al*. in the University of Virginia, USA presented a InP-based p-i-n photodiode grown by MBE with the response extended to 3.4 μm wavelength. The device dark current density was suppressed to 9.7 mA/cm^2 at the bias of −0.5 V in the temperature of 290 K [39]. A new strain compensation scheme was proposed involving one 5 nm $GaAs_{0.35}Sb_{0.65}$ layer sandwiched by two 5 nm $In_{0.75}Ga_{0.25}As$ layers as the compressive-strain quantum well (QW) which is compensated by two 3.4 nm tensile-strain $In_{0.2}Ga_{0.8}As$ layers. This leads to a small device leakage density of 2.6 mA/cm^2 in the same temperature and bias condition (−0.5 V, 290 K) benefiting from a thinner absorption region [40]. In 2012, Fujii. Kei, *et al.* at the Semiconductor Technologies R&D Laboratories, Japan reported pin-PDs with the lattice-matched $In_{0.53}Ga_{0.47}As$ (5 nm)/$GaAs_{0.51}Sb_{0.49}$ (5 nm) type-II QWs grown by MOCVD on InP (100) substrates (S-doped). By using a InP cap layer, the surface leakage density was suppressed to 9.0 μA/cm^2 (233 K). A peak wavelength of 2.52 μm, a maximum external quantum efficiency of 48 % (450-pairs QWs) at 2 micron wavelength, and an ideality factor of 1.2 were obtained [41].

Silicon photonics platform is more suitable for massive production benefiting from the CMOS compatible fabrication process. Integration of absorption region on this platform can achieve the photodetectors at a low cost in the photonics integrated circuit.

In 2011, Nannicha Hattasan *et al.* in Ghent University presented the first GaSb-based $Ga_{0.79}In_{0.21}As_{0.19}Sb_{0.81}$/$InAs_{0.91}Sb_{0.09}$ p-i-n photodiodes heterogeneously integrated on silicon-on-insulator (SOI) waveguide circuits in use of the adhesive bonding agent of DVS-BCB (Benzocyclobutene). A dark current density of 186 mA/cm^2 at -0.1 V and a responsivity of 0.44 A/W at 2.29 μm (external quantum efficiency ~24 %, room temperature) were successfully realized [42]. Then, Ruijing Wang from the same affiliation pulished the work further on the year of 2014 that the

InP-based InGaAs (2.6 nm)/GaAsSb (2.9 nm) type-II quantum well photodiodes was integrated on a silicon photonics integrated circuit with the same bonding technology. By excluding the coupling efficiency of −11 dB (2.3 μm), a responsivity of 1.2 A/W at 2.32 μm was obtained corresponding to a quantum efficiency of 65 %. The dark current of this device was 12 nA under −0.5 V bias at room temperature. [43]

The main properties of several representative photodiodes (above-mentioned) are listed in Table 1.1 as follows,

Table 1.1: Main properties of several representative 2 µm photodiodes published until recently

Author and affiliation	Substrate	Material (Intrinsic absorber/cap for bulk, well/barrier for quantum well)	Buffer layer (Thickness)	Calculated leakage density (mA/cm2)	Peak wavelength quantum efficiency	Absorption cut-off wavelength (nm)	Published time	Reference
A. J. Moseley, et al., Plessey Research (Caswell) Ltd., UK	n+InP	$In_{0.72}Ga_{0.28}As$(4µm thick)/$In_{0.72}Al_{0.28}As$	linearly composition-graded $In_{1-x}Ga_xAs$ (10 µm)	0.45 (-0.5 V)	95%	2400	1986	[15]
Ramon U. Martinelli, et al, David Sarnoff Research Center, USA	n+InP	$In0.82Ga0.18As$ (5µm thick)/$In0.82Ga0.18As$	linearly-graded $In_xGa_{1-x}As$ (20 µm)	32 (-2 V)	75%	2650	1988	[16]
Abhay Joshi, et al. Discovery Semiconductors, USA	n+InP	$In0.72Ga0.28As$ /$InAs_{0.33}P_{0.67}$	abruptly-graded InAsyP1-y (n-doped)	~50.93 (-5 V)	72 % (caculated)	2200	2012	[21][22]
Yonggang Zhang, et al. in Shanghai Institute of Microsystem and Information Technology, Chinese Academy of Sciences.	semi-insulated InP substrate	$In_{0.3}Ga_{0.2}As/In_{0.8}Al_{0.2}As$(2.5 µm)	n-doped linearly-graded $In_xAl_{1-x}As$ (3 µm)	8.15 ×10-2 (-10 mV)		2420	2008	[13]
Yetkin Arslan, et al. from the Middle East Technical University, Turkey	semi-insulated GaAs substrate (3 inch)	$In_{0.78}Ga_{0.22}As/$	linearly-graded $In_xAl_{1-x}As$	4.8×10^{-4} (-25 mV, 180 K)	~52 %	2600	2014	[25]
H. Shao, et al. in Columbia University, USA	GaSb	In0.24Ga0.76As 0.21Sb0.79 (2.5 µm thick)/ Al0.25Ga0.75A s0.03Sb0.97(0.5 µm thick)		4	63%	2570	2008	[35]
B. Liang, et al. from Carleton University, Canada	GaSb	$Ga_{0.7}$ $In_{0.3}As_{0.273}$ $Sb_{0.727}$			69%	2800	2011	[36]
Hiroshi Inada et al. from the transmission Devices R&D Laboratories, Japan	InP	250-pair InGaAs (5nm)/ GaAsSb (5nm) type II quantum wells/ InGaAs (1.3 µm thick)		0.92 (-1 V)			2009	[38]
Baile Chen, et al. in the University of Virginia, USA	InP	100-pairs $In_{0.34}Ga_{0.66}As$ (7 nm)/$GaAs_{0.25}Sb_{0.75}$ (5 nm) strain compensated type-II quantum wells		9.7 (−0.5 V, 290K)		3400	2011	[40]
Fujii. Kei, et al. at the Semiconductor Technologies R&D Laboratories, Japan	InP	$In_{0.53}Ga_{0.47}As$ (5 nm)/$GaAs_{0.51}Sb_{0.49}$ (5 nm) type-II QWs		9×10-2 (233 K)	48% (450-pairs QWs)		2012	[41]
Nannicha Hattasan et al. in Ghent University	SOI	GaSb- based $Ga_{0.79}In_{0.21}As_{0.19}Sb_{0.09}/InAs_{0.91}Sb_{0.09}$ 0.88		186 (-0.1 V)	24%		2011	[42]

35

1.2.3 90 ° optical hybrid based on the MMI structures

Based on the the multimode interference (MMI) proterty of the multimode waveguide, optical coupler can be realized by connceting its input/output ports with multiple single-mode waveguides.

It can take the advantage of the planar ridge waveguide geometry which is easy to be integrated with other active or passive devices. Simple rectangular structure provides more facility for the design optimization and more tolerance for device manufacture. Moreover, benefiting from the self-imaging property of the interference section (multimode waveguide), balanced output power and fixed phase relationship between output ports are obtained. Therefore, a single 4×4 general-interference MMI coupler is able to realize the 90° optical hybrid function demonstrating quadrature phase relations and even output power when any two asymmetric entrance waveguides are selected as the input. In addition, this type of device exhibits special abilities involving non-sensitive to wavelength and temperature stability which suit well to be integrated with the balanced photodiodes for the detection in coherent optical transmission systems.

InP-based III-V material system permits a natural vertical mode confinement by the heterogeneous semiconductor epitaxy layers grown by MOCVD. Mainwhile, horizontal definition of the waveguide geometry is able to be realized in planar process involving UV lithography and dry etching which is suitable for the hybrid based on MMI coupler schemes. In 1993, a GaInAsP/InP 4×4 MMI device was exhibited to achieve 90° optical hybrid function by E. C. M. Pennings from Philips Research Laboratories, The Netherlands. The optimized devices displayed an output power distribution of 97:99:104:99, insertion loss $\leq$ 1 dB, ± 3° deviation from phase quadrature condition and polarization-insensitive character at 1523 nm [44]. Also, new scheme has been proposed to further simplify the access such as releasing waveguide intersection at the output. On 2009, Seok-Hwan Jeong and Ken Morito from Fujitsu Laboratories Ltd., Japan presented an optical 90° hybrid on InP substrate based on MMI devices with no waveguide intersection at the output. As it is shown in Figure 1.6, this device was constructed by a 2×4 MMI coupler combining a 2×2 MMI coupler through a $-\pi/4$ phase shifter to any paired output ports of the 2×4 MMI coupler.

Experiment results exhibited a quadrature phase behavior cross a 94 nm wavelength region around 1550 nm. [45, 46]
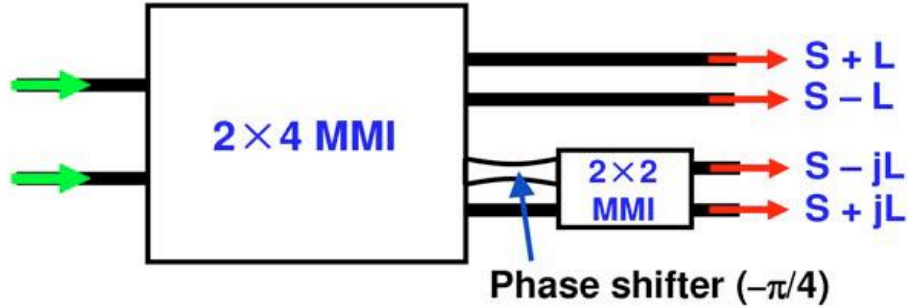
Figure 1.6: *Schematic for the 90° optical hybrid consisting of a 2×4 MMI coupler, a phase shifter and a 2×2 MMI coupler* [45, 46].

Later in 2011, a novel GaInAsP/InP 90° optical hybrid were exhibited from the same group by applying a linearly-tapered 2×4 MMI coupler directly combined with a 2×2 MMI at the paired output waveguides (Figure 1.7). A short device length of ~227 μm without any waveguide intersections and a phase deviation from quadrature condition of $< \pm 5°$ covering the C-band were obtained [47].
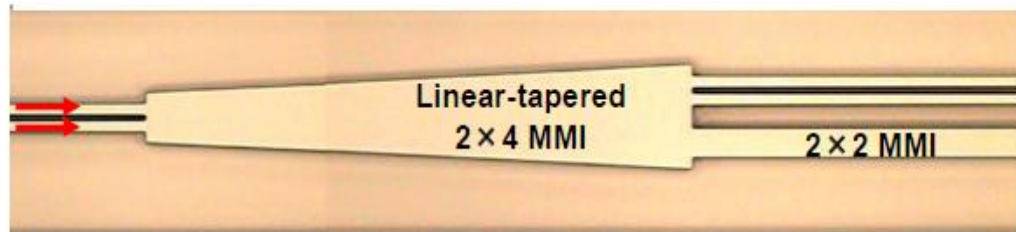
Figure 1.7: *Schematic for the novel 90° optical hybrid consisting of a 2×4 MMI coupler and a 2×2 MMI coupler* [47].

Integrated 90° optical hybrid based on MMI coupler structure in silicon-on-insulator (SOI) material gains not only the merit of high device compactness benefitting from the large refractive index contrast between the silicon waveguide and its surrounded claddings (SiO_2 and Air) but also the Complementary Metal–Oxide–Semiconductor (CMOS) process in silicon foundries for massive production at a low cost. In 2008, compact optical 90°-hybrid devices based on fully passive 4×4 multimode interference couplers were achieved by K. Voigt, *et al*. from Technische Universität Berlin,

Germany in use of rib waveguide SOI technology. The 2-µm deep nominal rib was defined by applying reactive-ion etching on the bonded and etch-back material. For the fabricated devices, 1-dB excess loss penalty, stable quadrature-phase property, temperature-insensitive behavior were observed all over the C-band wavelengths [48]. Later on the year of 2011, the same group developed a 90° optical hybrid based on the same scheme using 200 mm SOI wafers (silicon-0.22 μm, buried oxide-2 μm) in nanowire technology. With 248 nm Deep-UV-lithography and decoupled plasma source etching, the 10 μm × 200 μm fabricated device showed an excess loss smaller than 0.5 dB and phase error within 5° around 1550 nm [49].

1.3 Summary

Until now, the photodiodes with the absorption response wavelength up to around 2 micron have been realized in InGaAs and Sb-containing material on various platforms such as InP, GaAs, etc. Comparing to the Sb-containing system, manufacture process turns to be mature for the InGaAs devices which results in more attentions for the industry level applications. High indium-content can achieve large electron mobility promoting the transmission speed which is suitable for the high speed applications such as the receiver of the optical communication system. As the relatively-small lattice-constant difference between the intrinsic layer and the substrate, high-quality epitaxial growth of $Ga_xIn_{1-x}As$ layers on InP substrate is easier to be achieved by the method of MOCVD. While, the thickness of the linear-grading $Ga_xIn_{1-x}As$ is typically much more than 1 micron which would take long growth time limiting the production efficiency. Therefore, to realise the key aim of obtaining the photodiode with a high bandwidth as well as high responsitiy at 2 µm wavelength used for the practical communucation, more work should be focused on maintaining the efficient suppression for the diffusion of the mis-fit dislocations into the InGaAs intrinsic layer while finding the new buffer scheme to reduce the time cost of the buffer growth .

At this moment, most of the 90° optical hybrid based on the MMI devices were fabricated around the wavelength band at 1550 nm for the optical communication systems. New waveguide structure would be proposed to maintain the single mode property and optimizations on the device dimension should also be considered to obtain the hybrid function around the new wavelength region.

This thesis would present the theoretical simulation, design, optimization, device fabrication and characterizations on solving the above-mentioned challenges to obtain the high speed photodiodes and 90° optical hybrid working around 2 µm.

1.4 Structure of this thesis

In this document, review of the published works about the 2-µm wavelength photodiode and 90° optical hybrid are presented in the Chapter 1. In Chapter 2, we discuss the theories used in the design and characterization of the material exhibiting the bandgap around 2 µm wavelengths. Fabrication and characterization process of the optoelectronic devices will also be generally presented. In Chapter 3, we demonstrate the design, fabrication as well as characterization of both the edge-coupled photodiodes based on strained quantum wells and surface-normal type photodectors in strain-relaxed InGaAs bulk material with a photoresponse up to 2-µm wavelength region. In Chapter 4, design, optimization and characterization of a 2-µm wavelength 90° optical hybrid based on the 4×4 MMI coupler are displayed. In Chapter 5, the design and assembly of the module for packaging the high speed ridge waveguide and surface-illuminated photodetectors are explained with the evaluation results of the large signal test. Finally, the above-mentioned works as well as the further improvement on the devices are summarized in Chapter 6. The final section would be the appendix demonstrating the fabriaction process flows for the high speed top-illuminated mesa type photodiode on n-doped InP substrate as well the balanced photodetector based on the paired mesa detectors in serial conection on semi-insulating InP substrate for the applications around 2-µm wavelength.

1.5 References

[1] http://www.itu.int/rec/T-REC-G.694.1-201202-I/en

[2] H. Zhang, N. Kavanagh, Z. Li *et al.*, "100 Gbit/s WDM transmission at 2 µm: transmission studies in both low-loss hollow core photonic bandgap fiber and solid core fiber," *Optics Express*, vol.23, no.4, pp.4946-4951, 2015.

[3] A. D. Ellis, D. Rafique, and S. Sygletos, "Capacity in fiber optic communications the case for a radically new fiber," *IEEE Phot. Conference*, Arlington, 2011, pp. TuN1.

[4] http://www.cisco.com/c/en/us/support/docs/optical-networking/ons-15454-sonet multiservice-provisioning-platform-mspp/27042-max-att-27042.html

[5] G. Agrawal, *Nonlinear fiber optics*. 4 th ed, Elsevier/Academic Press, Oxford, UK, 2007.

[6] P. J. Roberts, F. Couny, H. Sabert, *et al*, "Ultimate low loss of hollow-core photonic crystal fibres," *Optics Express*, vol.13, no.1, pp. 236-244, Dec. 2005

[7] C. J. Hensley, D. G. Ouzounov, A. L. Gaeta, *et al.*, "Silica-glass contribution to the effective nonlinearity of hollow-core photonic bandgap fibers," *Optical Express*, vol.15, 3507-3512 (2007).

[8] F. Poletti, N. Wheeler, M. Petrovich, *et al.*, "Towards high-capacity fibre-optic communications at the speed of light in vacuum," *Nature Photonics*, vol.7, no.4, pp.279-284, 2013.

[9] A. M. Heidt, Z. Li., and D. Richardson *et al.*, "High power diode-seeded fiber amplifiers at 2 µm–from architectures to applications," *IEEE Journal of Selected Topics in Quantum Electronics*, vol.20, no.5, pp. 3100612, Step.2014.

[10] J. de Vries, E.C. Laan, I. Escudero-Sanz, *et al.*, "From OMI and SCIAMACHY to TROPOMI: recent improvements in sun backscatter atmospheric composition measurements," in *joint EUMETSAT meteorological satellite conference and American meteorological society satellite meteorology & oceanography co*, Amsterdam, Netherlands, Sept. 2007.

[11] J. Kirch, T. Kim, J. Konen, *et al.*, "Effects of antimony (Sb) incorporation on MOVPE grown InAsyP1−y metamorphic buffer layers on InP substrates," *Journal of Crystal Growth*, vol.315, no.1, pp.96-101, 2011.

[12] A. Gocalinska, M. Manganaro and E. Pelucchi, "Suppression of threading defects formation during Sb-assisted metamorphic buffer growth in InAs/InGaAs/InP structure," *Applied Physics Letters*, vol.100, no.15, p.152112, 2012.

[13] Y. Zhang, Y. Gu, Z. Tian, *et al.*, "Wavelength extended 2.4μm heterojunction InGaAs photodiodes with InAlAs cap and linearly graded buffer layers suitable for both front and back illuminations," *Infrared Physics & Technology*, vol.51, no.4, pp.316-321, 2008.

[14] L. Zimmermann, J. John, S. Degroote, *et al.*, "Extended wavelength InGaAs on GaAs using InAlAs buffer for back-side-illuminated short-wave infrared detectors," *Applied physics letters*, vol.82, no.17, pp.2838-2840, 2003.

[15] A. Moseley, M. Scott, A. Moore, *et al.*, "High-efficiency, low-leakage MOCVD-grown GaInAs/AlInAs heterojunction photodiodes for detection to 2.4μm," *Electronics Letters*, vol.22, no.22, p.1206, 1986.

[16] R. U. Martinelli1, T. J. Zamerowski1 and P. A. Longeway, "2.6 μm InGaAs photodiodes,". *Applied physics letters*, vol.53, no.11, pp.989-991,1988.

[17] V. S. Ban, G. Erickson, S. Masonm *et al.*, "Room-Temperature Detectors for 800-2600 nm Based On InGaAsP Alloys,". in *Orlando Symposium International Society for Optics and Photonics*, Sep. 1989, pp.151-164.

[18] A. Joshi, and S. Datta, "Low-noise UV-to-SWIR broadband photodiodes for large-format focal plane array sensors,". In *Defense, Security, and Sensing International Society for Optics and Photonics*, 2012, pp. 838507.

[19] A. Joshi, G. Olsen, S. Mason, *et al.*, "Near-Infrared (1-3 μm) InGaAs Detectors and Arrays: Crystal Growth, Leakage Current, and Reliability," in *Optical Methods in Atmospheric Chemistry SPIE*, vol.1715, 1992, pp.585-593.

[20] A. Joshi, V. Ban, S. Mason, and M. Lange, "512 and 1024 Element Linear InGaAs Detector Arrays for Near-Infrared (1-3μm) Environmental Sensing," in *Infrared Detectors: State of the Art SPIE*, vol.1735, San Diego, USA,1992, pp.287-295.

[21] A. Joshi and S. Datta,"High-speed, large-area, p-i-n InGaAs photodiode linear array at 2-μm wavelength," in *Defense, Security, and Sensing*, the international society for optics and photonics (SPIE), Maryland, USA, pp.83533D, 2012

[22] A. Joshi, "Developments in high performance photodiodes," *Photonics Conference (IPC) IEEE*. 23-27 Sept., 2012.

[23] M. D'Hondt ; I. Moerman and P. Demeester, "Dark current optimisation of 2.5 μm wavelength, 2% mismatched InGaAs photodetectors on InP,". in *International Conference on Indium Phosphide and Related Materials (IPRM)*, 1998, pp. 489-492.

[24] M. A. di Forte-Poisson, C. Brylinski, J. Di Persio, *et al.*, "$Ga_{1-x}In_xAs/InAs_yP_{1-y}/InP$ photodiodes for the 1.6 to 2.4 μm spectral region grown by low pressure MOCVD," *Journal of crystal growth*, vol.124, no.1, pp.782-791, 1992.

[25] K. R. Linga, G. H. Olsen, V. S. Ban, *et al.*, "Dark current analysis and characterization of $In_xGa_{1-x}As/InAs_yP_{1-y}$ graded photodiodes with x>0.53 for response to longer wavelengths (>1.7 μm)," *Journal of Lightwave Technology*, vol.10, no.8, pp.1050–1055, Aug. 1992.

[26] Y. Zhang, Y. Gu, Z. Tian, *et al.*, "Wavelength extended InGaAs/InAlAs/InP photodetectors using n-on-p configuration optimized for back illumination," *Infrared Physics & Technology*, vol.52, no.1, pp.52-56, 2009.

[27] C. Li, Y. Zhang, K. Wang *et al.*, "Distinction investigation of InGaAs photodetectors cutoff at 2.9 μm", *Infrared Physics & Technology*, vol.53, no.3, pp.173-176, 2010.

[28] S. Xi, Y. Gu, YG. Zhang *et al.*, "Effects of continuously graded or step-graded $In_xAl_{1-x}As$ buffer on the performance of InP-based $In_{0.83}Ga_{0.17}As$ photodetectors," *Journal of Crystal Growth*, vol.425, pp.337-340, 2015.

[29] Y. Arslan, F. Oguz, and C. Besikci. "Extended Short Wavelength Infrared $In_{0.83}Ga_{0.17}As$ Focal Plane Array," *Journal of Quantum Electronics IEEE*, vol.50, no.12, pp.957-964, 2014.

[30] L. Zimmermann, J. John, S. Degroote, *et al.*, "Extended wavelength InGaAs on GaAs using InAlAs buffer for back-side-illuminated short-wave infrared detectors," *Applied physics letters*,vol.82, no.17, pp.2838-2840, 2003.

[31] P Merken, L Zimmermann, J John, *et al.*, "Extended-wavelength InGaAs-on-GaAs infrared focal-plane array," *Electronics Letters*,vol.38, no.12, pp.588-590, 2002.

[32]. L.Zhou, Y.G. Zhang, X.Y. Chen, *et al*,. "Dark current characteristics of GaAs-based 2.6 μm InGaAs photodetectors on different types of InAlAs buffer layers", *Journal of Physics D: Applied Physics*, vol. 47, no. 8, p. 085107, 2014.

[33] A. Joshi, D. Becker, "High-speed low-noise pin InGaAs photoreceiver at 2 μm wavelength," *Photonics Technology Letters IEEE*, vol.20, no.8, pp. 551-553, Apr. 2008.

[34] M. Reddy, J. Olesberg, C. Cao and J. Prineas "MBE-grown high-efficiency GaInAsSb mid-infrared detectors operating under back illumination," *Semiconductor science and technology*, vol.21, no.3, pp. 267, 2006.

[35] H. Shao, A. Torfi, W. Li, *et al.*, "High detectivity AlGaAsSb/InGaAsSb photodetectors grown by molecular beam epitaxy with cut-off wavelength up to 2.6 μm," *Journal of Crystal Growth*, vol.311, no.7, pp.1893-1896, 2009.

[36] B. Liang, D. Chen, B. Wang, *et al.*, "Analysis, Optimization, and Design of 2-2.8 μm stacked multiple-juction PIN GaInAsSb/GaSb photodetectors for future O/E Interconnections," *Transactions on Electron Devices IEEE*, vol.57, no.2, pp.361-367, 2010.

[37] R. Sidhu. "Indium phosphide based photodiodes for mid-wave infrared detection" PhD dissertation, The University of Texas at Austin, Austin, Texas,.USA, 2005.

[38] H. Inada, K. Miura, Y. Nagai, *et al*., "Low dark current SWIR photodiode with InGaAs/GaAsSb type II quantum wells grown on InP substrate," in *Indium Phosphide & Related Materials (IPRM) IEEE*., 2009.

[39] B. Chen, W. Jiang, J. Yuan, *et al*., "SWIR/MWIR InP-bas ed PIN photodiodes with InGaAs/GaAsSb type-II quantum wells," *Journal of Quantum Electronics IEEE*, vol.47, no.9, pp.1244-1250, 2011.

[40] B. Chen, A.L. Holmes, "InP-based short-wave infrared and midwave infrared photodiodes using a novel type-II strain-compensated quantum well absorption region." *Optics Letters*,vol.38, no.15, pp. 2750-2753, 2013.

[41] K. Fujii, T. Ishizuka, Y. Nagai, *et al*., "MOVPE growth for photodiodes in 2.5 μm region with InGaAs/GaAsSb type-II quantum wells," *Physica Status Solidi (c)*, vol.10, no.5 pp.732-735, 2013.

[42] N Hattasan, A. Gassenq, L. Cerutti, *et al*. "Heterogeneous integration of GaInAsSb pin photodiodes on a silicon-on-insulator waveguide circuit," *Photonics Technology Letters IEEE*, vol.23.no.23 pp.1760-1762, 2011.

[43] R. Wang, S. Sprengel, M. Muneeb,, *et al*., "2 μm wavelength range InP-based type-II quantum well photodiodes heterogeneously integrated on silicon photonic integrated circuits," *Optics Express*, vol.23, no.20, pp.26834-26841, 2015.

[44] E. C. M. Pennings, R. J. Deri, R. Bhat, *et al.*,"Ultracompact, All-Passive Optical 90°-Hybrid on InP Using Self-Imaging" *Photonics Technology Letters IEEE*, vol 5, no.6 pp:701-703, 1993.

[45] J. Seok-Hwan, and K. Morito,. "Novel Optical 90 Hybrid Consisting of a Paired Interference Based 2×4 MMI Coupler, a Phase Shifter and a 2×2 MMI Coupler," *Journal of Lightwave Technology*, vol.28, no.9, pp.1323-1331, 2010.

[46] J. Seok-Hwan, and K. Morito, "Optical 90 hybrid with broad operating bandwidth of 94 nm," *Optics Letters*, vol.34, no.22, pp.3505-3507, 2009.

[47] J. Seok-Hwan, and K. Morito, "Compact InP-based 90° hybrid using a tapered 2×4 MMI and a 2×2 MMI coupler," in *Indium Phosphide & Related Materials (IPRM) IEEE*, 2010.

[48]. K. Voigt, L. Zimmermann, G. Winzer, *et al.*, "Silicon-on-insulator 90° optical hybrid using 4 × 4 waveguide couplers with C-band operation," in *European Conference on Optical Communication*, 2008.

[49] K. Voigt, L. Zimmermann, G. Winzer, *et al,*. "Fully passive Si-photonic 90° hybrid for coherent receiver applications," in *European Conference and Exposition on Optical Communications*, Geneva, Switzerland, Sep. 2011, pp. Tu-3.

Chapter 2 Overview of technical theories

In this chapter, we introduce the basic theories regarding the design and evalution method for the materials at 2 micron wavelengths. Experience formulas to estimate the bandgap of ternary InGaAs and quaternary AlInGaAs compound would be introduced with the corresponding characterization system through the visulazation of laser-excited photoluminece spectrum.

Explanations about the fabrication and characterizaition for optical-electronic devices will also be demonstrated here involving general process steps, I-V, C-V measurement, high-speed characterization and transmission spectrum characterization.

2.1 Material design and characterization

The material system of InGaAs can be used to build the active region of 2-µm wavelength photodiodes on InP substrate benefiting from the absorption spectrum envolving this wavelength range as well as the large carrier mobility for high speed application. By introducing a small portion of Al, the bandgap (AlInGaAs) could be relatively enlarged which is suitable to achieve the cladding layer acting as a window to let the light in shorter wavelengh (compare to the absorption wavelength edge of the intrinsic layer) pass through. Here, estimation of the bandgap for the material system used in this thesis will be presented in the following sections.

2.1.1 Bandgap of ternary InGaAs and quaternary AlInGaAs compound

By increasing the indium content of the ternary InGaAs alloy, the edge of the absorption spectrum can be extended to 3.4 µm at room temperature [1]. The direct-gap character can be maintained over the entire composition range.Using this material as the aborption layer, photodiodes can achieve high photoresponsivity covering the wavelengths around 2 microns which is matched with the low-loss window of the HCPBG fibre.

For the InGaAs ternary alloys establishing the absorption layer, the energy gap of E_g can be estimated as a quadratic function as Eq. 2.1.1,

$$E_g(In_xGa_{1-x}As) = xE_g(InAs)+(1-x)E_g(GaAs) - x(1-x)C$$

(2.1.1)

Where, x represents the alloy composition of InAs in the compound which could be considered as the combination of two binaries of InAs and GaAs, C is the bowing parameter which is positive and assumed to be temperature-independent for the InGaAs material. The bandgap of each binary component can be fitted in the empirical Varshini form considering the temperature-dependent character of bulk semiconductors [2].

Ascribed to the high light absorption efficiency benefiting from the wide-bandgap cap which acts to be a transparent window for the wavelengths between the cut-off peaks of absorber and cap, heterogeneous structure is utilized to create the junction area of the 2 micron photodiode. Here, a small composition of aluminum (Al) is introduced into the above-mentioned InGaAs alloy of the absorber so that a larger energy gap is created indicating a peak blue-shifting in the photoluminescence (PL) spectrum [3]. Considerring the lattice-mismatching potentials of the new alloys, an empirical formula in molar fraction expression would like to be used for estimating the AlInGaAs bandgap involving the sum of the weighted terms based on the bandgap energy of corresponding binary compounds and the bowing parameters of ternary alloys, in addition with a surface bowing estimation for the error correction [4]. It could be more generally used comparing to the lattice-matching limitation case in Ref. 2 explained by the linear interpolation between the bandgap energy of the two ternaries lattice-matched to InP substrate ($Al_{0.48}In_{0.52}As$ and $In_{0.53}Ga_{0.47}As$) with a direct-gap bowing term.

The above-mentioned function could be constructed based on the main term of E_{g0} (fundamental estimation of the bandgap energy for the compound) in addition with a deviation of ΔE_g as Eq. 2.1.2,

$$E_g(Al_xIn_yGa_zAs) = E_{g0}(Al_xIn_yGa_zAs) + \Delta E_g \qquad (2.1.2)$$

$E_{g0}(Al_xIn_yGa_zAs)$ can be expressed as Eq. 2.1.3,

$$E_{g0}(Al_xIn_yGa_zAs) = xE_g(AlAs) + yE_g(InAs) + zE_g(GaAs)$$
$$-xyC(AlInAs) - yzC(InGaAs) - xzC(AlGaAs)$$

(2.1.3)

Where, $E_g(AlAs, InAs, GaAs)$ is the band gap energy of the binary compound with the value of 3.0067 eV for AlAs, 0.3556 eV for InAs and 1.4256 eV for GaAs at the temperature of 20 °C; $C(AlInAs, InGaAs, AlGaAs)$ is the bowing parameter of the corresponding ternary alloy with the value of 0.70 for AlInAs, 0.477 for InGaAs, and 0.5018 for AlGaAs; x, y and z represent the fractions of AlAs, InAs and GaAs in the alloy satisfying the condition of $x + y + z = 1$.

The correction expression of ΔE_g is as follows,

$$\Delta E_g = -0.9272xyz$$

(2.1.4).

The final expression at the room temperature (20 °C) can be expressed as follows,

$$E_g(Al_xIn_yGa_zAs) = 3.0067x + 0.3556y + 1.4256z - 0.7xy -$$
$$0.477yz - 0.5018xz - 0.9272xyz$$

(2.1.5),

Correction terms with more accuracy could also be applied by fitting with the results of the pre-designed material [4].

The lattice misfit between the high-indium content layer and the InP substrate (5.87 Å) would like to be enhanced due to that the lattice constant of the InGaAs is increased linearly with the increasing composition of InAs (6.06 Å) [5]. Threading dislocations would be induced during the material growth and disperse into the intrinsic layer. Those defects would degrade the photodiode performance by introducing generation-recombination centers for leakage generation as well as interstitial sites resulting in larger reverse voltage for fully depleting the intrinsic layer [6]. To overcome this, a

metamorphic buffer layer was introduced in between the junction layers and the InP substrate to release the lattice mismatching and suppress the defect diffusion. Considering the large thickness of linearly-graded InGaAs buffer as well as the growth control complexity of InAsP epitaxy, we used an InGaAs parabolic grading layer to let the defect mainly disperse in the transverse plane vertical to the layer growth direction rather than into the intrinsic layer. Thus, a thin buffer layer could be achieved for saving the total growth time as well as maintaining element source type to be the same [7, 8].

Most of the 2 micron epitaxial structures mentioned in this thesis were grown in use of the MOCVD method by the Epitaxy and Physics of Nanostructures Group at Tyndall. This permits digitally controls on the composition of each element of the alloy as well as fast growth rate satisfying the efficiency requirement of the industrial production.

2.1.2 Characterize the material bandgap property

It is important to identify the energy band gap for the grown wafers in quantum wells or bulk material especially for those working at 2 µm wavelength band. To achieve a clear view on the energy bandgap of the grown 2 µm material, optical characterization tests regarding PL spectrum and light absorption spectrum need to be done.

Photoluminescence spectrum measurement system plays the key role to clarify the band structure by analysing the spontaneous emitting output generated from the recombination of electron-hole pairs with corresponding carriers distributed in different energy band. As it is shown in Fig. 2.1, a laser is used to pump the material for activating electrons and holes, and then the broad band self-emitted light due to the carrier pair recombination is coupled into the monochromator by the focus lens so that it could be analysed by the scanning step of several nanometres. In order to amplify the small signal while supressing the noise, a lock-in amplifier is used together with the photodiode to convert the weak projected light into electrical signal. The whole setup was controlled by the computer with LabVIEW programs.
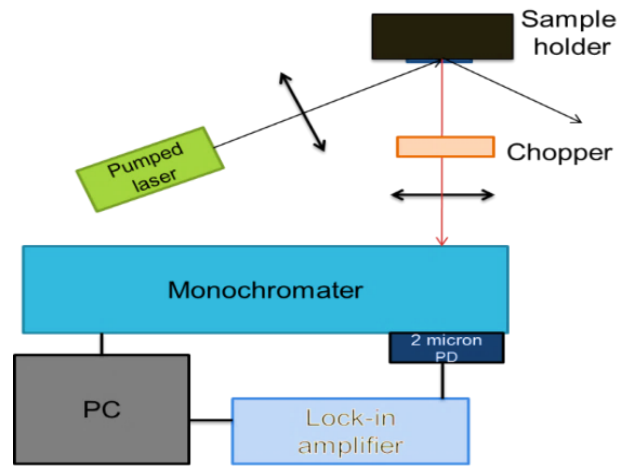
Figure 2.1: *2 micron wavelength PL spectrum characterization system*

As the main component of this system, the photodetector should have a working wavelength range covering the 2 micron wavelength region. Fig. 2.2 shows the photoresponsivity of the 2 micron commercial PD from Thorlabs company working in the PL characterization setup. Its responsivity ranges from 1.2 microns to 2.5 microns which provides spectrum detection across the band edge of all the 2 microns materials grown in Tyndall.
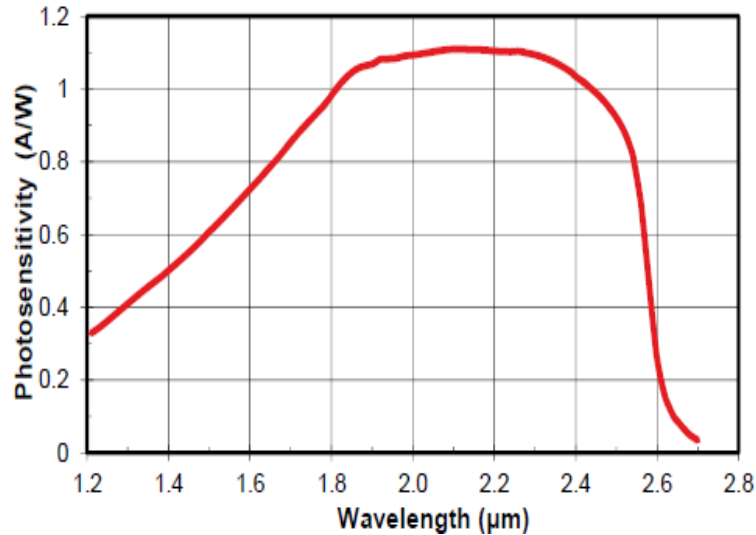
Figure 2.2: *Photoresponsivity for the commercial 2 micron photodetector from Thorlabs Company.*

By use of this system, we could get the PL spectrum of the 2 micron materials on both quantum well as well as bulk structure shown in Fig 2.3. For quantum well

materials, the band edge wavelength of the barrier layer would also be estimated from the scanning results. Though affected by the falling of the PD photoresponse at long wavelengths > 2.3 µm, the system is still able to provide PL peak detection longer than 2.1 µm proved by the different cut-off wavelength position exhibited in Fig. 2.3.
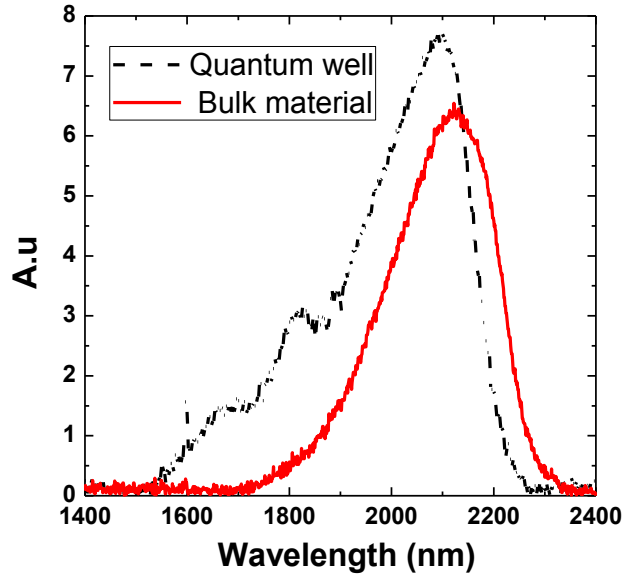
Figure 2.3: *PL spectra of different materials for 2 micron applications*

The band gap enlarging of the original quantum well structure due to the quantum well intermixing (QWI) process (change the bandedge by intermxing the wells and barriers) can be characterized by observing the blue-shifting of the PL spectrum peak by this setup. With the broad working band of the monochromater and photodiodes, we were able to observe the shift of hundreds nm for the 2 micron quantum well structures which are shown in Fig. 2.4. It could be seen that fluctuations appear on some curves indicating the low signal to noise ratio (SNR). This is due to the low emission efficiency resulting from the defects within the epitaxial layer. To obtain more accurate results, a high-power injection laser is required to provide sufficient pumping level.
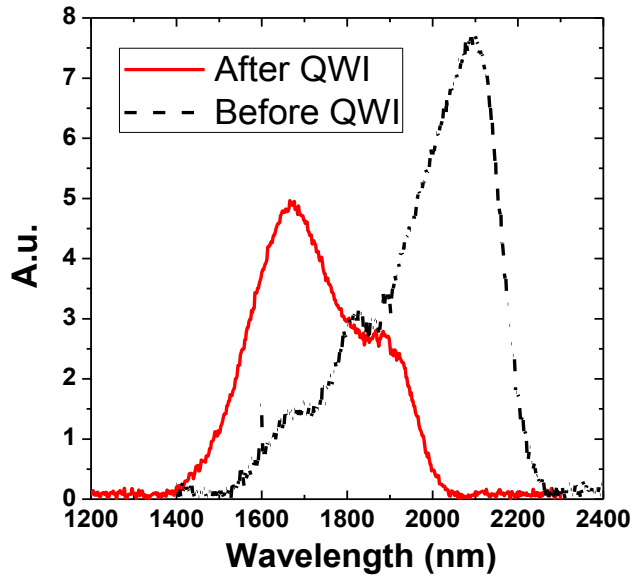
Figure 2.4: *PL spectrum for2 micron quantum well material after quantum well intermixing.*

In addition, the band gap of the material is also available to be extracted from the sharp dropping edge of the optical absorption spectrum. Using a white light source, the final results could be deduced after excluding the part coming from reflection and transmission in the absorption spectrum test system.

2.2 Device fabrication and characterization

2.2.1 Main steps for device fabrication

Standard III-V component fabrication processes have been applied on all 2 µm photodiodes and 90° optical hybrids. Patterns were defined via Ultra-violet (UV) lithography after the photoresist was spun on the wafer surface. Then dry etching is applied in order to create three-dimensional (3D) structure for the device. After that, passivation on the device surface and its side wall could be realized through Plasma-Enhanced Chemical Vapour Deposition (PECVD) with silicon oxide or silicon nitride deposition. Then, window opening is achieved by use of the plasma asher after patterning the intentionally-exposed area by UV lithography. For the photodiode, the lift-off process after the metal evaporation was operated to create contact pad. Finally,

devices in bar or single device were cleaved from the wafer after thinning the substrate for electrical and optical test or packaging in a module.

During the fabrication of the photodiode, p metal deposition followed by the thermal annealing could be the first step due to that it acted as a protective layer preventing contact surface from the plasma damage during the dry etching in the mesa formation and window opening. In addition, wet etching will be utilized to polish the side wall after the dry etching to preclude the leakage generation associated with the surface roughness. Temperature control during the PECVD passivation was also considered to minimize the dark current generation from the side wall. More techincal details regrading the fabrication processes can be found in the Appendix 1 and 2. And, innovation points will be described in the latter chapter (Chapter 3).

2.2.2 General I-V and C-V characterization

For electrical characterization, current-voltage (IV) test is applied to evaluate the quality of the p-n junction as well as the leakage of the device while capacitance-voltage (CV) test indicates the radio frequency (RF) bandwidth of the photodiode limited by the resistance-capacitance (RC) constant.

After finishing the fabrication processes, basic IV test was applied as the first step test to check the forward current plot in log form in a range from 10^{-8} to 10^{-3} A as a function of linearly-increased bias voltage, so that the ideality factor of the diode could be obtained. Typically this factor is smaller than 2. When it is coming close to 1, it means diffusion current is the dominant current source. When it is coming close to 2, the generation-recombination current will be a key factor which we try as best as possible to supress.

Additional capacitance of the device are either generated from the pn junction or the interval between the top bonding pad and the conductive substrate such as n-doped InP substrate. Those capacitances suppress the effective range of the device's electrical response which is setting an extra limitation on working bandwidth of the photodiode in cooperating with the load and serial resistance. Therefore, the -3dB cut-off frequency confined by RC constant could be derived from the Eq. 2.2.1,

$$f_{-3dB} = \frac{1}{2\pi RC}$$ (2.2.1)

R is the total resistance involving both 50 Ω load resistor and serial resistance of the PD, C is the total capacitance containing the natural junction capacitance and parasitic capacitance of the pad. The serial resistance is able to be deduced from the linear region of the forward IV test result. And, the total capacitance at different direct-current (DC) bias voltage could be abstracted by detecting the image part of current under small alternative-current (AC) voltage modulation by use of the Agilent semiconductor analyser (CV Enabled B1500 (1)).

2.2.3 High speed characterization

A photodiode plays a key role to convert the optical signal into electrical signal for further processing. In order to evaluate its performance in the real optical communication system, high speed characterization tests with respect to S_{21} parameter and eye pattern were performed in cooperation with the illumination of the modulated light.

For demodulating the high speed light signal, the photodiode should have a RF response more than or at least equal to the signal modulated frequency. Not only the capacitance but also the carrier traverse time across the junction affects the frequency of the photodiode. Therefore, small signal dynamic measurements should be performed on the photodiode in order to get the -3 dB roll-off bandwidth via extracted S_{21} parameter as a standard to analyse its high frequency response.

To further analyse the opto-electric signal transferring of the photodiode, eye pattern test system has to be built at a specific bit rate. Regarding the eye diagram results, the eye amplitude reflects the electrical signal amplitude while eye opening clearance shows the SNR. Most importantly, the slope of the rising edge shows how the high frequency components of the signal transferring through the device.

2.2.4 Transmission spectrum characterization

By using a lens-ended single mode fibre (SMF) specially designed for the application around 2 µm wavelengths, the broad-band light from the Amplified Spontaneous Emission (ASE) of the Thulium Doped Fibre Amplifier (TDFA) was optimally coupled into the test devices. At each of the output ports, the transmitted light was then collected again by the lens-ended SMF fiber and delivered to an Optical Spectrum Analyser (OSA) to evaluate the resulting spectrum.

2.3 Summary

Here, basic theories used to design and evalute the bulk and quntum well materials at 2 micron wavelengths have been explained. Main steps of fabrication and measurement are also introduced to obtain the I-V, C-V, bandwidth and transmission spectrum characterizations for the optoelectronic devices displayed in this thesis.

2.4 References

[1] A. Krier, and Y. Mao. "High performance uncooled InAsSbP/InGaAs photodiodes for the 1.8–3.4 μm wavelength range," *Infrared physics & technology*, vol.38, no.7, pp.397-403, 1997.

[2] I. Vurgaftman, J. R. Meyer, L. R. Ram-Mohan, "Band parameters for III–V compound semiconductors and their alloys," *Journal of applied physics*, vol.89, no.11, pp.5815-5875. 2001.

[3] M. Jain, "An investigation of broad gain spectrum InGaAs/InAlGaAs quantum well lasers latticed matched to InP", PhD dissertation, Department of Electronics and Electrical Engineering, The University of Glasgow, Glasgow,.UK, 2002.

[4] T. Mei, "Interpolation of quaternary III-V alloy parameters with surface bowing estimations," *Journal of applied physics*, vol.101, no.1, pp.013520-013520. 2007.

[5] S. Adachi, "Structual properties", *Physical properties of III-V semiconductor compounds*. Jon Wiley&Son, New York, USA,1992.

[6] A. Joshi, S. Datta, "High-speed, large-area, p-i-n InGaAs photodiode linear array at 2-μm wavelength," in *Defense, Security, and Sensing*, the international society for optics and photonics (SPIE), Maryland, USA, pp.83533D, 2012

[7] BH Müller, R Lantier, L Sorba, *et al*."$Zn_{0.85}Cd_{0.15}Se$ active layers on graded-composition $In_xGa_{1-x}As$ buffer layers," *Journal of applied physics*, vol.85, no.12, pp.8160-8169,1999.

[8] A Gocalinska., M. Manganaro, E. Pelucchi, "Suppression of threading defects formation during Sb-assisted metamorphic buffer growth in InAs/InGaAs/InP structure," *Applied Physics Letters*, vol.100, no.15, pp.152112, 2007.

Chapter 3 2 µm wavelength high speed photodiodes

3.1 Introduction

The desirable properties of photodiodes (PD) for communications include high speed, high responsivity at particular wavelength as well as low dark current. These properties are significantly dependent on the design of the material, device structure and the fabrication process. $In_xGa_{1-x}As$ is a suitable material with the feasibility to obtain a bandgap of 2000 nm by increasing the Indium composition in the compound from x=0.53 which is lattice-matched to InP to x=0.74. However, this introduces strain (~1.5 %) because of the lattice mismatch with the InP substrate, making it be challenged to obtain a high quality epitaxial crystal and potentially resulting in a high dark current. This can be accommodated by using strained quantum wells structure or by using buffer layers to release the strain due to the lattice mismatching. By using the compressively strained multiple $In_{0.74}Ga_{0.26}As/In_{0.53}Ga_{0.47}As$ quantum well (MQW) structure (low number of quantum well layers, not strain-relaxed), a ridge waveguide type photodiode demonstrating a photoresponse at 2 µm wavelength as well as a low leakage current. The thin intrinsic layer will take less time for the carrier to transverse so that higher working bandwidth can be expected. While, subjected to the small acceptance aperture of the waveguide geometry and tens of nm thick active layer stacks, the coupling efficiency is low (external quantum efficiency is only 23.46 % involving the coupling loss) which results to the limited tolerance of fibre alignment during the test and package assembling. To improve the photoresponse of the detector for larger optical SNR as well as better optical alignment tolerance, a 2 µm surface normal type PD based on the strain-relaxed InGaAs absorber with AlInGaAs claddings is realized benefitting from the strain accommodation from a parabolic graded buffer. By optimizing the layer stack structure, a 3-dB bandwidth of ~10 GHz is achieved while maintaining a polarization-insensitive photoresponsivity up to 0.93 A/W taking the advantage of the round mesa geometry and thick absorption layer.

An eye pattern of 15.6 Gbit/s has been obtained with the sample attached on the test submount to prove the ability to work at the 2 micron optical communication system. Finally, balanced photodetector was realized based on the top-illuminated type high speed photodiode on the semi-insulating substrate.

3.2 Ridge waveguide structure in compressively strained quantum wells

3.2.1 Epitaxial layers design

Due to the large crystal mismatch between the active layer and the substrate, InGaAs material with absorption band around 2 µm wavelengths is strongly strained when it is grown on InP substrate. If this is not accommodated properly, dark current generated from defects would like to be highly increased for the photodiode fabricated on the same material. Therefore, the SNR of the device working in optical communication system would be further degraded. A quantum well structure is able to keep such strain effect within an acceptable layer thickness though more technical control is required for the epitaxy growth. Meanwhile, due to the short optical transmission path along the layer growth direction, the absorption rate is low with most of the light energy transmitted when it is vertically projected on to the material stacks. The ridge waveguide geometry structure in which the light can be illuminated at the device facet is proposed to improve the absorption efficiency with light horizontally propagating within the quantum well absorption region. In addition, higher working speed can be expected due to the carrier transportation path being perpendicular to the light transportation direction is very short probably proportion to the total thickness of quantum wells in such structure.

Here, two kinds of strained quantum well material were selected and grown by Metal Organic Chemical Vapour Deposition (MOCVD) to develop the 2 micron absorption region on InP substrate. QW_1 is similar to the epitaxy layer structure of the laser in Reference No.1 from Eblana Company. The MQW structure consisted of three compressively-strained $In_{0.74}Ga_{0.26}As$ quantum wells and four lattice-matched $In_{0.53}Ga_{0.47}As$ barriers. Material QW_2 were designed and fabricated in Tyndall on

semi-insulating substrates with two 9-nm-thick $In_{0.82}Ga_{0.18}As$ quantum wells separated by a 10-nm-thick AlInGaAs (PL=1240 nm) barrier layers sandwiched by 80 nm and 110 nm thick un-doped lattice-matched AlInGaAs layers on the top and bottom respectively. Then, a InGaAsP layer was also grown as an etch stop selectively from InP followed by a 1.7 µm thick highly p-doped ($Zn\sim1\times10^{18}$) InP layer to reduce the loss from mode leakage into the top contact layer. Finally, the highly Zn-doped InGaAs (100 nm) is formed as the contact layer [2]. The whole designed epitaxial material structure is shown in Fig. 3.1.
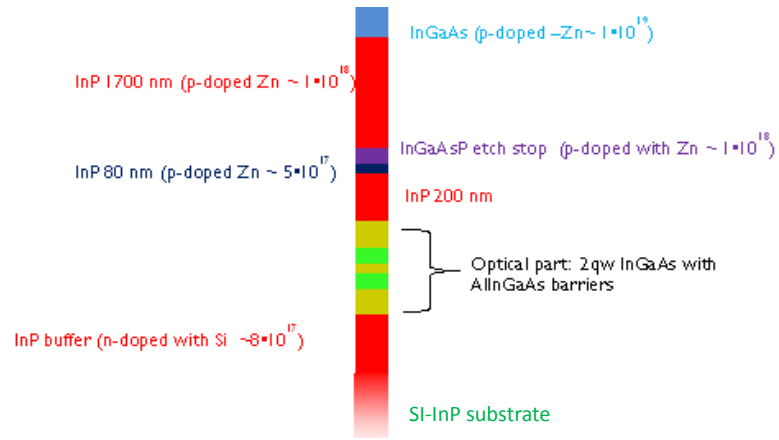
Figure 3.1: *The epitaxial layer structure for QW₂ material*

3.2.2 Device structure and fabrication

As shown in Fig. 3.2, coplanar electrodes with Ground-Signal (GS) structure have been used to improve the high frequency property of our photodiodes. BCB material was applied under the electrode pads for both types of quantum well material which achieved the planarization for the electrical contact in the same plane and minimizes the parasitic capacitance coming from the p-contact metal pad relative to the n-doped InP substrate for QW_1 material. The ridge waveguide geometry was obtained through dry etching with $Cl_2/CH_4/H_2$ in an Oxford 100 ICP system where a 500 nm thick SiO_2 layer was used as the etching mask[3]. Following the deposition of a 150 nm thick SiN_x passivation layer, BCB 4024-35 was spin-coated and cured at 250 ºC for one hour, followed with etching back of the BCB in a SF_6/O_2 Inductively Coupled Plasma (ICP) process until a planarized ridge is obtained. Then, a layer of 150 nm thick SiN_x

was deposited on top of the BCB to improve the adhesion with the metal electrodes. Windows for p and n-type ohmic contacts were opened by dry etching with the gas of etching back through the SiN$_x$ and BCB. Finally, a 300 nm thick Ti-Au layer was evaporated for both p and n contact pads using electron beam evaporation.
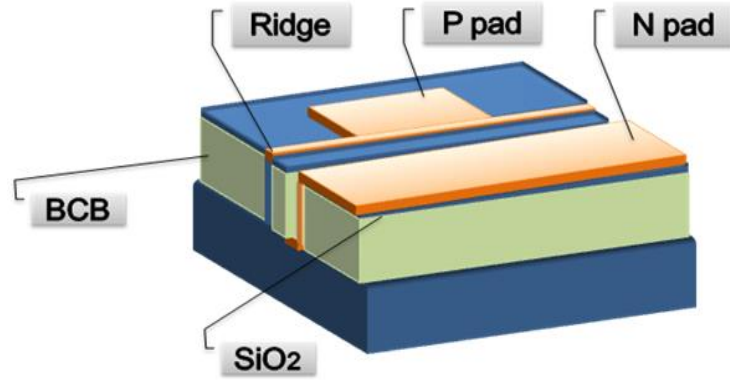
Figure 3.2: *Device scheme for the ridge type photodiode in QW$_1$ and QW$_2$ materials*

The overview of the processed samples can be seen from Fig. 3.3 (a). In addition, to form the facets of the device, accurate cleaving along the indicated red line shown in Fig. 3.3 (b) has been realized .
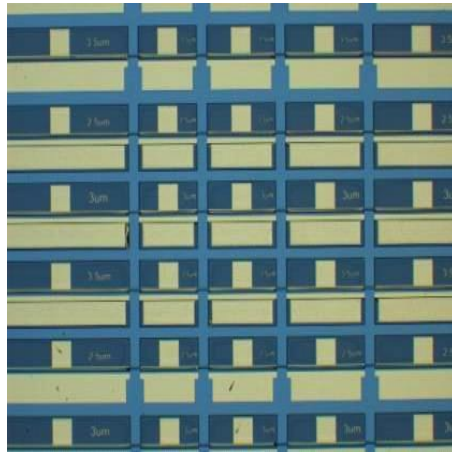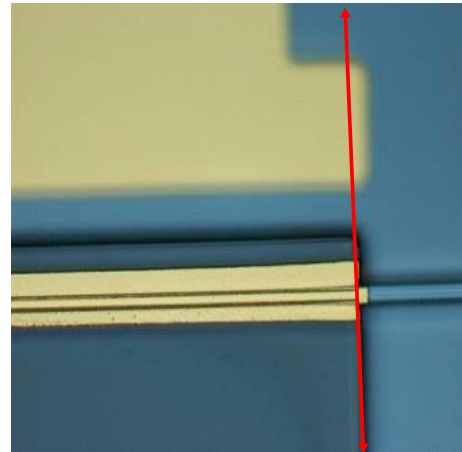
(a)   (b)

Figure 3.3: *Top view of the ridge photodiodes (a) overview of all the fabricated samples, (b) cleaving location on one single device.*

3.2.3 I-V C-V and photoresponse characterizations

Limiting the Signal To Noise Ratio (SNR), the device dark current as a noise source and photoresponsivity defining the recovered signal magnitude should be characterized.
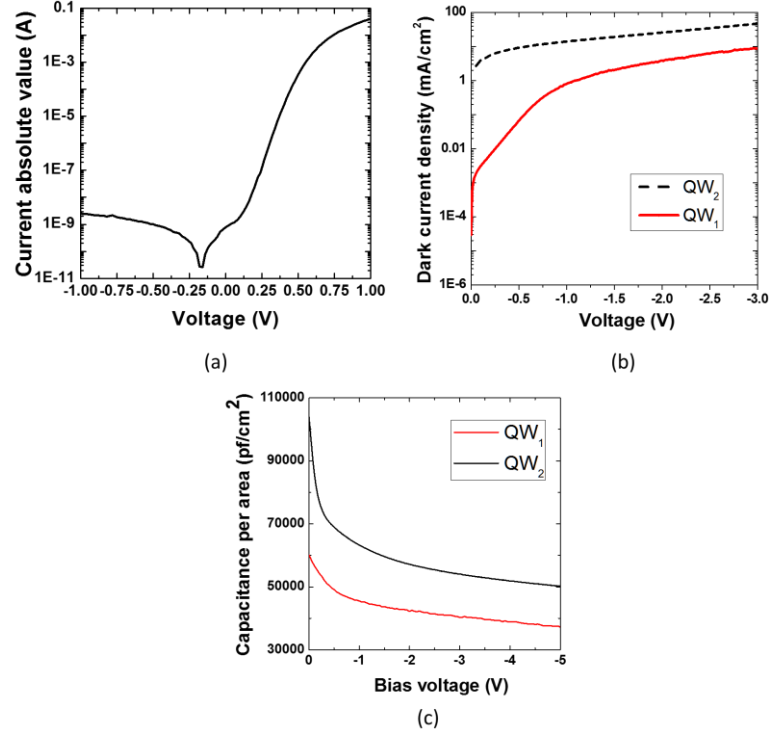
Figure 3.4: *I-V property of ridge waveguide PD in QW1 material (ridge width: 3 μm, device length: 440 μm) (a), Leakage density characters with biased voltage for different quantum well materials (b).Captacitance per area for the ridge waveguide photodetectors made in QW1 and QW2 material.*

As it is shown in Fig. 3.4 (a), the leakage of the ridge waveguide photodiode in material QW_1 is approaching to 2.55 nA at -1 V bias proving that the lattice-mismatch has been suppressed by using the strained quantum well structures. While, at the same reverse bias, the photodiode in QW_2 material on the semi-insulating substrate demonstrates a dark current density (46.94 mA/cm^2) nearly 5 times higher than the QW_1 material on n-doped substrate (8.97 mA/cm^2) (Fig. 3.4 (b)). This results from the higher indium content of material QW_2 with larger lattice constant difference relative

to the substrate which may generate more lattice-mismatch defects during the epitaxy growth.

To figure out the Resistance-Capacitance (RC) factor which confines the work speed of the detector, the CV measurement is appled on the cleaved devices to extract the capacitance vaule under different reverse biases. Due to the ultilization of BCB taking the merit of low dielectric constant, the parasitic capacitance (between the metal pad and conductive substrate) is fully suppressed and the main source of the device capacitance per area can be estimated mainly from the pn junction of the material.To accurately demonstrate the natural capacitance property away from the limitation of the ridge dimension, the capacitance per area under different bias voltages is ploted in Fig.3.4 (c). Obviously, we can see that the device in use of QW_1 layer stacks exhits a number of 37237 pf/cm^2 in -5 V which is much lower than the one using QW_2 material (50130 pf/cm^2) under the same bias. Therefore, the detectors made in the junction of QW_1 material can demonstrate smaller capacitance comparing to those in QW_2 juction patterned in the same ridge dimension.
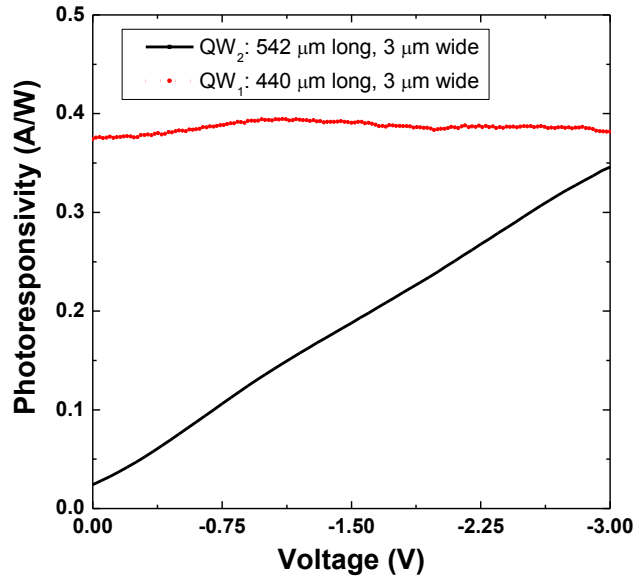
Figure 3.5: *Photoresponsivity for the ridge type photodiodes in different quantum well materials, red for the QW1 material with the length of 440 μm, width of 3 μm, black for the QW2 material with the length of 542 μm, width of 3 μm.*

With a lensed-ended single-mode fibre and a 2-μm wavelength single mode laser, the photoresponse of the fabricated ridge type detector has been characterized with the

results shown in Fig. 3.5. From the red line of Fig. 3.5, we can see that the photoresponsivity of the 400 µm long photodetector in QW_1 material can be up to 0.38 A/W (-3 V) excluding the fibre loss and non-sensitive to the reverse bias. In contrast, the device made in QW_2 material is very sensitive to the bias voltage probably due to the valence band offset between the non-doped InP layer and the deep-valence-band AlInGaAs barrier (of the QW), which acts as a barrier to block the hole carrier movement to the anode electrode. This can be indicated by the band structure shematics of this layer stack which is visilized by using the software of SimWindows (Fig. 3.6). Correspondingly, the holes accumulation close to the barrier would establish an electric field partially shielding the reverse bias field. In addition, less quantum well pairs could decrease the coupling efficiency with smaller acceptance aperture which further degrades the external quantum efficiency referring to the photoresponsivity of the QW_2 detectors (Fig. 3.5, black line). The responsivity can be potentially improved by use of the AR coating on the input waveguide facet or further by the integration of the spot size converter to match the fibre mode. Moreover, the polarization state of the input light should be optimized (may bend the fibre or use a fibre polarization mentaner) due to the polarization-sensitive propety of the strained quantum wells.
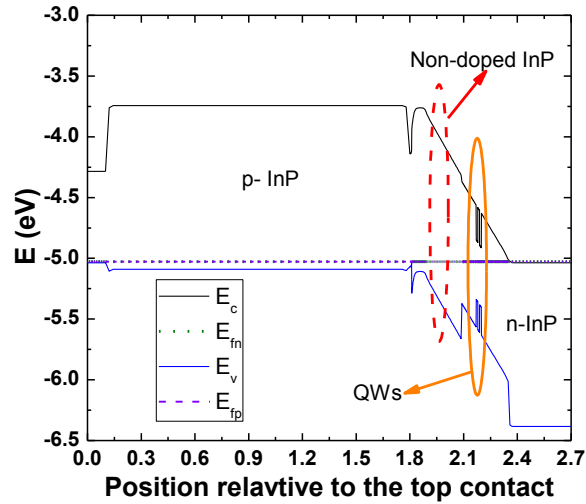
Figure 3.6: *Band structure for QW₂ material on the semi-insulating substrate*

63

3.2.4 High speed characterizations

Another important property for the photodiode is the small signal bandwidth determining how much capacity it could provide in real optical communication system. A high frequency test system as Fig. 3.7 was built to test the chips on the bar cleaved from the wafer by use of GS probe to collect the electrical signal and lensed fibre for light coupling. Meanwhile, a network analyser was applied to load the modulated broad band signal on to the opitcal modulator converting the electrical signal to optical domain. Then, the S_{21} parameter of each frequency was extracted after signal recovering back to the electrical domain by the photodiode and plotted. The frequency corresponding to the -3 dB cut-off point in the S_{21} curve indicates the small signal working bandwidth of the photodetector.
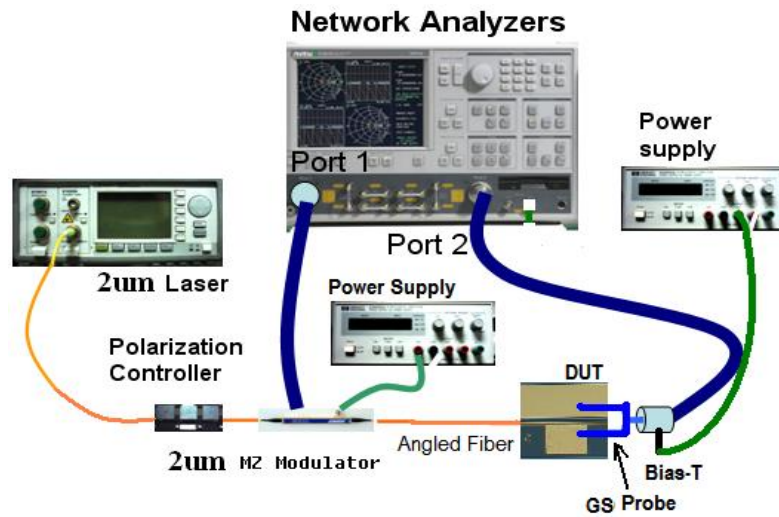
Figure 3.7: *High frequency test setup for the evaluation of photodetector chips on the bar.*

As it shown in Fig. 3.8, the bandwidth of the 300 µm long ridge type photodiode in QW_1 material on n-doped substrate with BCB could reach as high as 7 GHz at -7V which was limited by the ~6 GHz GS probe.
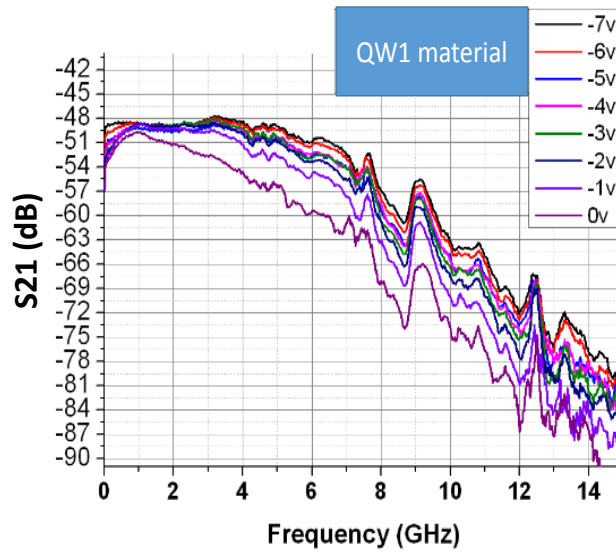
Figure 3.8: *S₂₁ of the ridge waveguide photodetector fabricated in QW₁ materials with BCB on n-doped substrate at 2 micron wavelengths.*

The photodiode fabricated in QW$_2$ material with BCB on semi-insulated InP substrate just reach up to 5 GHz under -12 V bias which is also sensitive to the amplitute of the reverse bias (Fig. 3.9). This may be due to the same reason demonstrated in Fig. 3.5 that the valance band offset between InP and AlInGaAs barrier layer leads to holes accumulating which partially neutralize the electrical field driving the hole carriers to transport over the intrinsic region.
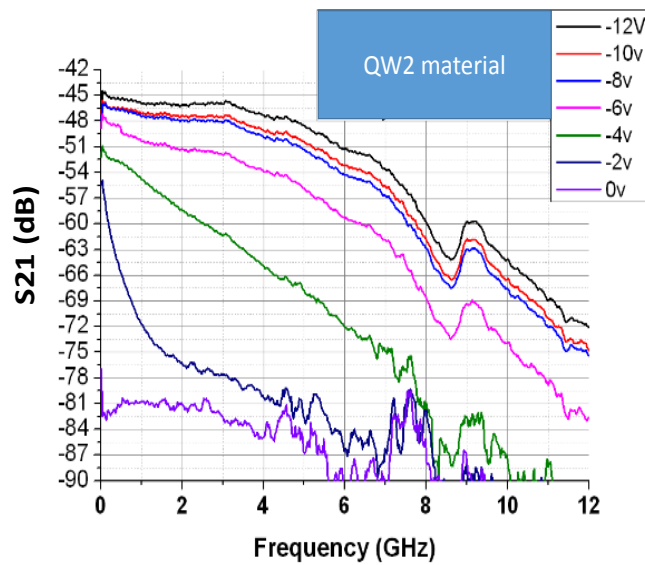
Figure 3.9: *S₂₁ of the ridge waveguide photodetector fabricated in QW₂ materials with BCB on semi-insulated substrate at 2 micron wavelengths.*

Due to the bandwidth limit of the GS probe, photodiode chips on a bar could not be characterized at more than 7 GHz. However, packaging would help the device to be tested at much higher frequency over such limitation due to the probe. Similar to the setup in Fig. 3.7, high speed electrical signal was converted to the light singal by the application of an optical modulator and the network analyser was used to obtain the S_{21} parameter of the 2 micron packaged photodiode through the RF cable (Fig. 3.10). In addition, the ridge waveguide and strained quantum well structure make the photodiode sensitive to the polarization of the input light. But this could be compensated by bending the input fibre in front of the packaged photodiode to let it maintain the best polarization state.
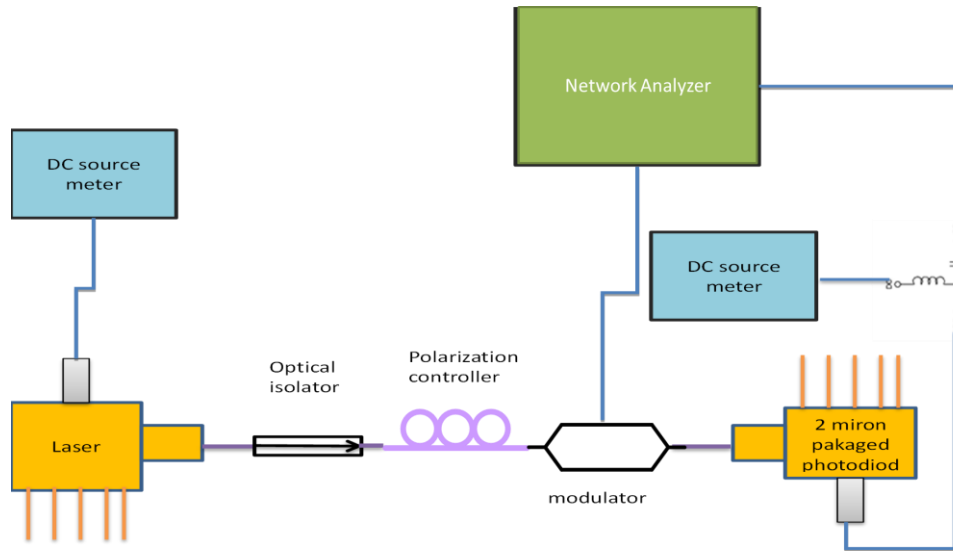
Figure 3.10: *High frequency test setup for the 2 µm packaged ridge photodiode*

High frequency test was first carried out at 1550 nm wavelength due to that the available 20 GHz 1550nm modulator could provide larger bandwidth to accurately characterize the photodiode. In addition, narrow band gap material is able to absorb the light shorter than the local band gap wavelength.

As it can be seen from Fig. 3.11, the packaged module containing the 2 µm photodector in QW_1 material planarized with BCB could provide the working bandwidth as high as 12.9 GHz under -5 V bias at 1550 nm wavelength.
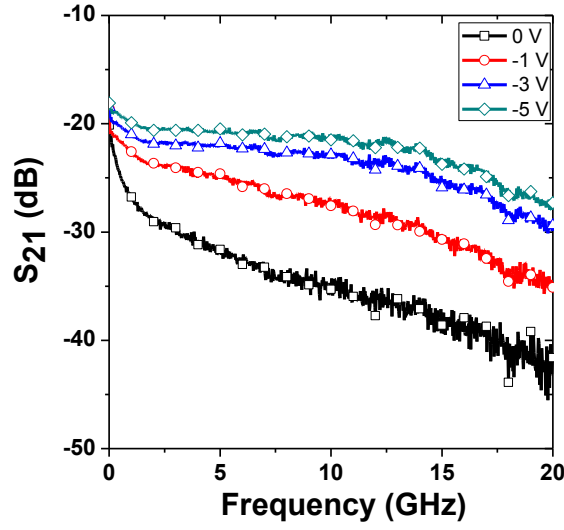
Figure 3.11: *S_{21} parameter at 1550 nm for packaged ridge photodiode in QW_1 material with BCB on n-doped substrate.*

Meanwhile, a degradation of the photoresponse during the light coupling process was observed due to the low tolerance of fibre alignment subjected to the small spot size of the ridge waveguide geometry and the thin absorption layer of the quantum well structure. Finally, the photoresponsivity of the packaged device dropped from 0.3 A/W to the 0.14 A/W at 0 V bias due to the fiber coupling misalignment loss after the completion of the packaging process [4].

3.3 Surface-normal-illuminated photodiode in strain-relaxed bulk material

A surface-normal-illuminated configuration is preferred in the real applications not only due to the better light coupling efficiency and higher signal to noise ratio (SNR) but also due to better fiber alignment tolerance for packaging which takes the advantages of the circular geometry for mode matching with the input fiber. Here, to obtain a thick enough absorption layer along the light transporting path while maintaining the epitaxial material quality, a thin parabolic-graded buffer is proposed to release the heavy strain due to the large lattice mismatch between the 2 µm intrinsic layer and the InP substrate. Layer epitaxial structures and fabrication processes have been optimized to achieve high bandwidth, small leakage and large photoresponsivity

at 2 µm wavelengths. All the layer structures were grown using MOVPE by the Epitaxy and Physics of Nanostructures Group in Tyndall.

3.3.1 Material Design for the surface normal photodiodes at 2 µm wavelengths

The InGaAs material system is appropriate for long wavelength applications due to flexible growth by MOCVD and mature processing technologies for device fabrication. We use $In_{0.7}Ga_{0.3}As$ as the intrinsic absorbing layer material which has a band edge of around 2.2 µm (Fig. 3.12). A thin buffer layer (thickness of 500 nm) obtained by parabolic grading of the indium content from 0.53 to 0.8 is used to relax the lattice constant difference between the absorbing layer and the InP substrate [5]. By adding aluminum to the $In_{0.7}Ga_{0.3}As$, the bandgap is blue shifted to approximated 1.8 µm (Fig. 3.12, solid) and used as cladding layers.
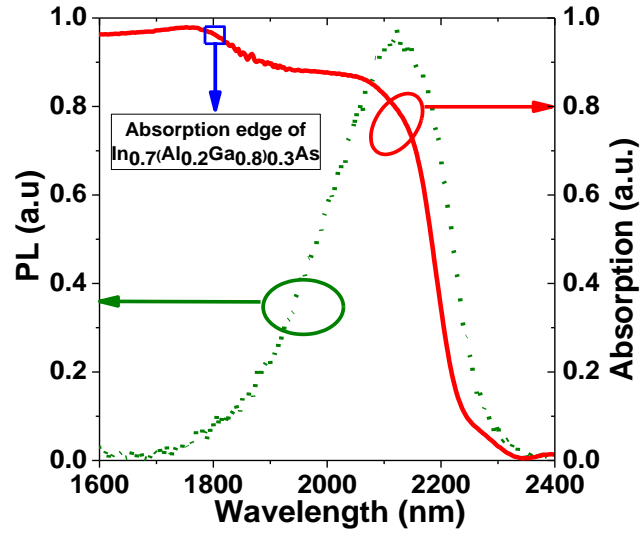
Figure 3.12: *Photoluminescence (dot) and absorption (solid) spectrum of Design-1 on n-doped substrate.*

The p-doping profile and layer thickness are optimized to achieve high speed operation. Two different designs for the 2 µm surface normal photodiode are investigated here. We compare active region thicknesses of 2500 nm and 2000 nm and in the second design we increase the p-doping level at the upper cladding and remove

the un-doped AlInGaAs layer in order to promote hole transport. The structural details of the two designs which were grown by MOCVD are presented in Table.3.1. SEM graph for viewing the layer stacks of the Design-2 material can be found in Fig.3.16.

Table 3.1: Epistaxial structures design for 2 µm surface normal photodiodes

Material	Dopant	Design-1		Design-2		Note
		Thick.	Level	Thick.	Level	
		(nm)	(cm^{-3})	(nm)	(cm^{-3})	
In$_{0.7}$Ga$_{0.3}$As	Zn/C	100	3×10^{19}	100	3×10^{19}	Contact
In$_{0.7}$(Al$_{0.2}$Ga$_{0.8}$)$_{0.3}$As	Zn	600	1×10^{18}	*500*	*2-3x10^{18}*	p-cladding
In$_{0.7}$(Al$_{0.2}$Ga$_{0.8}$)$_{0.3}$As		100		*0*		
In$_{0.7}$Ga$_{0.3}$As		2500		*2000*		absorption
In$_{0.7}$ (Al$_{0.2}$Ga$_{0.8}$)$_{0.3}$As	Si	700	1×10^{18}	1000	1×10^{18}	n-cladding
In$_x$Ga$_{1-x}$As(x=0.53→0.8)		500		500		parabolic grade
In$_{0.53}$Ga$_{0.47}$As		50		50		
InP substrate						n-doped

3.3.2 Device fabrication

Isolated mesa photodiodes in different diameters were fabricated. The p contact metal was deposited and alloyed then followed by self-aligned removal of the exposed InGaAs contact material within the absorption window. A mesa was etched until the n contact layer by Inductively Coupled Plasma with a short wet etching ($H_2SO_4:H_2O_2:H_2O=1:1:8$) to remove any damage on the sidewall while removing the damaged surface of the n-doped layer to reduce the contact resistance. A mesa sidewall encapsulation (passivation) using SiN$_x$ was deposited by Plasma Enhanced Chemical Vapour Deposition (PECVD). Ti-Au and Au-Ge-Ni were deposited as the contact metal for the anode and cathode pads respectively. For high speed application, benzocyclobutene (BCB) was used under the anode contact pad to suppress the parasitic capacitance between the pad and the n-doped substrate. Details of fabrication process can be found in Appendix 1

3.3.3 I-V and photoresponsivity characterization

After device fabrication, the basic properties of the PD, such as current-voltage (I-V), dark current, and photoresposivity at room temperature (20 °C) were obtained to profile the material quality.
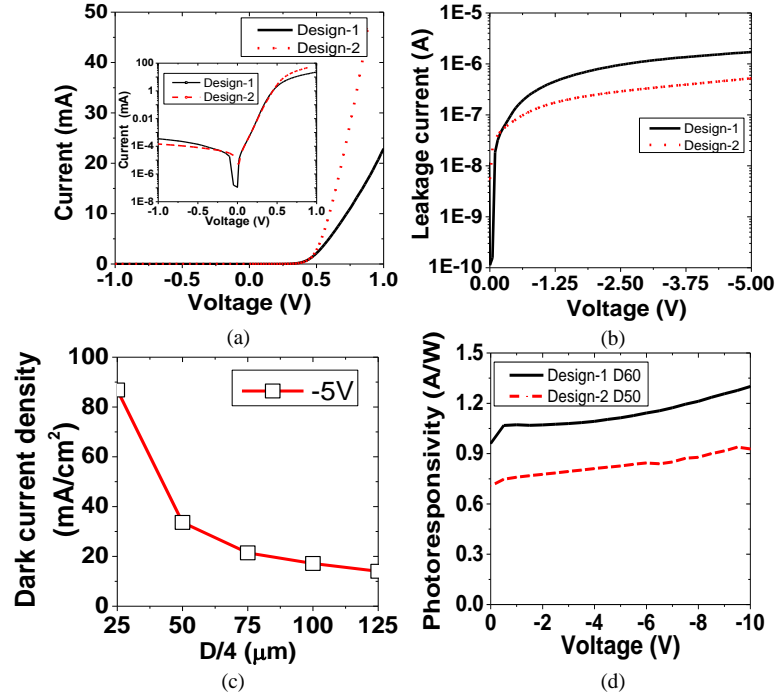
Figure 3.13: *Forward I-V and log |I|-V (inset) of 50 µm diameter mesa (a), reverse leakage of 50 µm diameter mesa (b), leakage density characteristic for mesas from Design-1 material (c) and photoresponsivity (d) for 2 µm surface normal photodiodes at 20 °C.*

The I-V characteristics (Fig. 3.13 (a)) showed diode ideality factors of 1.50-1.52 for both designs, indicating low defect density in the intrinsic layer. These dark current measurement is shown in Fig. 3.13 (b) with leakage as low as 1.7 µA at -5 V bias for 50 µm diameter mesas on Design-1 material. The dark current from mesas with diameters ranging from 100 µm to 500 µm were measured in order to clarify the source of the current leakage. As shown in Fig. 3.13 (c), the leakage density decreased non-linearly with the mesa diameter (D). This suggests that the dark current is mainly generated from the sidewall rather than from the bulk material. We can conclude that the parabolic graded buffer was effective in relieving the lattice mismatch so that the

defects in the intrinsic layer were minimized. To further suppress current leakage from the mesa sidewall, the samples were loaded at 20 °C and the temperature ramped to 300 °C for the mesa PECVD passivation on the Design-2 devices. From Fig. 3.13 (b), we see that the leakage is further reduced to 0.52 µA for 50 µm diameter mesas corresponding to a leakage current density of 26.6 mA/cm^2 at a bias of -5 V.

The photoresponsivity of the photodiodes was obtained by coupling the light from a 2 µm single mode laser (Reference [1]) with a lens-ended fibre. The loss of the fibre was excluded in the responsivity shown in Fig. 3.13 (d). The measured photoresponsivity at 2 µm was up to 1.3 A/W (at -10 V) with the dark current of -8.92 µA for a 60 µm mesa in Design-1 material, which is not far away from the theoretical maximum of 1.6 A/W [6]. The measured photoresponsivity corresponds to a quantum efficiency of 81 % in the 2.5 µm thick intrinsic layer with SiN$_x$ as the anti-reflecting (AR) coating film. When the absorption layer thickness was reduced to 2000 nm (Design-2), for the mesa of 50 µm diameter, the resulting photoresponsivity was up to 0.93 A/W with the dark current of -2.88 µA which corresponds to a quantum efficiency of 58 % at -10 V.

3.3.4 Capacitance and small signal characterization

For high-speed system applications, the modulation bandwidth is a key requirement which is limited by the device capacitance and carrier transit time. Capacitance-Voltage (C-V) measurements were made on devices with BCB so that the capacitance of the p-n junction was dominant. The inset of Fig. 3.14 shows that the capacitance reaches around 0.3 pF when the bias is less than -2 V which means that the background doping of the intrinsic layer is suppressed [7].A corresponding background doping concentrations of 1×10^{15} cm^{-3} for Design-2 is obtained. Although the intrinsic layer thickness of the photodiode of Design-2 material is thinner, the capacitance (C) could be optimized to be nearly the same as that of Design-1 material (mesa diameter 60 µm) by reducing the mesa diameter to 50 µm. A 3-dB Radio Frequency (RF) bandwidth of 10 GHz can be expected, limited by the RC time constant with a 50 Ω load resistor.

To accurately evaluate the operating bandwidth, small modulation signal characterization was carried out on devices mounted on a test sub-mount including a

50 Ω parallel resistor, heat sink, microwave transmission line, and a SMA connector. A lens-ended fiber was used to couple 2 µm wavelength laser light to the top acceptance window of the device. An external $LiNO_3$ Mach–Zehnder Modulator (MX2000-LN-10, Photline) was used to convert the small electrical modulation from a Vector Network Analyzer (VNA) into the optical domain, and hence to analyze the S_{21} parameter (normalized to the pre-characterized background of a commercial photodiode).
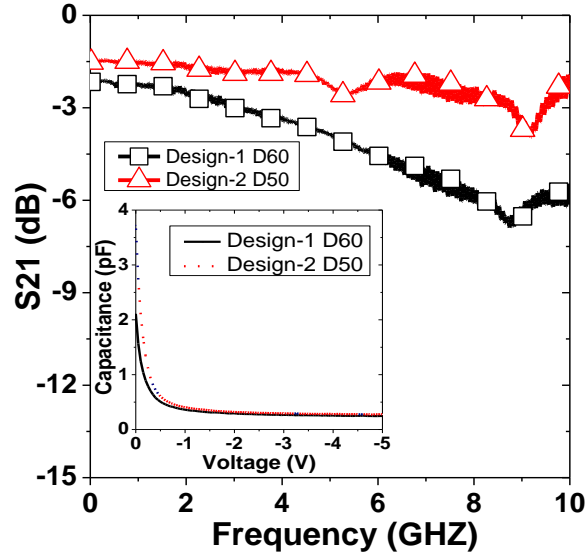
Figure 3.14: *S_{21} characterization results at -10 V tested at 2 µm wavelength; and capacitance versus reverse voltage (inset) for the 2 µm surface normal photodiode with BCB.*

The S_{21} results displayed in Fig. 3.14 show that the devices made from Design-2 material reached a 3-dB cut-off frequency of around 10 GHz at -10 V, limited by the small signal bandwidth of the 2 µm modulator [7]. This was much larger than the devices from Design-1 material which only reached 6.5 GHz. The measured fluctuations in the response are mainly due to electrical reflections between the sub-mount and external RF cable connected to the receiver port of the VNA. Since both devices have nearly the same capacitance, the main reason for the bandwidth limitation is from the carrier transport. The doping modification at the p-cladding layer, removal of the un-doped AlInGaAs layer and the thickness reduction of the intrinsic layer have enhanced the RF bandwidth by facilitating carrier transport over the p-i interface and across the intrinsic layer.

3.3.5 Eye diagram and bit error rate characterization

To analyse the device for use in a practical 2 µm optical high speed communication systems, the eye diagram and the Bit Error Rate (BER) of the fabricated PD were evaluated (Diameter-50 µm, Material of Design-2 with BCB). The setup for this was similar to the RF bandwidth analysis, with a 2 µm laser, followed by the LiNbO$_3$ modulator in the transmitter, a TDFA to amplify the signal from the transmitter, and an attenuator to adjust the input power to the photodiode. An optical filter with a bandwidth of 1.6 nm was also used after the TDFA to suppress the Amplified Spontaneous Emission (ASE) outside the signal bandwidth, minimizing spontaneous bit noise at the detector. Then, the signal light was delivered to the top window of the device by a flat facet fiber adjusted by a manual fiber stage. In addition, the output of the PD was amplified by a RF amplifier (Gain=26 dB, Saturation power=20 dBm) before measurement on a sampling oscilloscope.

(a)   (b)
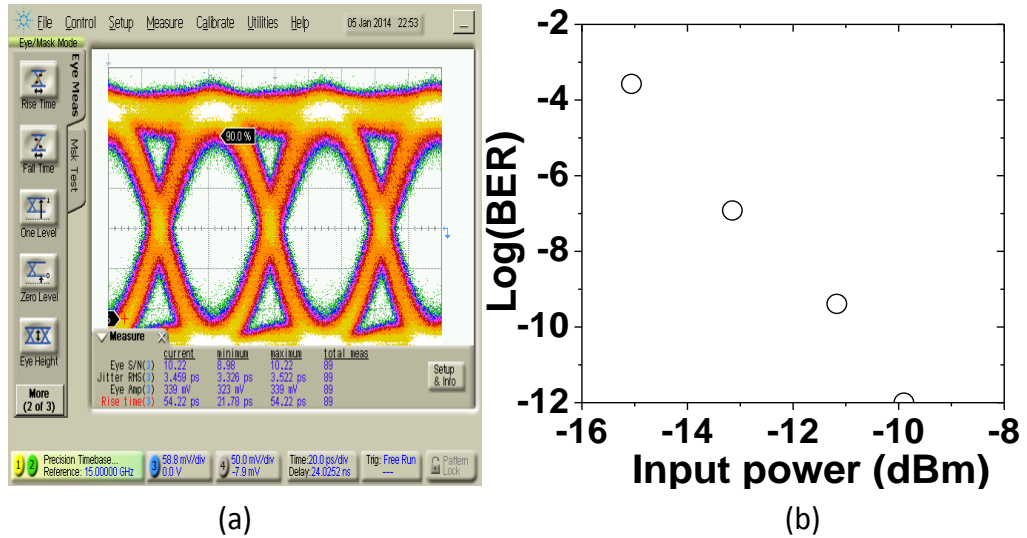
Figure 3.15: *15.6 Gbit/s eye diagram in -3.07 dBm obtained with the PD biased at - 10 V (a); and BER versus input power (b) at 2 µm for the high speed photodiode fabricated on Design-2 material with BCB.*

Fig. 3.15 (a) shows a clear and open eye at an input power of -3.07 dBm under a bias of -10 V with an additional noise source arose from ASE of TDFA. A receiver is proved to be more sensitive if it achieves a specific BER with less optical power incident on it [8]. For our photodetector, a BER as low as 1×10^{-12} was obtained at an

input optical power of -9.9 dBm (Fig. 3.15 (b))[9][10]. Comparing to the latest result of the published photodiode (2 µm wavelength) characterized at 1550 nm (5 Gbit/s) [11], the BER data of our detector is obtained at 2 micron wavelength under much higher modulation speed up to 10 Gbit/s.

3.3.6 Reasons for the large-bias needed to obtain the optimum photoresponse bandwidth and eye diagram results

As it is demonstrated in Fig. 3.13, Fig. 3.14 and Fig. 3.15, those optimum results of the photodetector related to the photoresponsivity, small signal working bandwidth and eye pattern characterizations are obtained under the high voltage reverse bias up to 10 V.

One of the possible reasons is the offset between the valence band of the InGaAs absorber and the one for the AlInGaAs cladding layer which protects the hole's transporting to the anode. This is similar to the case of the ridge waveguide photodetecor made of QW_2 material which contains AlInGaAs in the QW region and non-doped InP as the cap layer (See the section 3.2.3).
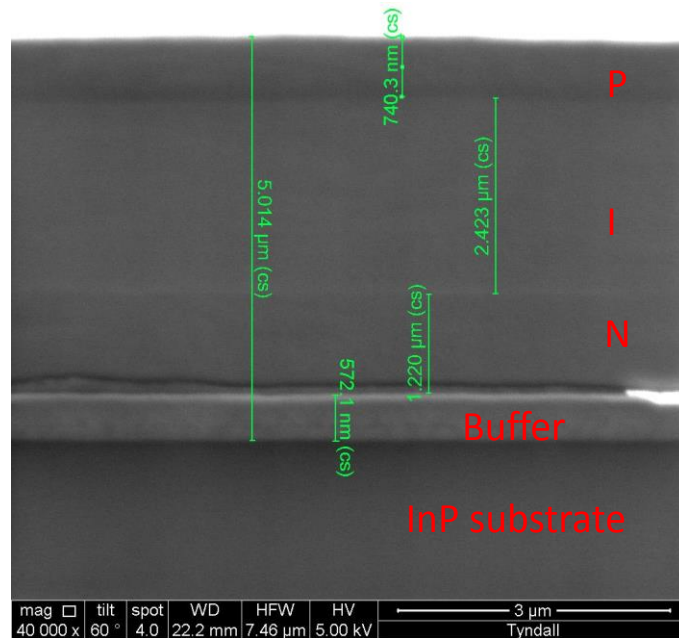
Figure 3.16: *SEM photo of the layer stacks for the grown Type-2 material*

In addition, the background doping within the intrinsic layer due to both of the defects diffusion generating from lattice-mismatching and dopant diffusion from the N layer can increase the bias-voltage cost (for the voltage value referring to the delepletion starting point) to achieve the optimum depletion width. Material optimization like introducing a graded buffer in the intrinsic layer/p cladding interface and using a diffusion-protection layer between the N and intrinsic layer could be investigated together with the calibration of the MOCVD growth accuracy to further decrease the biased-voltage in the future.

3.3.7 Comparison between the ridge type waveguide and surface normal type mesa photodiode.

Both types of photodiodes in ridge waveguide geometry and surface normal schematic have been fabricated and characterized in the last sections. Comparing the main performances of those two kinds of devices are necessary to check which is more suitable for the optical system application around 2 µm wavelengths.We can see from Fig. 3.17 (b) that the photoresponse of the surface normal type photodiode could be as high as ~0.75 A/W (-3 V) even up to 0.93 A/W (-10 V) which is much higher than the ridge waveguide type (0.38 A/W, -3 V) though the leakage density of the former is around twenty times of the latter (see Fig. 3.17 (a) and Table 3.2).
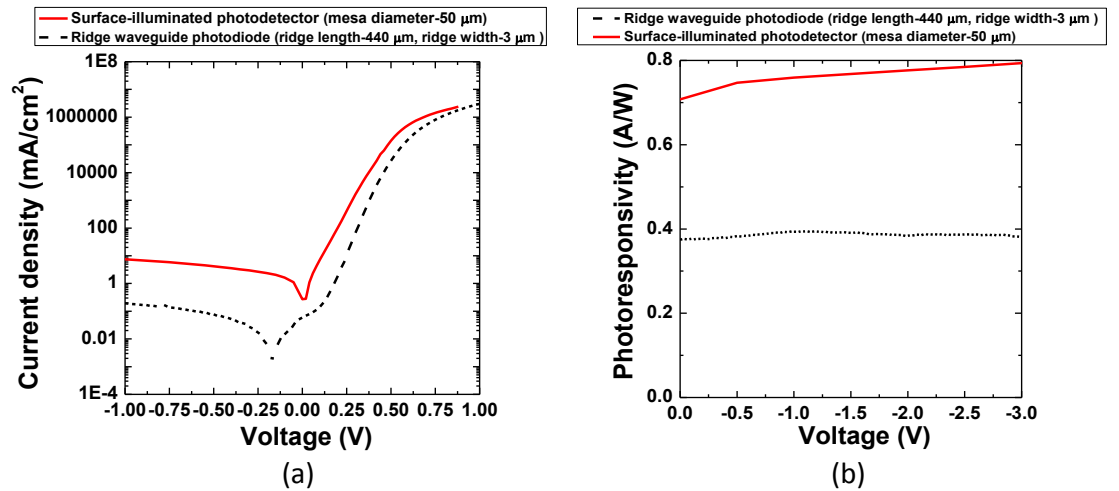
Figure 3.17: *Current density (a) and photoresponsivity at 2 micron wavelength (b) varied with biased voltages for different types of photodiodes.*

Considering that the ASE noise of the optical amplifier could be the main noise source comparing to the noise from the dark current in the receiver end, the signal recovering ability referring to the detector photoresponsivity would determine the SNR after the conversion of light to current, a surface normal type photodiode is more suitable to be used in the real system. benefiting from the circular aperture which is mode-matched with the coupling fiber.

Table 3.2: Main parameters for the ridge waveguide and surface normal types of 2 µm photodiodes

	Ridge waveguide	Surface normal
Serial resistance (Ω)	9.17	7.72
Ideality factor	1.37	1.52
Maximum photoresponsivity (A/W)	0.38	0.93
Leakage density at -3 V (A/cm^2)	0.0008	0.0168

3.4 Balanced photodiode based on the surface-normal type detector

A balanced photodetector can be used to achieve the differential detection for further suppressing the relative intensity noise (RIN). As it is shown in Fig. 3.18, the device has been designed based on the serial connection of two single surface-normal type detectors taking advantage of the high coupling efficiency.
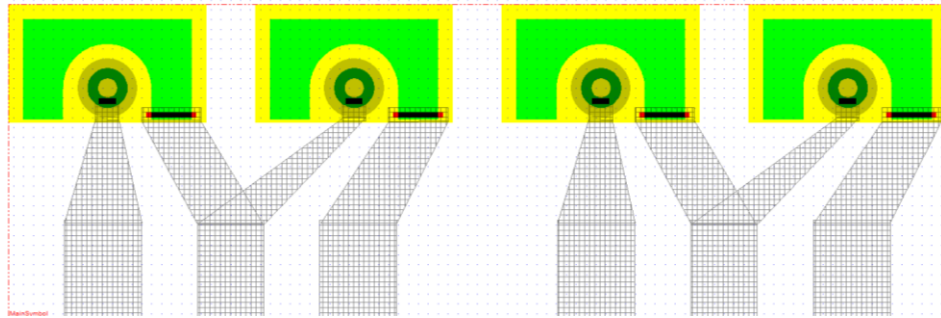
Figure 3.18: *Mask pattern design for the 2 µm balanced photodiode.*

Due to the high electrical isolation requirement between the two mesas, semi-insulating substrates are required to protect the potential short circuit of the p and n

contact after linking the paired photodiodes via metal connection. With the same epitaxial layer design as the Design-2 shown in Table.3.1, the new material was grown on the semi-insulating substrate with an InP(100 nm)/InGaAs(2 nm)/AlInAs(15 nm) buffer in between as the diffusion-stop layer to protect the dopant diffusing from the n layer into the semi-insulating substrate. The balanced photodetector working at 2 µm wavelengths was fabricated following the main steps of the process flow similar to the fabrication of the high speed surface normal photodiode. To further suppress the extra dark current and simplify the process, dry etching steps are optimized. First, the larger mesa pattern was etched until the N layer. Then, the intrinsic mesa and N contact mesa (until the semi-insulating substrate) was able to be achieved at the same time in the following etching process by using a smaller (inner) mesa pattern and sharing the same SiO_2 hard mask. No extra hard mask deposition was needed and the sidewall surface could avoid a risk of failure for the coverage of SiO_2 hard mask layer which is different from the final passivation layer of SiN_x. Schematics showing the main process steps are demonstrated as Fig. 3.19 and details can be found in Appendix 2.
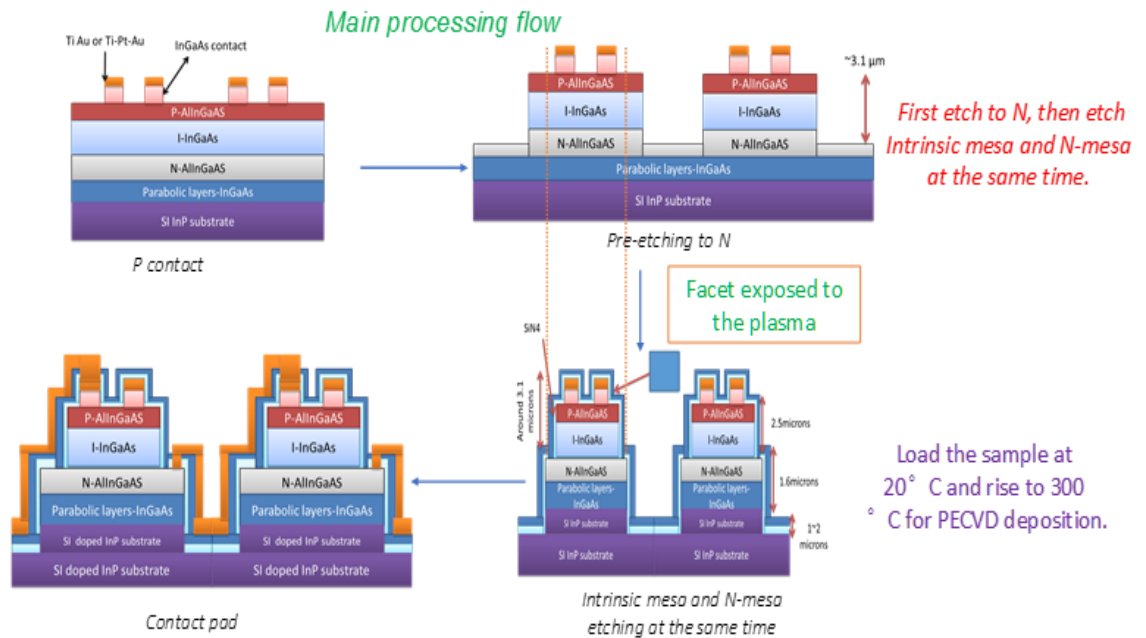
Figure 3.19: *Main process steps for the 2 µm balanced photodiodes.*

As it is shown in Fig. 3.20, the device was successfully fabricated with electrical contact connection from the p contact of one single photodiode to the n contact of the other one.
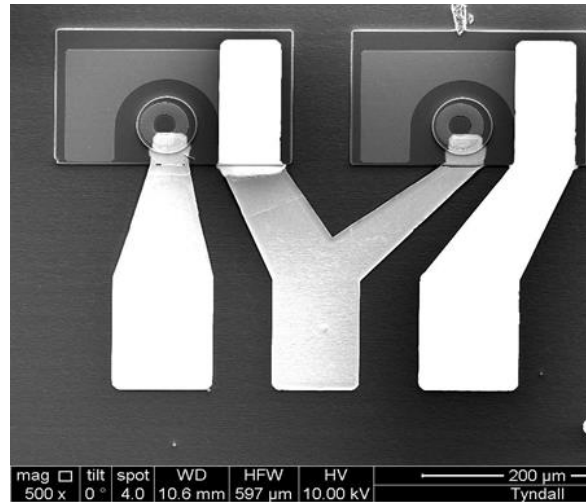
Figure 3.20: *SEM graph of the top view for the fabricated balanced photodetector at 2 micron wavelength based on the surface normal type paired photodiodes in serial connection.*

Stripe mesas are also fabricated at the same run and cleaved for taking the SEM photo on the transverse section to check the process results.
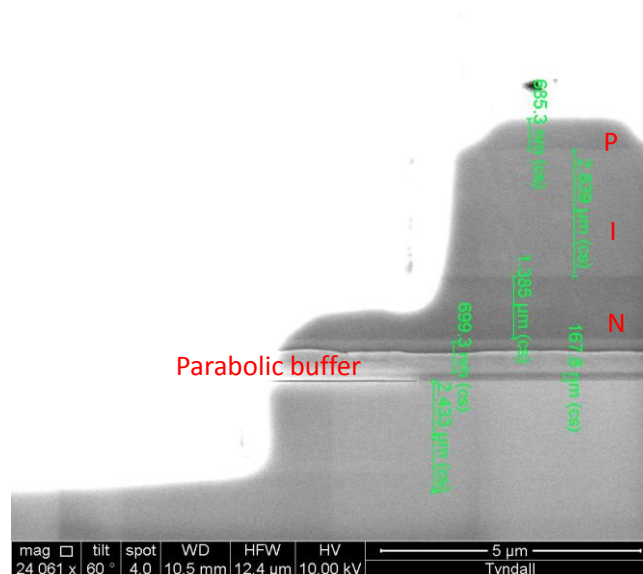
Figure 3.21: *SEM graph of the transverse section for the stripe mesa with the same material and processed at the same run of 2 µm balanced photodiode.*

From Fig. 3.21, we can see that the intrinsic layer has been etched through demonstrating a thickness of ~2.839 µm while an over-etch of ~2.433 µm deep into the semi-insulating InP substrate is achieved.

I-V characterization demonstrated a leakage of -10.4 µA under -7 V for one single device (Diameter: 50 µm) within the paired photodiodes.
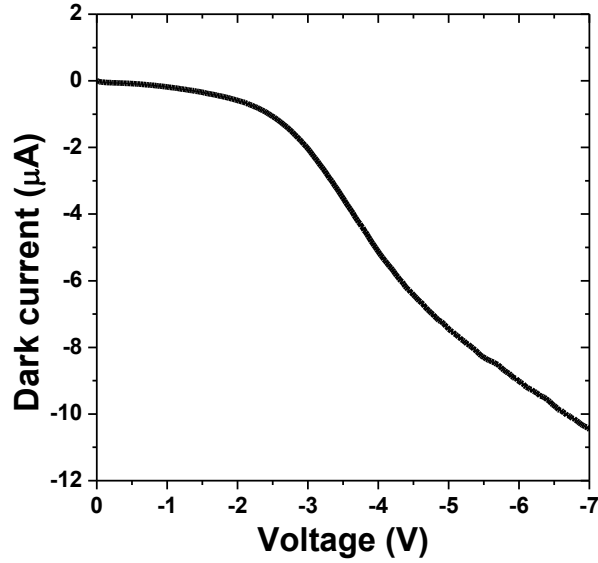
Figure 3.22: *Dark current under differnt bias voltage for one of the single photodiodes (Diameter: 50 micron) within the 2-µm wavelength surface normal balanced photodiode..*

The leakage of the single detector within the 2 micron paired balanced photodiode is approximately one order higher comparing to the surface normal high speed photodiode with the same mesa diameter of 50 micron. This may be due to the p contact ring closing to the mesa edge and the larger side wall area exposed to the dry etching plasma from the intrinsic layer thickness (~2.839 µm) shown in Fig. 3.21.

The CV result of this device obtained under different reverse biases are shown in Fig. 3.23. A capacitance of 1.11 pF (single detector) expected to a bandwidth of 2.87 GHz (assuming the total serial resistance is 50 Ω) is able to be obtained at the same bias voltage.
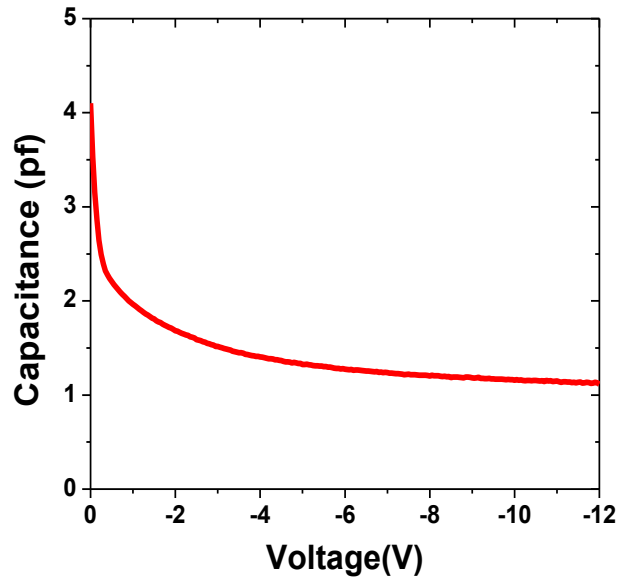
Figure 3.23: *Capacitance under differennt bias voltages for one single device (diameter 50 µm) within the paired balanced photodiode at 2 µm wavelengths*

Its capacitance at -7 V is much higher than the one for the 50 µm diameter high speed photodiode which is around 0.3 pF under the same bias. The extra parasitic capacitance may come from the current leakage generated from the roughness of the semi-insulating substrate after the process.
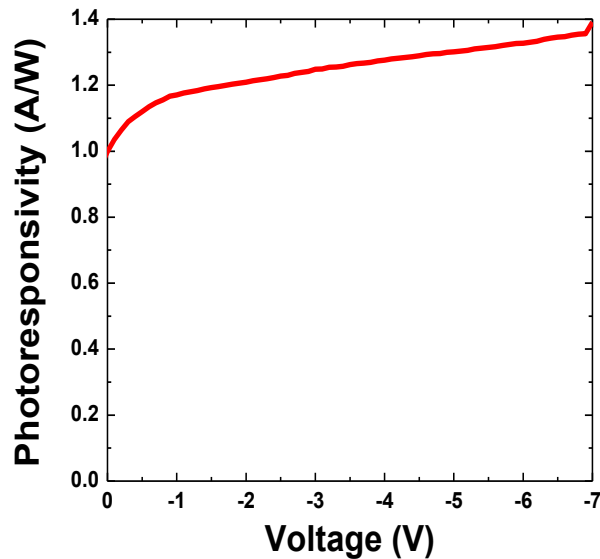
Figure 3.24: *Photoresponsivity changed with bias voltage for one single photodiode (Diameter: 50 micron) in the paired balanced photodiode at 2 µm wavelengths.*

This can be solved by stopping the dry etching on the level which is a few hundred nm up from the semi-insulating substrate and finish with selective wet etch to remove the remaining epitaxial material and leave a smooth slightly over-etched substrate surface. Another way to further reduce the capacitance is cleaving part of the contact pad for shrinking the effective area of the parasitic capacitance.

The thick intrinsic layer helps the light absorption efficiency to provide a large photoresponsivity. As it is shown in Fig. 3.24, the photoresponsivity of the single device is enlarged to 1.39 A/W when the device is biased at -7 V.

3.5 Conclusion

In this chapter, we have demonstrated the edge-coupled high speed photodiodes based on strained $In_{0.74}Ga_{0.26}As/In_{0.53}Ga_{0.47}As$ (QW_1) and $In_{0.82}Ga_{0.18}As/AlInGaAs$ (QW_2) quantum wells for operations at the 2 µm wavelength region. The fabricated device in QW_1 material has a leakage current as small as 2.55 nA at -1 V bias and responsivity of 0.38 A/W under -3 V bias at 2000 nm excluding the fibre loss. The packaged device shows a 3 dB bandwidth up to 12.9 GHz characterized at 1550 nm. For the surface illuminated type photodetector, by introducing a high quality parabolic-graded buffer layer and AlInGaAs cladding layers in the material design, a sensitive 2 µm InGaAs surface normal photodiode has been achieved with the 2 micron wavelength photoresponsity up to 0.93 A/W. In addition to high photoresponse and low leakage current, a high speed device was successfully obtained by optimizing the layer doping and thickness. We show successful operation at 15.6 Gbit/s, with a clear eye diagram while maintaining a BER of $1x10^{-12}$ for -9.9 dBm input power at 2 µm wavelength. A balanced photodiode was also achieved based on the paired top-illuminated type photodetectors in serial connection. One single device in the paired photodiodes demonstrated a leakage current of -10.4 µA under -10 V and photoresponsity of 1.39 A/W when biased at -7 V. Further work should be focused on the etching process optimization to suppress the extra parasitic capacitance and the package design together with the 90º optical hybrid to achieve the coherent detector scheme for the detection of higher order modulated format in the real optical commuincation system at 2-µm wavelengths.

3.6 References

[1] R. Phelan , J. O'Carroll, D. Byrne *et al.*, "In$_{0.75}$Ga$_{0.25}$As/InP multiple quantum-well discrete-mode laser diode emitting at 2 μm," *Photonics Technology Letter IEEE*, vol.24, no.8, pp. 652–654, 2012.

[2] Y. Hua, N. Ye, M. Manganaro *et al.*, "High speed AlInGaAs/InGaAs quantum well wave guide photo diode for wavelengths around 2 microns," in *International Conference on Indium Phosphide and Related Materials*. Aug. 2012.

[3] A. Wieczorek, V. Djara, F.H. Peters *et al.*, "Inductively coupled plasma deep etching of InP/InGaAsP in Cl2/CH4/H2 based chemistries with the electrode at 20°C," *J. Vac. Sci. Technol. B*, vol. 30, no.5, pp. 051208, Aug 2012.

[4] H. Yang, N. Ye, R. Phelan *et al.*, "Butterfly packaged high-speed and low leakage InGaAs quantum well photodiode for 2000 nm wavelength systems," *Electronics Letter*, vol.49, no.4, pp. 281-282, Feb. 2014.

[5] A Gocalinska, M Manganaro, E Pelucchi, *et al.*, "Suppression of threading defects formation during Sb-assisted metamorphic buffer growth in InAs/InGaAs/InP structure," *Applied Physics Letter*, vol.100, pp.152112, Apr. 2012.

[6] K. W. Busch, M. A. Busch,. "Introduction to photoelectronic detection", Multielement detection systems for spectrochemical analysis, John Wiley & Sons, 1990, pp.372-373.

[7] H. Zhang, Z. Li, N. Kavanagh, *et al.*, "81 Gb/s WDM Transmission at 2μm over 1.15 km of Low-Loss Hollow Core Photonic Bandgap Fiber," in *Optical Communication European Conference (ECOC)*, Cannes, France, 2014, pp.p.5.20.

[8] G. P. Agrawal, "Signal Recovery and Noise", *Lightwave technology: telecommunication systems*, John Wiley & Sons, 2005, pp.158.

[9] N. Ye, M. R. Gleeson, M. U. Sadiq, *et al.*, "InP-Based Active and Passive Components for Communication Systems at 2 μm," *Journal of Lightwave Technology*, vol.33, no.5, 2015, pp. 971-975.

[10] N. Ye, H. Yang, M. Gleeson, *et al.*, "InGaAs Surface Normal Photodiode for 2 μm Optical Communication Systems," *Photonics technology letters* IEEE, vol.27, no.14, pp.1469-1472, Jul. 15, 2015.

[11] A. Joshi, S. Datta, "High-speed, large-area, p-i-n InGaAs photodiode linear array at 2-µm wavelength," in *Defense, Security, and Sensing*, the international society for optics and photonics (SPIE), vol.83533, Maryland, USA, pp.83533D, 2012.

Chapter 4 90° optical hybrid working at 2 μm region

4.1 Introduction

In order to achieve higher capacity at 2 μm wavelength, advanced order modulation formats such as QPSK or QAM needs to be applied to optimize the spectral efficiency. Recovering the In-phase and Quadrature (IQ) information of this signal requires coherent detection by use of a suitable 90° optical hybrid at a specific wavelength range. The function of this kind of device is to combine the incoming signal with the local oscillating source to generate a quadrature phase relationship at the output followed by a pair of balanced photodiode to demodulate the I/Q part of the QPSK or QAM signal separately. The waveguide-based MMI coupler structure is of special interest due to that it can be conveniently integrated with other active or passive elements on the same chip by the planar semiconductor fabrication processing. Benefitting from the self-imaging property of the multimode waveguide, a simple rectangular coupler has been achieved which can image the input mode field distribution onto the output ports periodically along the waveguide length. When any two asymmetric entrance ports are selected as the inputs, each of the 4 output ports demonstrates an equal amplitude with a 90° phase difference between them. In this chapter, we present the design, optimization and characterization of a 90° optical hybrid based on the MMI general inference scheme (From the theory scheme side, it is explained as 4×4. From the device physical structure side, it can also be explained as 2×4 if the number of input and output ports are considered) for the operation around 2 μm wavelengths. In addition, as the main building block, a single mode diluted optical waveguide is shown with a large spot size for improving the light coupling between the waveguide and the 2 μm optical fibres. Analysis on the epitaxial layer, device design, fabrication process, and evaluation test are carried out to estimate the reason of loss and deviations away from the original simulation results.

4.2 Diluted waveguide at 2 micorn wavelength

4.2.1 Waveguide design and simulation

To ensure high coupling efficiency between the MMI and a single optical fiber, the epitaxial structure of the waveguide is designed to take account the mode mismatch between the fibre and ridge waveguide facet. This is achieved by introducing a diluted waveguide, expanding the mode distribution along the layer growth direction [1] to form a near circular mode shape and large spot size matching the transmisson mode of the single mode fiber.

Here, we propose a waveguide based upon a lattice matched quaternary compound of InGaAs$_y$P$_{1-y}$ where y is equals to 0.43 corresponding to a bandgap of λ_g =1.117 µm. At 2-µm wavelength, this material has a refractive index of 3.2837 while InP has an index of 3.1527 based upon the Adachi model which is used in FIMMWAVE software. A diluted waveguide with quaternary insertions minimises the thickness of quaternary needed and thus eases the requirement on precise lattice matching for a large thickness.

Table 4.1: 2 micron diluted waveguide layers structure

Thickness (nm)	Material
1000	InP
150	InGaAsP ($\lambda_g = 1.117$ µm)
700	InP
150	InGaAsP ($\lambda_g = 1.117$ µm)
700	InP
150	InGaAsP ($\lambda_g = 1.117$ µm)
700	InP
150	InGaAsP ($\lambda_g = 1.117$ µm)
Substrate	InP

As it is shown in Table.4.1, an epitaxial wafer structure which includes four InGaAsP layers separated by 700 nm-thick InP layers is used to achieve a transverse mode size of more than 3.6 µm in the vertical direction. Simulation results from the FIMMWAVE software indicates that a 4 µm wide, 5.5 µm deep ridge diluted waveguide is able to achieve single mode operation (Fig. 4.1) with an effective index of ~3.16 but with a small birefringence (~1×10^{-3}) for both TE and TM polarization at the wavelength of 2 µm (Table 4.2).

Table 4.2: Simulated effective and group index values for the diluted waveguide structure

Polarization	Ridge width (µm)	Effective index (n_r)	Group index	Vertical Width (µm)	Horizontal Width (µm)
TE	4.0	3.16136	3.277	3.6410	3.0594
TM	4.0	3.16061	3.273	3.6927	3.2214

The effective index variation due to etch depth change is also simulated by use of the same software platform. With the fixed ridge width of 4 µm, the effective index would like to be slightly decreased (1×10^{-4}) when the etching depth is increased but it becomes stable when the depth is more than 5 µm for both polarization states. This can be visualized by recording the effective index of each etch depth which is presented in Fig. 4.2. Therefore, we can estimate the proper depth limitation for the etch process during the device fabrication which should be no less than 5 µm.

(a)   (b)
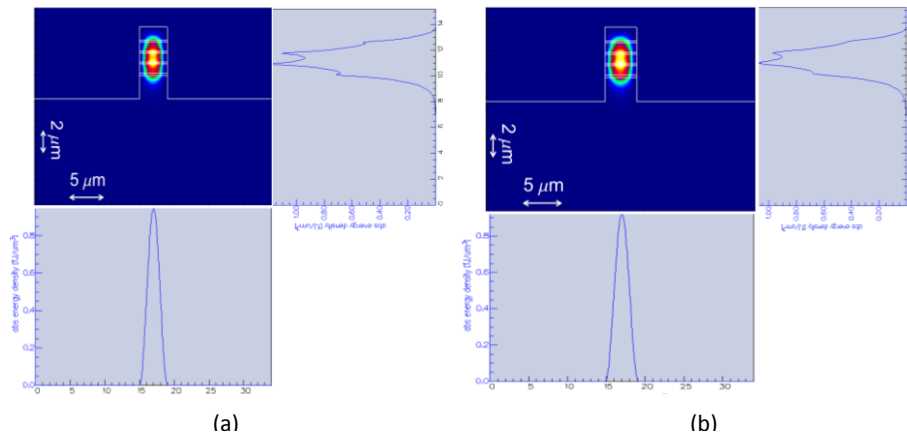
Figure 4.1: *Simulated modes of a diluted waveguide with the ridge width of 4 µm and depth of 5.5 µm at 2-µm wavelength. (a) TE mode (b) TM mode*
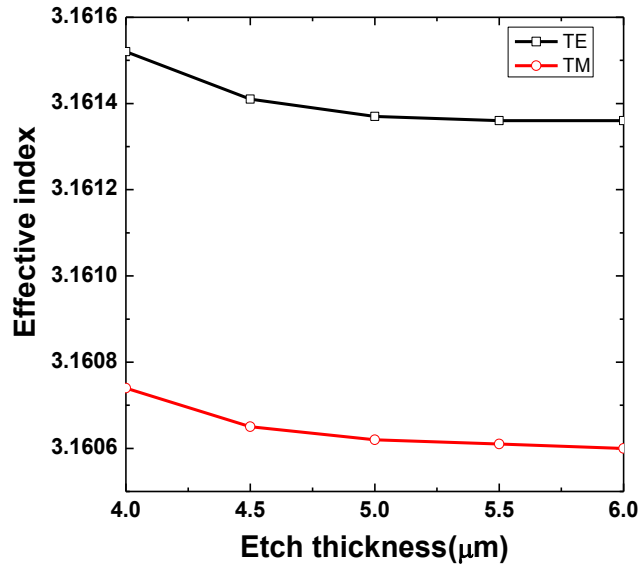
Figure 4.2: *The effective index variated with the etch depth for the 4 µm wide diluted waveguide at 2-µm wavelength. (a) TE mode (b) TM mode*

The etching depth may also affect the potential cross talk between two adjacent waveguides in parallel with each other. When the two waveguides come close to each other, the whole structure can be seen as a simple directional coupler and the leakage light from one waveguide would become the cross talk for the other. As it is shown in Fig. 4.3 and Fig. 4.4, a mode confined in the input waveguide would be partly coupled into the parallel waveguide (coupling waveguide) after transporting a distance of 1 cm. Simulation results from the FIMMPROP software reveal that the cross-talk could be suppressed when the etching depth is increased.
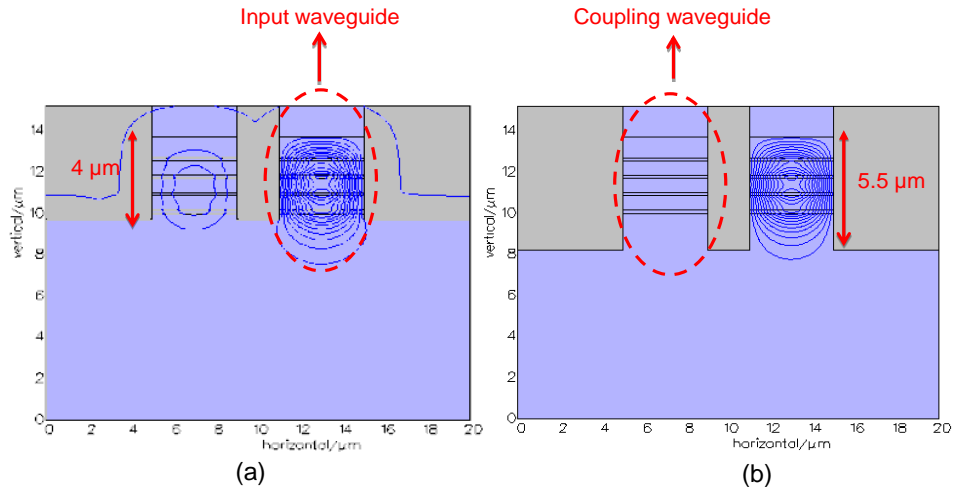
Figure 4.3: *Cross talk dependence on etching depth ((a)4 µm and (b) 5.5 µm) for the adjacent 4-µm wide diluted waveguides in TE mode at 2-µm wavelength.*

88

From Fig. 4.3 and Fig. 4.4, we could see that the isolation between the adjacent waveguides (interspacing 2 µm) is obviously improved when the etching depth is increased from 4 to 5.5 µ m corresponding to the cross talk from -14.32 to -42.36 dB for Transverse-Electric (TE) mode and from -13.59 to -40.50 dB for Transverse-Magnetic (TM) mode.
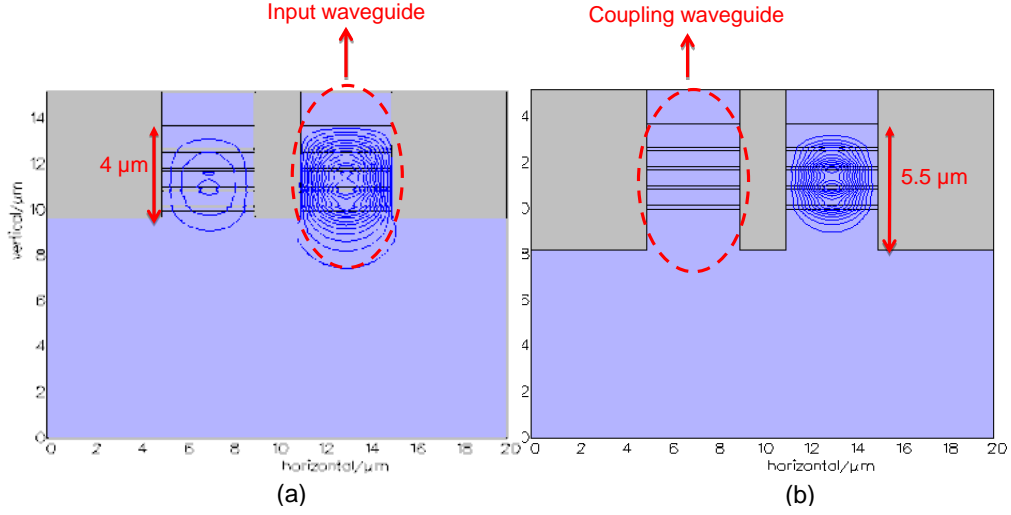
Figure 4.4: *Cross talk dependence on etching depth ((a) 4 µm and (b) 5.5 µm)) for the adjacent 4-µm wide diluted waveguides in TM mode at 2 µm wavelength.*

4.2.2 Waveguide fabrication and characterizaiton

To realise the diluted waveguide structure, deeply-etched ridge waveguides with the depth of > 5 µm and width of 4 µm were fabricated using III-V device process mainly focused on the optimization of inductively-coupled plasma etching [2]. A hard mask of 600 nm SiO_2 followed by 100 nm SiN_x was deposited by Plasma Enhanced Chemical Vapour Deposition (PECVD) at 300 °C. After spinning the photoresist (PR) of AZ5214E, the wafer was exposed with mask aligner under the Ultraviolet (UV) light source and developed in the solvent of AZ400K/DI to reveal the PR pattern. This pattern was transferred to the hard mask by dry etch with a gas of CF_4/CHF_3 in a STS ICP system. To clean the photoresist after the hard mask formation, the sample was etched by an O_2 plasma and put into 1165 solvent at 90 °C. Then, it was held on a silicon carrier wafer and using an Oxford ICP etch system, the epitaxy layers were etched by a gas recipe of $Cl_2/CH_4/H_2$ (10:18:12 sccm). As it is shown in Fig. 4.5, a

smooth side wall after the dry etch has been obtained by taking the SEM graph. After dipping the sample in the Buffered Oxide Etchant (BOE) to remove the remaining dielectric layer, a 600 nm-thick SiO₂ layer was deposited by PECVD as a protective layer on the top and sidewall of the diluted waveguide. Finally, waveguides were cleaved into different lengths for the characterization.
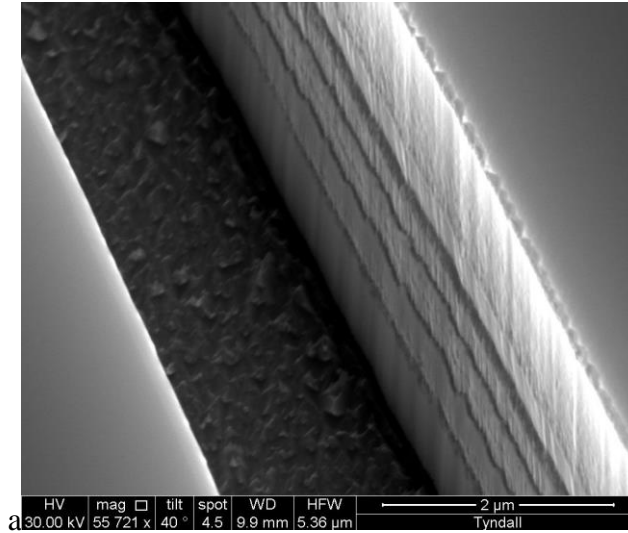
Figure 4.5: *SEM graph for the side wall of the diluted waveguide at 2-µm wavelength after dry etch.*

Transmission spectra from the cleaved waveguides were characterized and analysed to estimate the transmission loss due to the roughness of the waveguide side wall and coupling loss from the mode mismatch between the waveguide acceptance aperture and the coupling fiber. By using a 2 µm lens-ended fibre, broad band light covering 2 µm wavelengths generated from the Amplified Spontaneous Emission (ASE) of a TDFA was optimally coupled into the ridge of the diluted waveguide. The transmitted light at the output was then coupled into an Optical Spectrum Analyser (OSA) using the same type of lens-ended fibre and the resulting Fabry-Perot (FP) fringes were monitored. Those output results are normalized to the input ASE broad band spectrum to remove the background so that the pure effect of the cavity based on diluted waveguide could be abstracted to further deduce the factors affecting the total loss of the waveguide.

4.2.3 Methods for deducing waveguide loss

As an uncoated single-mode waveguide can be treated as a Fabry–Pérot (FP) cavity, the corresponding power transmission behaviour can be modeled based on the Airy transmission function which describes the transmission spectrum of the standard FP resonator [3]. Therefore, the transmission spectrum T_{FP} for a single mode waveguide could be explained in Eq. 4.2.1 as follows:

$$T_{FP} = \frac{T^2 \times e^{-\alpha L}}{(1-\hat{R})^2 + 4\hat{R}\sin^2(\Phi/2)} \times \eta \qquad (4.2.1)$$

Where R is the facet reflectivity used in the Fresnel formula of $R = (\frac{N_{eff}-1}{N_{eff}+1})^2$ considering the waveguide end as a perfect facet. T represents the end-facet transmission which could be obtained through the conservation relationship of $T = 1 - R$. The loss of $\hat{R}$ involves the combination of the facet reflection R and the mode propagation intensity loss of α in the form of $\hat{R} = R \times e^{-\alpha L}$. η is the coupling efficiency. The total phase Φ of the transmission fringes can be presented as $\Phi = 2k_0 N_{eff} L + \Phi_0$, with Φ_0 as the natural phase deviation; k_0 as the free space wave number ordinarily expressed in $k_0 = \frac{2\pi}{\lambda_0}$, N_{eff} as the effective index of the transmission mode, and L as the waveguide length.

From the output spectrum, we can abstract the $\hat{R}$ by Eq. 4.2.2 from the maximum and minimum value of the periodically varying transmission shown in Fig. 4.6:

$$K = \frac{(T_{max}-T_{min})}{(T_{max}+T_{min})}, \hat{R} = \frac{(1-\sqrt{1-K^2})}{K} \qquad (4.2.2).$$

Then the propagation loss can be expressed as:

$$\alpha = \frac{\ln\left(\frac{R}{\hat{R}}\right)}{L} \qquad (4.2.3).$$

Other parameters such as coupling loss can be deduced by fitting the spectrum with the power transmission function of Eq. 4.2.1 based on the least squares method[3].

For our 2 µm wavelength diluted waveguide, it will be a challenge to apply the above-mentioned theory not only due to that it is difficult to obtain the accurate value of the refractive index for the layer with the epitaxial material at this wavelength range but also as that the reflectivity is hard to calculate due to the failure of effective index approximation for the semiconductor waveguide indicated by reference No.3. In addition, one fixed value of $\hat{R}$ can refer to several pairs of R-α combinations due to the relation of $\hat{R} = R \times e^{-\alpha L}$.

Furthermore, resulting from this relationship, small change in the reflectivity would cause a large variation for the fitted value of propagation loss along the waveguide. It can be seen from Fig. 4.6 that the fitted value of the transmissions loss α variates from 1.9339 dB/cm (Fig. 4.6 (a)) to 6.0584 dB/cm (Fig. 4.6 (b)) presented from the red-high-lighted part at Table.3 when the facet reflectivity is changed from 0.2677 to 0.25 (high-lighted in green at Table 4.3), even though both of the fitted curves are quite converged to the original transmission spectrum from the 1.6 mm long diluted waveguide around 2 µm wavelengths by use of the two different R-α groups.
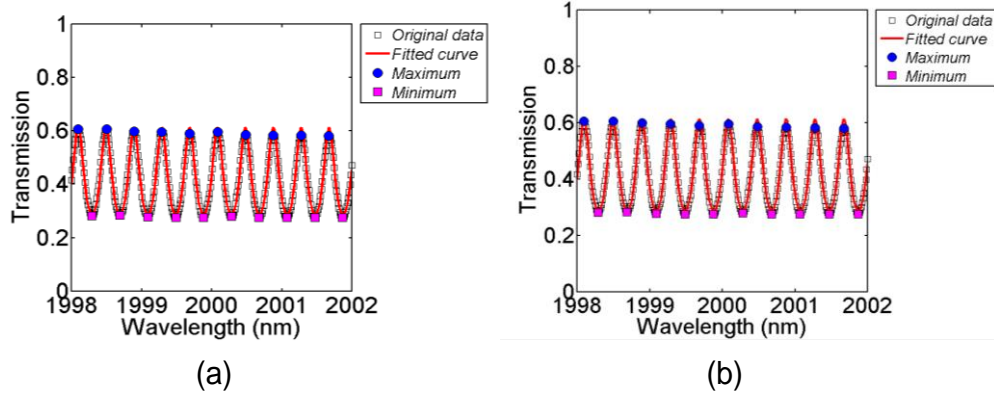
Figure 4.6: *Light power transmission changed with wavelengths around 2 µm and corresponding fitting results with reflectivity of 0.2677 (a) and 0.25 (b) for 1.6mm long diluted waveguide.*

Table 4.3: Fitted results with different reflectivity for the 1.6 mm long diluted
waveguide

Reflectivity	α (/cm)	Transmission loss(dB/cm)	Coupling loss(dB)	Fitted effective index
0.2677	0.4453	**1.9339**	0.913	3.144
0.25	1.395	**6.0584**	0.4605	

To deduce the transmission loss independent of the reflectivity effect, an involved
method has been developed by taking account of both transmission and reflection
spectrum from the same waveguide [4]. As it is shown in Eq. 4.2.4, the ratio of
reflection relative to the transmission for a single-mode waveguide cavity can be
presented as follows:

$$\frac{R_{FP}}{T_{FP}} = \frac{\left(1+e^{-2\alpha L}-2e^{-\alpha L}\cos(\Phi)\right)R}{T^2 e^{-\alpha L}} \tag{4.2.4}$$

Where, R_{FP} is the power reflection of a single-mode waveguide which can be
modeled as a FP cavity and other parameters have the same meaning as Eq. 4.2.1.
From this formula, we can see that the coupling loss has been excluded by such
division operation.

When Φ equals to $2 m\pi$ ($m = 1,2 ... ...$), the function will be:

$$\frac{R_{FP}}{T_{FP}}_{(\Phi=2m\pi)} = \frac{(1-e^{-\alpha L})^2 R}{T^2 e^{-\alpha L}} \tag{4.2.5}.$$

When Φ equals to $(2m + 1) \pi$, the function will be:

$$\frac{R_{FP}}{T_{FP}}_{(\Phi=(2m+1)\pi)} = \frac{(1+e^{-\alpha L})^2 R}{T^2 e^{-\alpha L}} \tag{4.2.6}.$$

Combine the last two equations, we have the new formula as follows:

$$\frac{\frac{R_{FP}}{T_{FP}}_{(\Phi=2m\pi)}}{\frac{R_{FP}}{T_{FP}}_{(\Phi=(2m+1)\pi)}} = \frac{\left(1-e^{-\alpha L}\right)^2}{(1+e^{-\alpha L})^2} = tanh^2\left(\frac{\alpha L}{2}\right) \qquad (4.2.7).$$

Note that the waveguide cavity facet reflectivity R has been removed.

Meanwhile, according to the physical meaning of R_{FP} and T_{FP} when Φ equals to $2\,m\pi$ or $(2m+1)\,\pi$, we can have this function in another form of:

$$\frac{\frac{R_{FP}}{T_{FP}}_{(\Phi=2m\pi)}}{\frac{R_{FP}}{T_{FP}}_{(\Phi=(2m+1)\pi)}} = \frac{I_{R_{min}}I_{T_{min}}}{I_{R_{max}}I_{T_{max}}} \qquad (4.2.8)$$

Where, $I_{R_{min}}$ ($I_{R_{max}}$) and $I_{T_{min}}$ ($I_{T_{max}}$) are the minimum (maximum) value of reflective and transmitted intensity in the resulting spectrum fringes respectively.

Therefore the final expression related to the waveguide propagation loss could be:

$$tanh^2\left(\frac{\alpha L}{2}\right) = \frac{I_{R_{min}}I_{T_{min}}}{I_{R_{max}}I_{T_{max}}} \qquad (4.2.9).$$

It is clear that the propagation loss of the diluted waveguide can be deduced from Eq. 4.2.9 by introducing the averaged maximum/minimum value from the transmission and reflection spectrum after the waveguide [4].

A simple setup as shown in Fig. 4.7 (a) was built to characterize the transmission and reflection properties of the 2 µm diluted waveguide with the broad band light source from the TDFA. An optical circulator working around 2 micron wavelengths was achieved by using the isolator to block the reflected light travelling to the soucce while the 1×2 coupler leads the light (refelected) to go to the other port. The resulting output were collected by a 2 µm Optical Spectrum Analyser (OSA) and normalized to the background spectrum of the TDFA, which is displayed in Fig. 4.7 (b). Then, the peaks and valleys were located to obtain the averaged maximum and minimum so that we can have the transmission loss of α which equals to 17.06 dB/cm or -3.93 /cm.
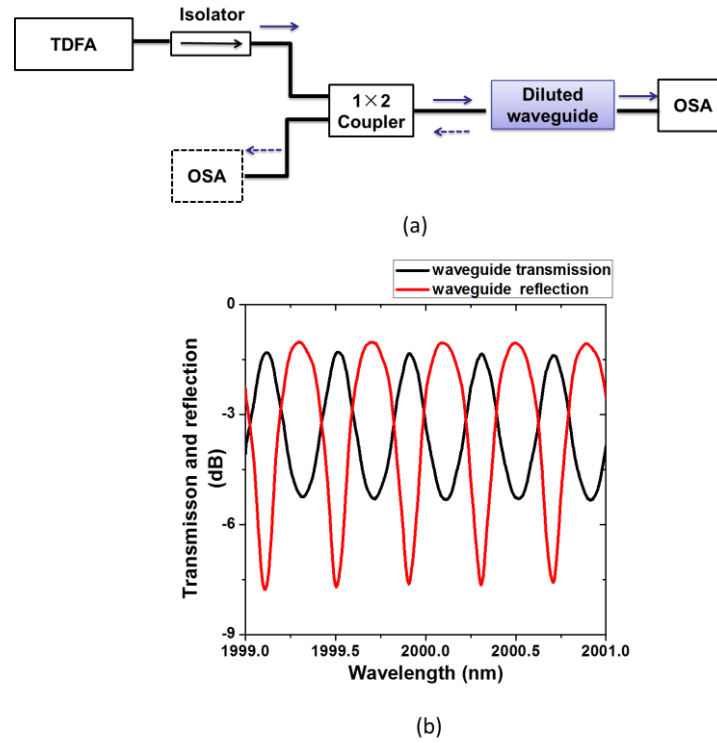
Figure 4.7: *Light power reflection and transmission characterization used to obtain the loss of the diluted waveguide around 2-µm wavelengths. (a) Test setup with an optical isolator and a 1×2 coupler, (b) Spectras for the light which transmits through and reflects back from the 2-µm wavelength diluted waveguide.*

Obviously, this method requires a shot waveguide cavity length to provide sufficient numbers of peaks and valleys in the transmission spectrum. This suffers from the non-uniform quality of the wavguide cut from different regions of the wafer.

Generally, having the estimation of the average propagation loss and facet coupling loss are appropriate to evaluate the waveguide quality for further fabrication of waveguide-based passive devices. By suppressing the reflection loss of a waveguide, we can approximately qualify the average propagation loss and coupling loss. One of the diluted ridge waveguides with a length of 4.8 mm was sputtered with a layer of SiO_2 film as an anti-reflection (AR) coating. The transmission characterization was then achieved with the output spectrum test setup mentioned in Section 2.2.4. Seen from the transmission results around 2 µm wavelengths through the 4.8 mm long diluted waveguide before (black) and after (red) AR coating as shown in Fig. 4.8, the significant reduction in reflection loss (suppression of the FP effect) is observed as a result of the AR coating. The excess loss is around 1.8 dB at 2 µm wavelength which

can be only assigned to the transmission loss along the waveguide in combination with the coupling loss between the waveguide facet and the input/collected lensed-ended fibre.
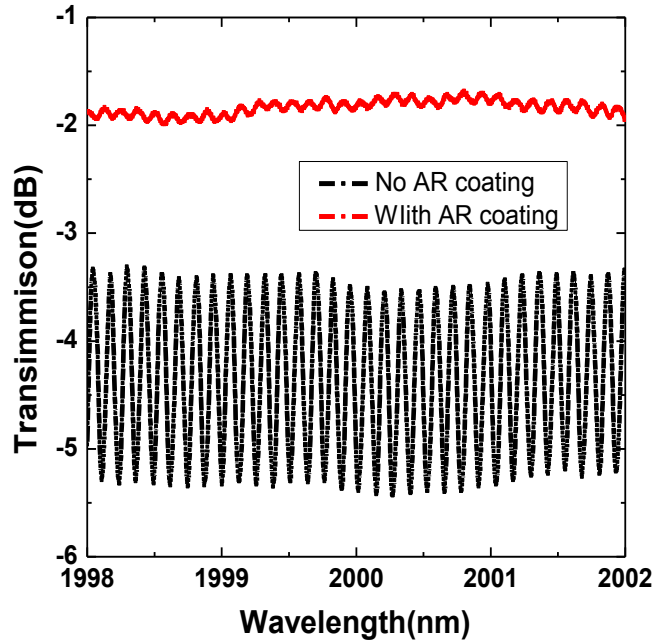
Figure 4.8: *Transmission through 4.8 mm long straight diluted waveguide with and without AR coating.*

Then, we can make the assumption that the maximum coupling loss would be smaller than 0.9 dB per facet if the mode tranmission loss is very small. The mode transmission loss can be estimated as < 3.6 dB/cm if the facet loss could be eliminated. Due to the small transmission loss for this type of waveguide, the same test on waveguides in shorter length such as 1 mm are not necessary. Also, the result from the cut-back method (deducing the attenuation parameter based on the single wavelength transmission data of the wacveguides in different lengths) is not reliable due to the same reason.

4.3 Multimode interference coupler based on the single-mode diluted waveguide around 2 micron wavelength

Due to the natural characteristics of the multimode waveguide, an input profile is able to be mirrored as a single or multiple images at certain positions which periodically appears along the propagation direction of the waveguide. The longitudinal position of the image has a strong connection with the parameter of L_π which is defined as the beat length of the two lowest-order modes. It could be explained as follows:

$$L_\pi \approx \frac{4 n_r W_e^2}{3 \lambda_0} \qquad (4.3.1)$$

Where, n_r is the (effective) refractive index of the ridge, λ_0 is the wavelength in the free space, and W_e is the effective width of the multimode waveguide which is dependent on the light polarization shown in Eq. 4.3.2 [9]:

$$W_e = W_m + \left(\frac{\lambda_0}{\pi}\right) \left(\frac{n_c}{n_r}\right)^{2\sigma} (n_r^2 - n_c^2)^{-\left(\frac{1}{2}\right)} \qquad (4.3.2)$$

Where, n_c is the refractive index of the cladding region, W_m is the physical width of the multimode waveguide, $\sigma=0$ when it is TM mode and $\sigma=1$ when it is TE mode. According to the general-interference mechanism which includes all the excited modes,
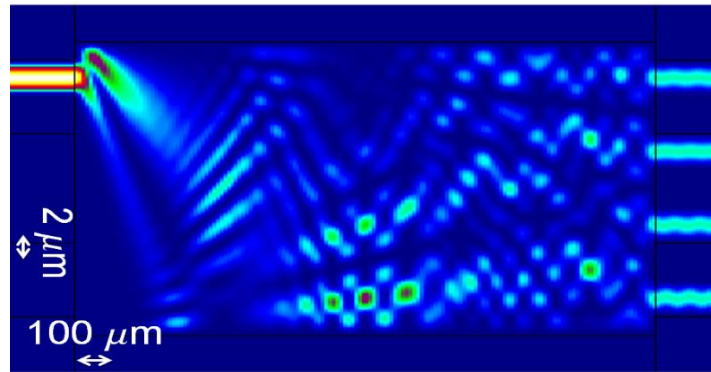
Figure 4.9: *Simulated mode transmission within the N×N MMI coupler (N=4).*

A N×N coupler could be achieved on the multimode interference (MMI) structure with the shortest length of $3 \times L_\pi/N$ corresponding with the longitude position of the first N-fold image, where N is the number of input and output waveguide [5]. The simulated propagation properties of the coupler with N=4 is demonstrated in Fig. 4.9. Therefore, the MMI scheme can be applied to achieve the waveguide-based coupler for the monolithic integration on one single chip by taking the advantage of the self-imaging property of the multimode waveguide while connecting a few single-mode waveguides at the beginning and the end of the multimode waveguide as the input and output ports.

Due to the high fibre coupling efficiency of the diluted waveguide, establishing the couplers based on this type of waveguide would help to further reduce the loss at the input/output of the chip and provide more facility and tolerance for coupling alignment during the following package process. While, most of the MMI couplers have been designed for applications at the wavelength of 1.55 µm, moving the working range of these device up to 2 µm wavelengths requires care on the refractive indices and device dimension variation at this new wavelength. In this section, we introduce the design and fabrication of the 1×2 and 1×4 MMI optical couplers at 2 µm wavelengths based on the single-mode diluted waveguide which has been achieved in the last section.

4.3.1 2 micron wavelength 3 dB coupler based on 1×2 MMI scheme

In a Photonics Integrated Circuit (PIC), a 3 dB coupler based on 1×2 MMI scheme works as a power splitter to separate the launched light into two evenly outputs. Here, we design this kind of device by using the symmetric interference mechanism with the first 2-fold image distance in the form of $\frac{3L_\pi}{8}$ (L_π is the beat length) resulting in the relatively short device length along the light transport direction in comparison with other interference schemes such as general inference [5]. By setting the width of the multimode waveguide as 14 micron and etching depth of 5.5 micron, a beat length (L_π) of 414 micron for TE and 426 micron for TM mode are obtained by use of both Eq. 4.3.1 and Eq. 4.3.2 with the ridge effective index of the above-mentioned 4 micron wide single-mode diluted waveguide and the refractive index of the cladding layer as

the same as the air (or free space). Therefore, a polarization-independent multimode waveguide length can be estimated around 158 µm deriving from the mean value of the calculated lengths corresponding to the first location of the 2-fold imaging point along the light transport direction within the waveguide for both polarization states.

(a)   (b)
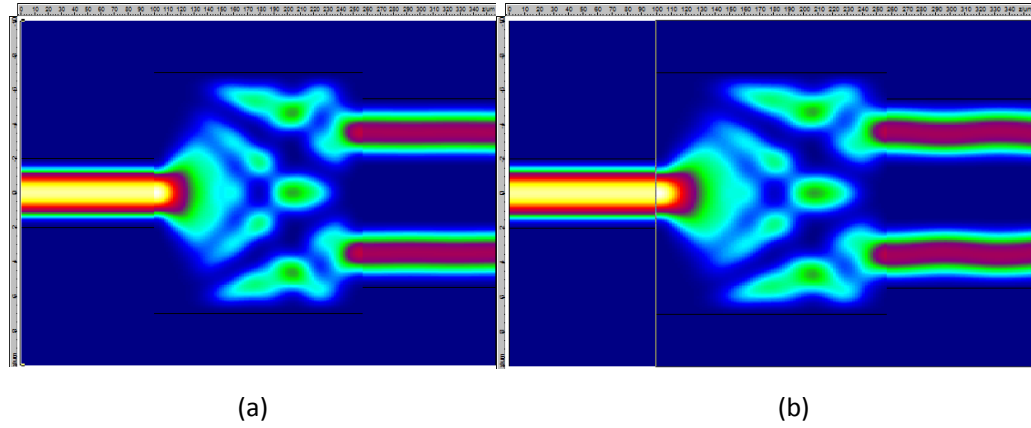
Figure 4.10: *Top view of the light transmission for the 3 dB coupler at 2 µm wavelength in TE (a) and TM (b) polarization.*

Using the 3-D simulation of the light launching into, propagating through, and coupling out from the device by use of FIMMPROP software (Fig. 4.10), an optimized MMI waveguide length of 157 µm is obtained demonstrating an output power imbalance of <0.002 dB, minimum loss of around 0.07 dB and polarization dependent loss as small as 0.0075 dB, which is summarised in Table 4.4.

Table 4.4: Simulation results for the 2 µm wavelength 1×2 MMI optical coupler based on the single mode diluted waveguide

Polarization	Output imbalance (dB)	Loss (dB)	Polarization dependent loss (dB)
TE	0.000475	0.0659	0.0075
TM	0.0013	0.0734	

The dimensions of the coupler involving the positon of the output waveguides are shown in Fig. 4.11. The waveguide width is 4 µm for both of the device input and output port while the etch depth is 5.5 µm which is not displayed in this planar view in Fig. 4.11. The interspacing between the two output waveguides is 3 µm and the

distance from the outer edge of one single-mode output waveguide to the edge of the multimode waveguide is 1.5 µm which is still over the general resolution limitation of 1 µm for the UV light expose process.
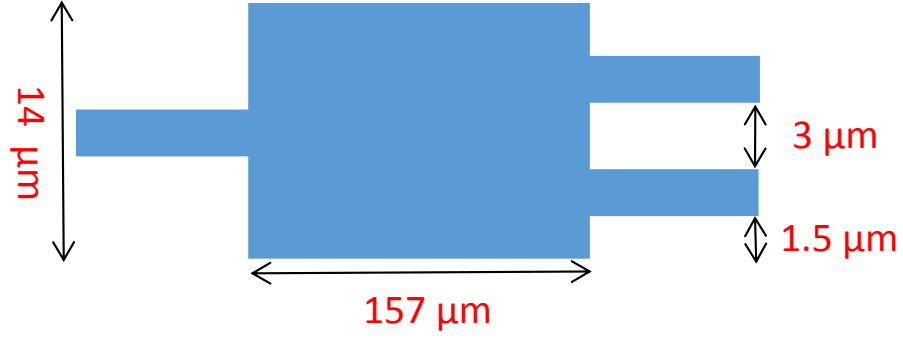
Figure 4.11: *Top view of the design scheme for the 2 micron wavelength 3dB coupler in 1×2 MMI coupler structure (single mode waveguide width: 3.5 µm).*

4.3.2 2 micron wavelength 1×4 optical coupler based on 4×4 MMI scheme

Based on the general interference MMI scheme (N=4), a design of 1×4 optical coupler with one input port (single mode waveguide) and four output ports (single mode waveguide) connecting with the wide multimode waveguide is proposed. Similar to the process of designing the 1×2 MMI optical coupler, the multimode waveguide width is fixed at 31 micron considering to beat more high-order modes for better imaging quality [5].
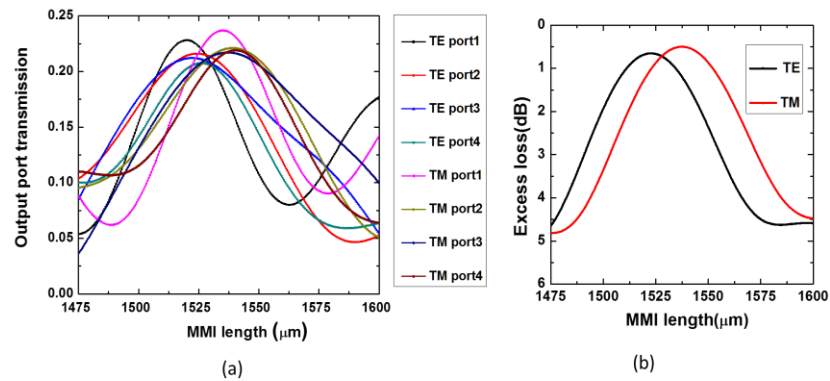
Figure 4.12: *Transmission of each port (a) and excess loss (b) for TE and TM polarization with the variation of the multimode waveguide length.*

Considering the effective index presented in Table 4.2, simulations to find the optimal length of the multimode waveguide for the coupler are carried out by use of FIMMPROP software. Fig. 4.12 (a) and (b) display the optical power transmission through each output port of the coupler as well as total excess loss of the device in different multimode waveguide lengths for both TE and TM polarisations. The optimal length is found to be approximately 1525 µm taking into account the power balance of the output waveguides and polarization insensitivity.

(a)   (b)
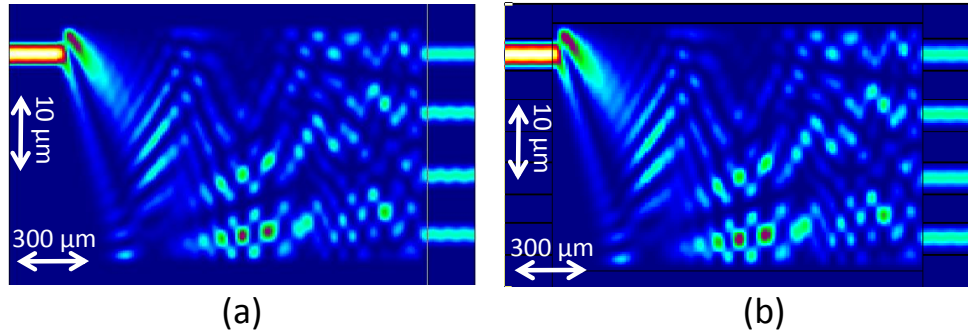
Figure 4. 13: *Top view of the light field distribution when it is transporting into, through and out of the 1×4 optical coupler at 2 µm wavelength in TE mode (a) and TM mode (b)*

Figure 4.13 illustrates the light power distribution along the transport path into, through and out of this 31 µm wide and 1525 µm long multimode waveguide for the 1×4 optical coupler with non-equally spaced output waveguides.

(a)   (b)
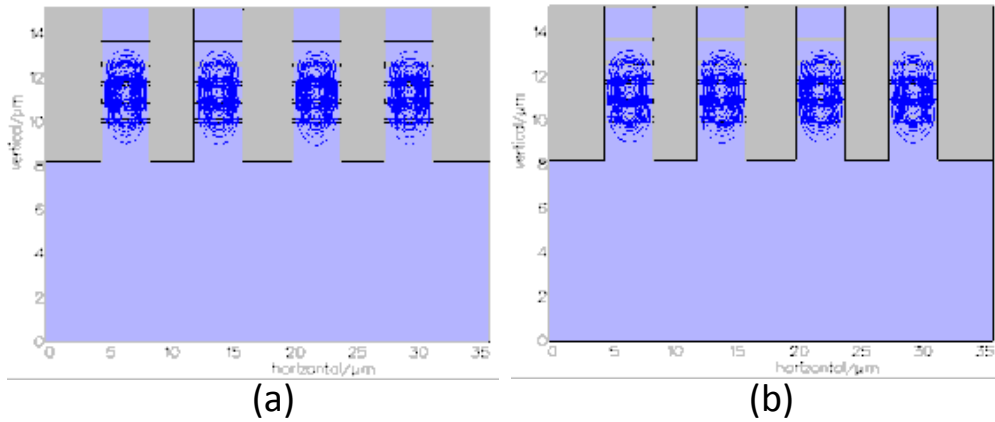
Figure 4.14: Transverse view of the balanced output field from the 1×4 optical coupler at 2 µm wavelength in TE mode (a) and TM mode (b)

Crucially, the power is balanced for both polarization states indicated by the mode field distribution from the transverse view of the output waveguides shown in Fig 4.14.

In Fig. 4.15, the complete design of the 1×4 coupler involving the positon of the output waveguides are demonstrated. It is obvious that the interspacing between the nearest waveguides is not the same value which indicates that the imaging is not fully symmetric to the middle of the multimode waveguide along the width direction.
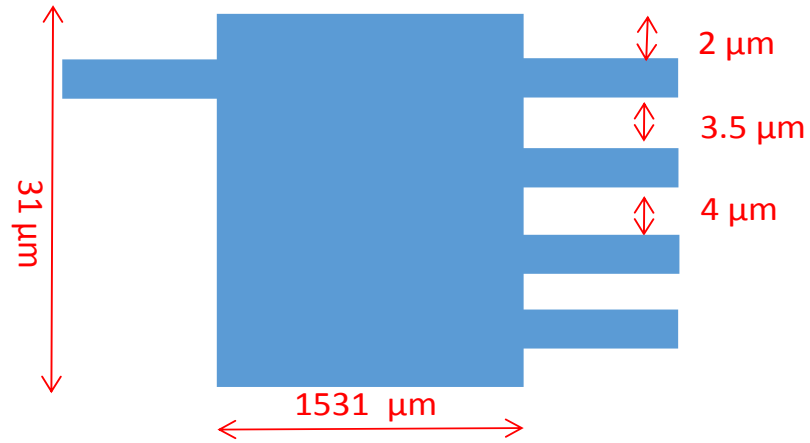
Figure 4.15: *Top view of the design scheme for the 1×4 optical coupler at 2 µm wavelength.*

This is due to the natural imaging property of the 4×4 MMI multimode waveguide (general-interference) that the optimum imaging locations (for the paired waveguides) at the output are symmetric with respect to the ¼ width point [9].

(a)   (b)
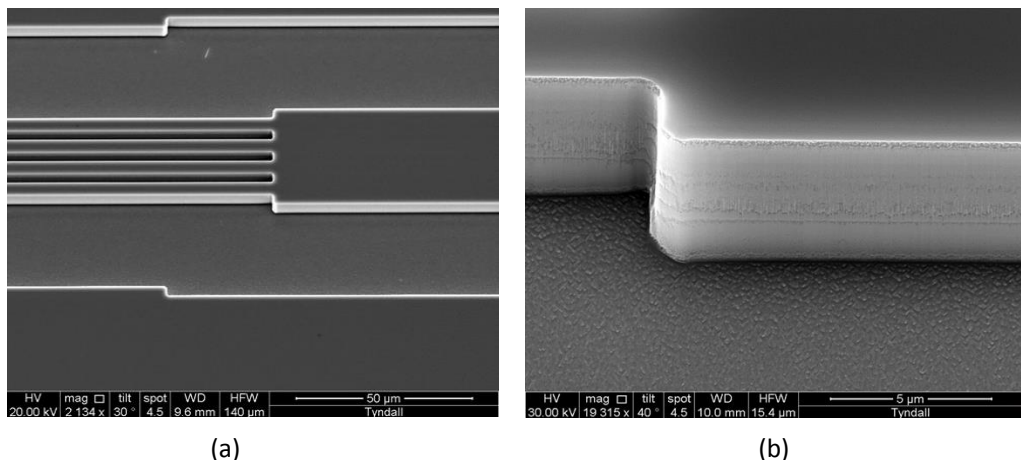
Figure 4.16: *SEM images for the output ports of the 1×4 MMI coupler (a) and etched side wall (b) around the multimode waveguide*

With the same fabrication process of the diluted waveguide, the 1×4 optical coupler was achieved with regular rectangular device geometry and smooth surface as demonstrated in the SEM images of Fig. 4.16 (a) and (b).

Having verified the quality of the diluted waveguide structure after the device fabrication, we examined the 1×4 optical coupler. In order to ensure that the optimal dimensions of the multimode waveguide were found, a number of MMI couplers were fabricated with various lengths and offsets from equal spacing (only for the output waveguides close to the edge).
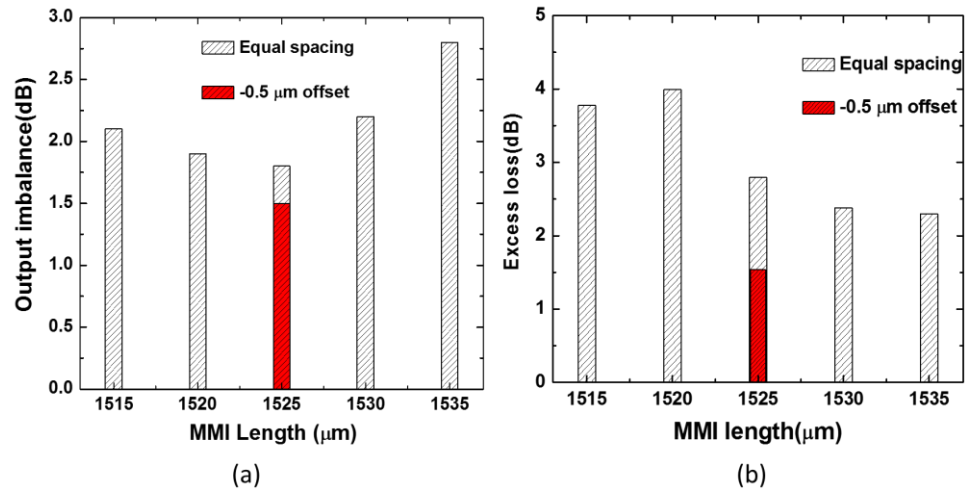
Figure 4.17: *Imbalance (a) and excess loss (b) for different device lengths and output waveguide offsets.*

The power imbalance and loss of these devices were then measured using the same setup to characterize the diluted waveguide but fixed at the wavelength of 2 micron, the results of which are presented in Figure 4.17. Note, these results are normalized to the loss of a straight diluted waveguides, effectively removing the coupling loss as well as waveguide transmissioin loss.. From these results, it can be seen that a minimum excess loss of 1.54 dB and power imbalance in the output ports of 1.5 dB can be obtained for the optimally-designed multimode waveguide dimension.

4.4 90° optical hybrid at 2 µm wavelengths

Based on the 1×4 optical coupler in the general interference scheme, an optical 90° optical hybrid can be obtained by exhibiting not only the balanced output power at the

output ports but also a quadrature phase relationships between the output waveguides when the signal and oscillator light are launched into any two asymmetric input waveguides. (Figure 4.18).
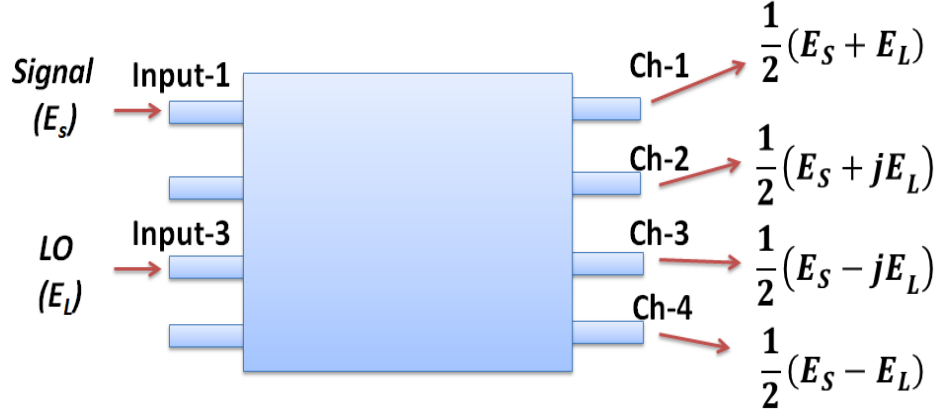
Figure 4.18: *Schematic of a 90° optical hybrid based on the 4×4 MMI (general interference) scheme*

The imaging property of 4×4 MMI in general interfenrence leads to the optimum locations for the input waveguides which are symmetric with respect to the ¼ width point on the multimode waveguide[9]. By setting a fixed width, the basic geometry of the multimode waveguide as well as the input/output port locations of the 90° optical hybrid in one particular wavelengths can be figured out by the above-mentioned theories.

4.4.1 Optical hybrid design and optimization

The width of the optical hybrid device is set to 32 μm in order to have the input and output channel with an equal center-to-center spacing of 8 μm considering that the adjacent images of the input mode should be symmetrically distributed around the ¼ width point at the end facet of the multimode waveguide (compared to the case of 31 μm width device). With the fixed width of the multimode waveguide (32 μm) and using one entrance waveguide as the input port (Fig. 4.19 (a)), the transmission property (at 2 μm wavelength) from each output port was simulated on the platform of FIMMRROP by scanning the multimode waveguide length around the estimation

value calculated in use of the formulars mentioned above (Section 4.3). The final result is demonstrated in Fig. 4.19 (b).Therefore, an optimum length of 1629 µm free from polarization dependence and minimizing the power imbalance between output ports can be obtained.
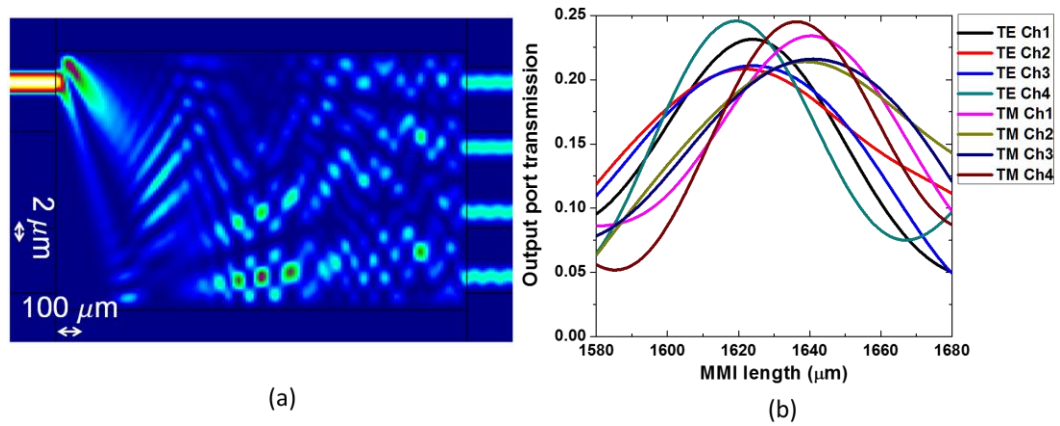
Figure 4.19: *Simulated results for the optical hybrid device working at 2 µm. (a) Planar view of the transmission. (b) Simulated output port power change due to variation in the multimode waveguide length for both TE and TM polarization.*

Table 4.5: CMRR and total excess loss deduced from the FIMMPROP simulation result for the 90° optical hybrid at 2 µm wavelength.

	Channel	TE	TM
CMRR (dB)	Ch1-Ch4 from Input1	39.1958	76.4739
	Ch2-Ch3 from Input1	46.6608	37.8091
	Ch1-Ch4 from Input3	46.6030	37.8156
	Ch2-Ch3 from Input3	39.4260	58.1625
Total loss (dB)	All ports to Input1	0.4186	0.4422
	All ports to Input3	0.4820	0.4617

Typically, the power imblance can be qualified in the form of Common Mode Rejection Ratio (CMRR) which is more sensitive to the imaging error of the multimode waveguide. From Table. 4.5, it can be seen that the CMRR for each output port of the device is greater than 37 dB at the optimized multi-mode waveguide length when the input light wavelength is 2 μm. Also, the total excess loss of the same device can be smaller than 0.5 dB deriving from the same simulation result shown in Fig.4.19 (b).

4.4.2 Test structure to evaluate the fabricated device.

To figure out the phase deviation, power imbalance and total excess loss for the designed 90° optical hybrid at 2 μm wavelengths, a test structure with the monolithic integration of MZI composed of a 1×2 MMI optical coupler and a delay line together with the hybrid component is proposed in this section.The phase deviation from the quadrature condition could be verified by takings the advantage of the wavelength-dependent phase shift of a MZI when connected with the 90° optical hybrid. As shown in Fig. 4.20, a 1×2 MMI optical coupler is used to equally separate the input power while the delay line introduces a phase shift dependent on the input wavelength.
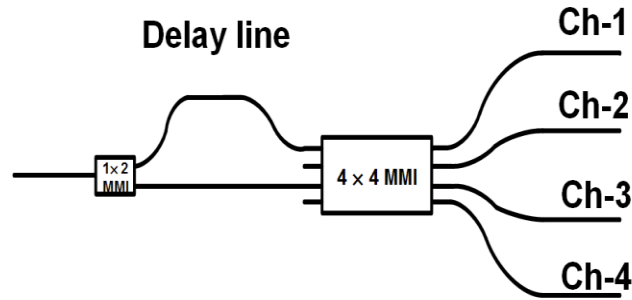
Figure 4.20: *Schematic of test structure to characterize 90° optical hybrid based on the 4×4 MMI multi-mode wavguide structure.*

When this section is connected with a 90° optical hybrid through two asymmetric input waveguides, the identified output port transmission function at the output channels of the device can be described by Eq. 4.4.1:

$$T_{chI} = \frac{1}{4}(A_{chI} + B_{chI}\cos(\theta_{chI} - \frac{2\pi n\Delta L}{\lambda}))$$ (4.4.1)

where, n is the effective index of waveguide, ΔL is the length difference between the arms ; θ is the nature phase of the channel including the background and distortion; A_{chI}, B_{chI} are referring to the power change (involving attenuation and scattering) after the device for the corresponding channel of chI. I is referring to the channel number (1,2,3,4).
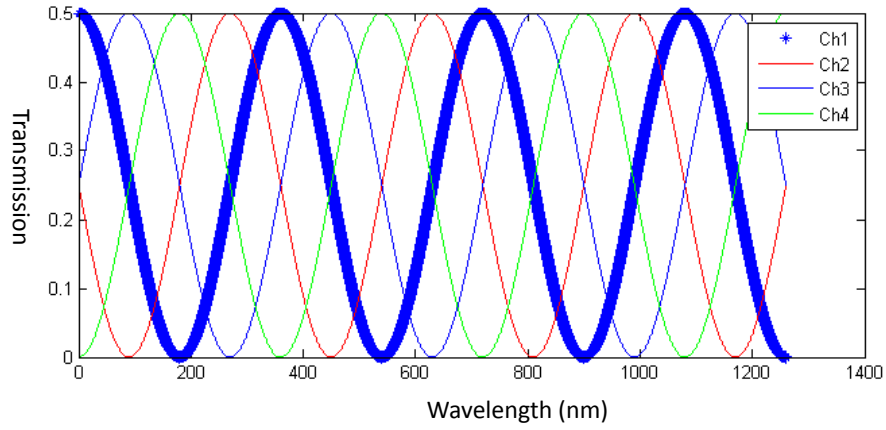
Figure 4.21: *Simulated transmission of different output ports when a broad band light is launched at the input of the test structure involving the 90° optical hybrid monolithically connected with the MZI.*

Theoretically, if there is no phase error and the power imbalance is fully eliminated, the output spectrum can be seen as Fig. 4.2.1. For the transmission spectrum of Channel 1 and Channel 4, the peak position of Channel 1 spectrum is corresponding to the valley of the Channel 4 which indicates the 180° phase relationship between each other. Furthermore, by sweeping the wavelength of the broad band input light, the phase shift from quadrature relation as well as power imbalance of the output port can be estimated by fitting the data to the Eq. 4.4.1.

During the mask design, an optimum dimension of 14 µm ×157 µm from the simulation results in Section 4.2.1 were used for the 1×2 MMI coupler. 32 µm wide 4×4 MMI devices with lengths varied by ± 60 µm around 1629 µm were investigated to compensate against simulation or fabrication errors.
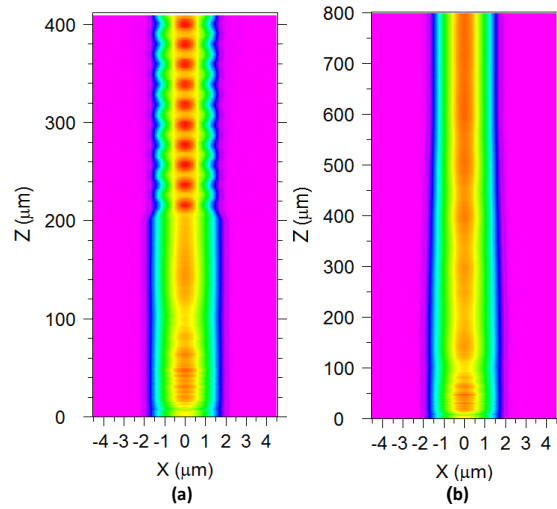
Figure 4.22: *Extra mode filtering effect for the taper with different lengths. (a) Waveguide width is linearly tapered from 4 μm to 3.5. μm over 10 μm length (b) Waveguide width is linearly tapered from 4 μm to 3.5. μm over 400 μm length.*

To avoid undesired high-order modes excited during the light coupling with the lens-ended fiber at the facet, all the input and output waveguides were adiabatically tapered to a width of 3.5 μm over a 400 μm length and then tapered back to 4 μm closed to the chip facet. The filter efficiency depends on the taper length which is shown in Fig. 4.22.
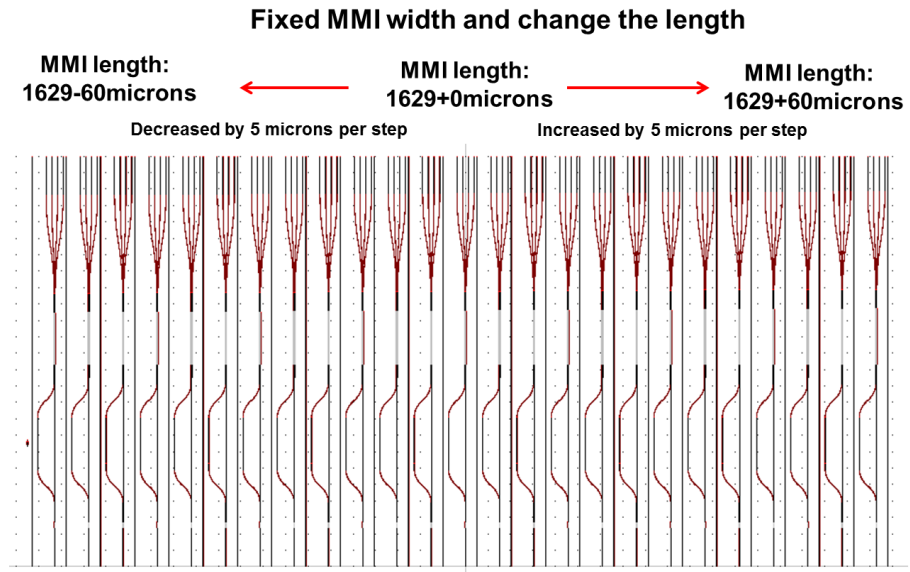
Figure 4.23: *The mask design for the monolithic test structures of 90° opitcal hybrid and MZI.*

When the taper length is only 10 μm, power oscillation due to the excitation of higher-order light modes is observed as shown in Fig. 4.22 (a). While, as displayed by Fig 4.22 (b), this can be highly suppressed until a single mode transport when the taper length is 400 μm long indicating sufficient mode-filtering. All of these simulated results are obtained by use of the Beam Propagation Method (BPM) module of Rsoft software.

In addition, taper structures are also applied in the launching and receiving ports of the multimode waveguide to provide more tolerance for the imaging quality. Finally, the interspacing of the input and output channels is enlarged to 127 μm to make it convenient for fitting the pitch of fiber array used in the packaging process. The view of the whole mask pattern can be seen from Fig. 4.23.

Deep etched (5.85 μm) ridge waveguide structures were obtained using the inductively coupled plasma ($Cl_2/CH_4/H_2$) etching. After cleaving the devices, a quarter-wave SiO_2 layer was deposited as an antireflection (AR) coating. Removing the AR coating by HF, the SEM image of a device is shown in Fig. 4.24.
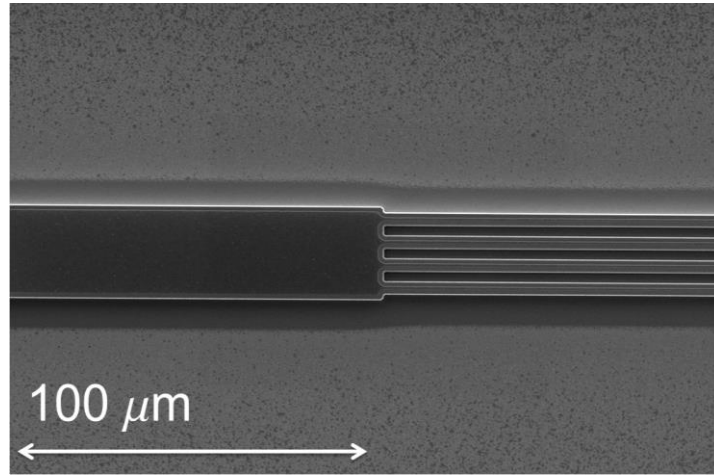
Figure 4.24: *SEM image of 90° optical hybrid at 2 μm after removing the AR coating by HF etching.*

Light from an un-polarized Amplified Spontaneous Emission (ASE) source based on a TDFA was coupled into the diluted waveguides by monitoring the output power until the maximum. The output light at each output port was then coupled into a lens-ended SMF and delivered to an Optical Spectrum Analyzer (OSA) to measure the resulting spectrum.

The transmission spectra covering 90 nm from the output ports of the 4×4 MMI normalized to the transmission from a straight waveguide are shown in Fig. 4.25 (a) for a device with dimensions of 32 µm × 1644 µm.

From this, we obtain a free spectral range (FSR) of 512 GHz (6.82 nm). Fig. 4.25 (b) shows the data over a span of 20 nm from which the quadrature nature is evident. By fitting the original transmission data with the Eq. 4.4.1 as that is displayed in Fig. 4.25 (c), the exact relative phases can be obtained and the power relation between each port could be estimated. The common mode rejection ratio (CMRR) which is equal to $-20 \times \log (|I_{Chm}-I_{Chn}|/(I_{Chm}+I_{Chn}))$, where m, n=1, 4 (In-phase) or 2, 3 (Quadrature) and I is the photocurrent proportional to the light power from the corresponding output channel [6].
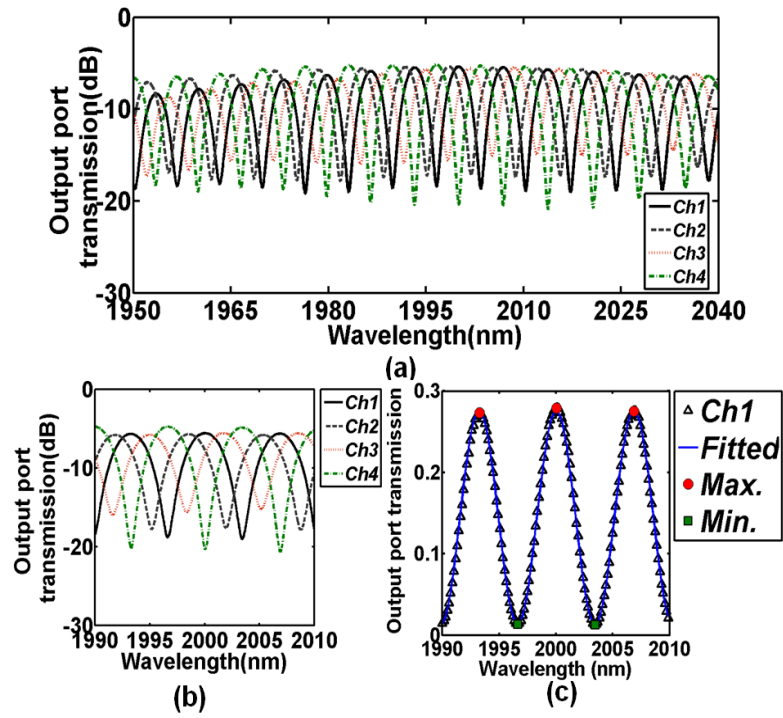
Figure 4.25: *Transmission spectra for different output ports of 90 optical hybrid (32 µm×1644 µm) around 2 µm with ASE input. (a) Span-90 nm (b) Span-20 nm (c) Fitted curve over 20 nm span.*

The minimum CMRR, the excess loss, and the relative phase are selected as the figures of merits to evaluate the devices as a function of MMI length (Fig. 4.26). The optimum 90° optical hybrid was found for a length of 1644 µm where a CMRR > 15.6 dB, an excess loss of 2.2 dB including the MZI structure and a phase deviation from quadrature condition of around ± 10° was obtained. This is close to the requirements for an optical coherent communication system application i.e. CMRR ≥ 20 dB, Excess loss < 3 dB, Phase deviation ≤ 5°.

The reasons for the unexpected power imbalance and phase error may be due to the un-polarized nature of the measurement or the high order modes distortion generated by over-etching the ridge [7].
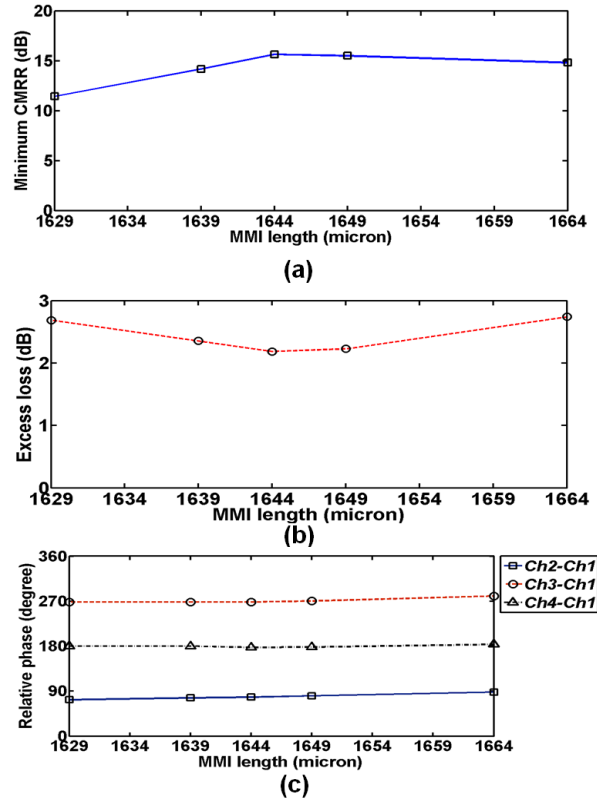
Figure 4.26: *Experimentally estimated performance for 90° optical hybrid in different MMI lengths. (a) Minimum CMRR. (b) Excess loss. (c) Relative phase.*

4.5 Conclusion

A low-loss diluted waveguide was designed, grown and fabricated, with transmission loss smaller than 3.6 dB/cm and coupling losses less than 0.9 dB per AR coated facet. Using the same epitaxial structure, a 1×4 (MMI) coupler for operation at 2 µm was developed with an excess loss of 1.54 dB and power imbalance as low as 1.5 dB. These advancements enable the development of a 90° optical hybrid based on 4×4 MMI working around 2 micron wavelength range. Using the monolithic integration of a MZI, a test structure allows the extraction of the phase deviation as well as the CMRR between the output channels of multimode waveguide. With the injection of broadband light and wavelength scanning at each output port of the device, we obtained a hybrid with approximately ± 10° phase shift variation from the quadrature condition, a CMRR better than 15.6 dB and total excess loss as low as 2.2 dB. These values are close to the requirement for the coherent detection in a 2 µm QPSK communication system. These hybrids will be combined with integrated balanced photodiodes to achieve a compact coherent receiver at 2 µm in the future.

4.6 References

[1] B. Mersali, F. Ghirardi, J. Brandon., *et al,* "Low-loss fiber-matched diluted multiple quantum well waveguide," *IEEE Proceedings-Optoelectronics*, vol.141, no.5, pp.296-298, 1994.

[2] A. Wieczorek, V Djara, F.H. Peters, *et al,* "Inductively coupled plasma deep etching of InP/InGaAsP in Cl2/CH4/H2 based chemistries with the electrode at 20 °C," *J. Vac. Sci. Technol*, vol.B, no.30, pp.051208, 2012.

[3] S. Taebi, M. Khorasaninejad, S. S. Saini, "Modified Fabry-Perot interferometric method for waveguide loss measurement," *Applied optics*, vol.47, no.35, pp.6625-6630, 2008.

[4] D.F. Clark, and M.S. Iqbal, "Simple extension to the Fabry-Perot technique for accurate measurement of losses in semiconductor waveguides," *Optics letters,*vol.15, no.22, pp.1291-1293, 1990.

[5] LB Soldano, and ECM Pennings, "Optical multi-mode interference devices based on self-imaging: principles and applications," *Journal of Lightwave Technology*, vol.13, no.4, pp. 615-627, 1995.

[6] N. Ye, M. Gleeson, H. Yang, *et al*. "Demonstration of 90 ° optical hybrid at 2 microns wavelength range based on 4×4 MMI using diluted waveguide," in *Optical Communication European Conference (ECOC)*, Cannes, France, 2014, pp. p.1-3.

[7] J. Fandiño, P. Muñoz, and J. Capmany, "Manufacturing Tolerance Analysis of an InP, 4×4 MMI-based 90° Optical Hybrid for Integrated Coherent Receivers," in *Optical Fiber Communication Conference and Exhibition (OFC)*, Anaheim, California, United States, 2013, pp.JW2A31.

[9] M. Bachmann, P.A. Besse, H. Melchior, "General self-imaging properties in N× N multimode interference couplers including phase relations," *Applied Optics*, vol.33, no.18, pp.3905-3911, 1994.

Chapter 5 Packaged high bandwidth photodetectors at 2-µm wavelengths

5.1 Introduction

Bare chips are not suitable to be used for long time experiments suffering from the unstable light coupling due to instability of the input fibre support stage and complex electrical interconnection between the device and measurement oscilloscope by the use of a high speed probe. Thus, packaging the device becomes necessary for the high-speed 2-µm photodiodes. For different types of photodiodes, a specific packaging scheme needs to be optimized in the respects regarding light coupling, electrical connection, inside supporting structure and outside cell design. In order to improve the light coupling efficiency of the ridge waveguide device, lensed-ended fibre is used at the input facet. The whole package module could take advantage of the previously designed high-speed laser module benefiting from the similar light coupling design as well as the electrical circuit access to the test system. To facilitate the coupling process during the package of the surface normal detector, an angled fibre can be used in order to bend the light path from horizontal to vertical for illuminating the top acceptance window of the surface normal photodiode set flatly on the planar ceramics surface. To obtain better electrical connection stability, improvement related to the module cell has been done by introducing a protrusion on the bottom of the top cover to tightly fix the output connector on to the ceramics and the following submount. Both the edge-coupling quantum well photodetector and the top-illuminated mesa type photodiode were packaged and then evaluated with large signal eye pattern test at 1.55 µm or 2 µm. All packaging works were supported by the Photonics Packaging Group in Tyndall. Before packaging, best samples with the lowest leakage currents were selected by the I-V test after cleaving the single devices from the wafer. Performanace characterizations about the stablity and SNR were carried out after packaging one of the samples to provide feed back for further modification on circuit design and light coupling within the module.

Here, we would like to explain the details about the design, assembly and improvement of the package module for both types of photodetectors. Large signal characterization results for those packaged module are displayed and analysed as the evaluation.

5.2 Package module of the ridge waveguide quantum well photodiode

Based on the 7-pin module cell for high-speed laser, the ridge waveguide quantum well detector can be packaged by applying a lensed-ended fiber to increase the input light coupling efficiency and an impedance-matching ceramics circuit combining a high speed connector to bridge the electrical connection between the device and the output access network. The module scheme is presented in Fig. 5.1 in 3-D coloured mode.
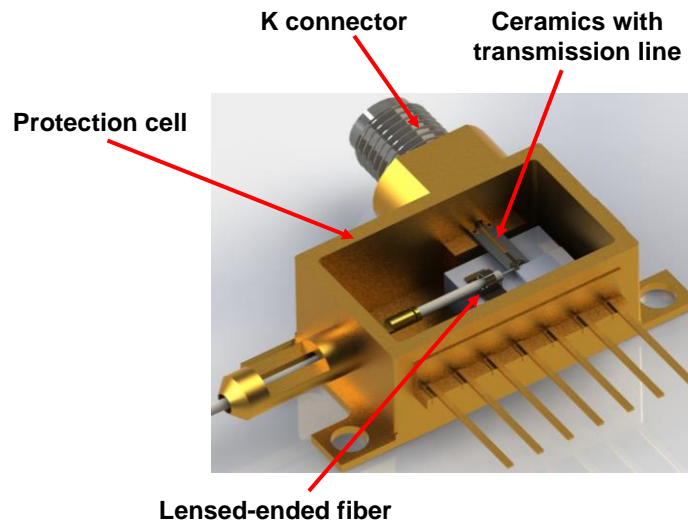
Figure 5.1: *3D simulation for the inside view of the packaged ridge waveguide quantum well photodetector at 2-µm wavelength.*

Due to the vertical confinement of multiple quantum well stack and the horizontal mode confinement of the ridge waveguide, the acceptance aperture is typically small compared to the mode size of the input single mode fibre. Therefore, the coupling efficiency is low and the fibre alignment/fixing tolerance is small due to the large

mode mismatch between the device and the input fibre. To accommodate such spot size mismatch, it is possible to adjust the absorption window of the photodiode or modify the mode dimension of the single mode fibre. Here, we put more effort on the latter as it is more convenient to be optimized by the technology used in the field of photonic device packaging.

A special fibre based on 2-µm single mode fibre (Type: Nufern_SM1950, Mode field diameter: 8.0 µm at 1.95 µm) was fabricated with a tapered head to compress the light mode spot coupled with the edge-coupling photodiode with the graph shown in the Fig. 5.2 [1].
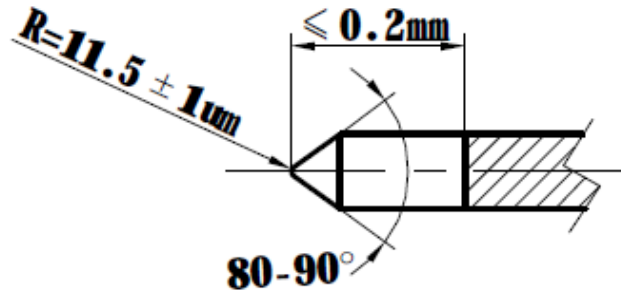
Figure 5.2: *Design of the lensed-ended fiber at 2 µm wavelengths* [1].

Within the package module, a clamp was used to fix the fiber onto the heat sink by laser soldering where the fibre was aligned at the optimum coupling point [2]. Manual adjusting is necessary considering the best coupling position shift due to the strain generation after laser soldering.

To couple the electrical signal of the detector to the high-speed connector of the package, a transmission line circuit based on an aluminium nitride substrate was set within the package module to build the connection in-between. In the end closest to the detector, a Coplanar Waveguide (CPW) structure was used to provide a flat plane for the wire bonding. Two 100 Ω resistors are positioned in parallel with each other to work as a 50 Ω load on the ceramic to suppress the reflections from the device due to the electrical property of the photodiode approaching to the open circuit under reverse bias (See section 5.5). In the transmission section, CPW is converted into microstrip line for facilitating the circuit fabrication omitting the vias and metal connection to link the top ground-plane with the bottom one. At the output end of the microstrip line, it is converted back again for the planar link with the pin of K connector on the

package. All of the transmission line are designed as an impedance of 50 Ω with details seen from the Fig. 5.1 and Fig. 5.3.
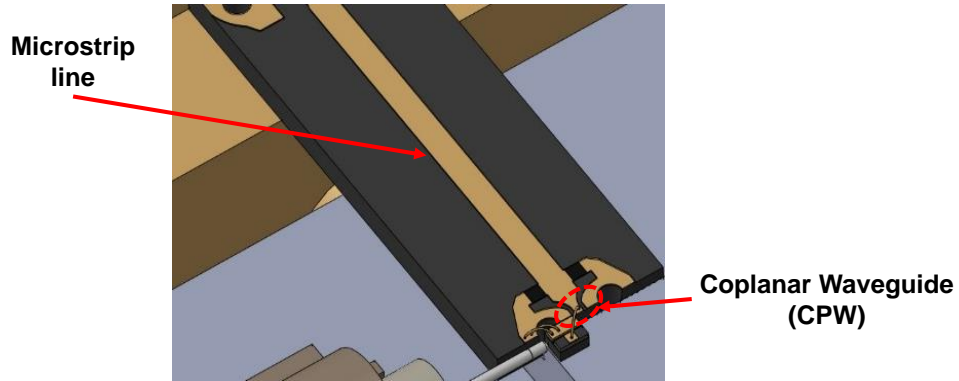
Figure 5.3: *Schematic of the circuit on the AlN ceramic.*

Direct wire bonding was firstly applied to connect the device with the CPW transmission line. Due to the softness of the BCB under the device bonding pad, pushing the soldering ball and then pulling the gold wire during the direct bonding process will destroy the contact of the device even the force is set at minimum.
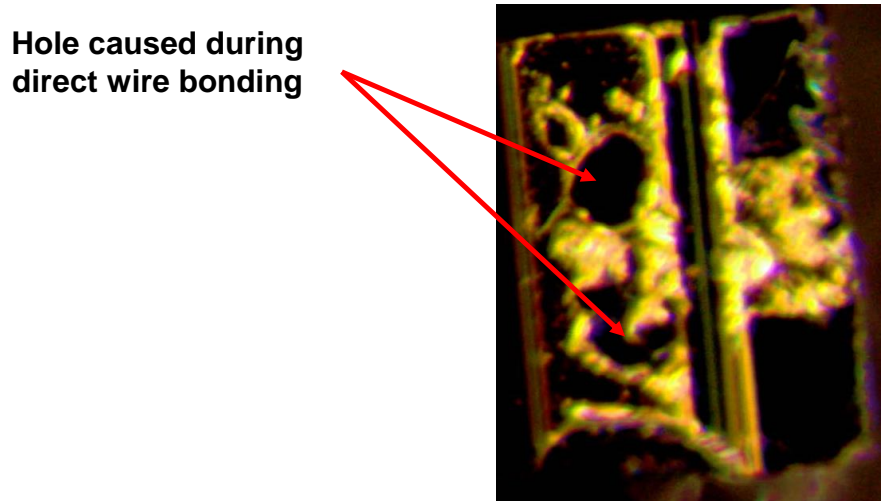
Figure 5.4: *Picture of the failed wire bonding process on the pad of the ridge waveguide photodetector monitored by the optical microscope.*

In Fig. 5.4, a damage to the bond pad can be observed indicating the failure of the direct wire bonding on the contact pad of the detector even with a thin dielectric protection layer. Increasing the thickness of the protective silicon dioxide layer and

using soldering method with silver epoxy or indium can help to solve this problem. For the former, as it is shown in Fig. 5.5, directly bonding between any contact pads works well when the thickness of the silicon dioxide was increased up to 500 nm.
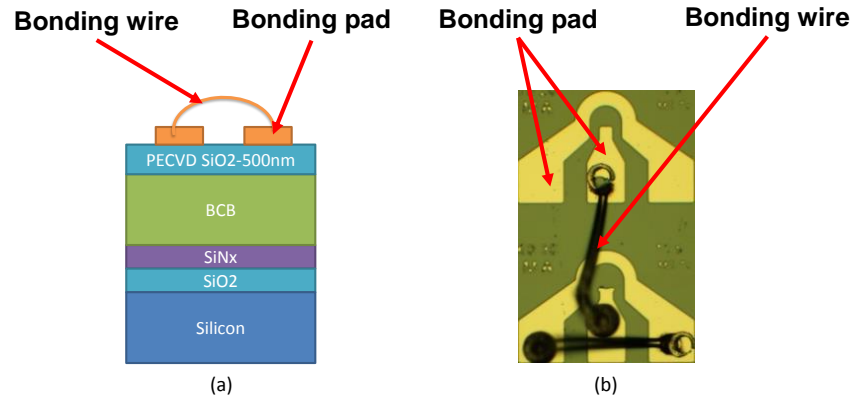
Figure 5.5: *Direct bonding test on the contact pad with 500 nm thick silicon oxide on top of the BCB.*

For the latter, both of the silver epoxy curing and wire soldering by indium reflow are able to fix the bonding wire on the top of the pad, which is shown in Fig. 5.6. We choose the former method due to that no more fabrication steps would be required. In addition, silver epoxy curing is efficient to be used due to the simple operation step though some technical experience is required during the disposition of the epoxy mixture to avoid the potential short curcuit .
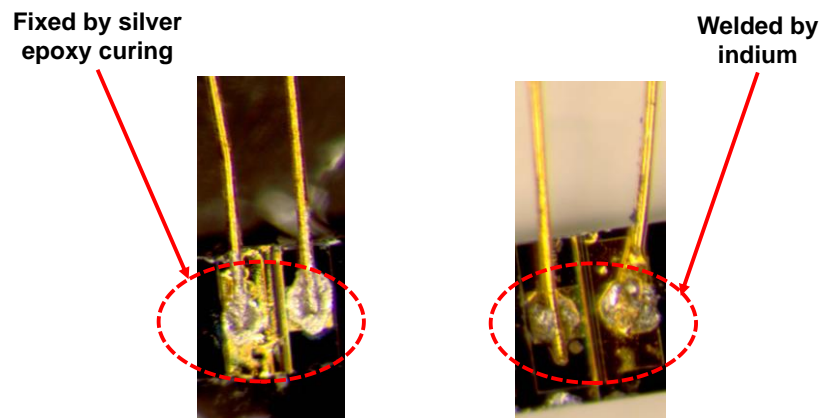
Figure 5.6: *Fix the bonding wires by silver epoxy curing and indium reflow.*

As the strong mechanical strength of the ceramic, direct wire bonding can be applied to fix the conductive wire on the CPW connection end.To electrically bridge the connection between the device and transmission line, a kind of hybrid bonding strategy is used. As it is shown in Fig. 5.7, direct bonding is used to attach one end of bonding wire on the CPW from the side of the transmission line. Then, the gold wire will be pulled up, cut off in a proper length and fixed on the contact pad of the ridge waveguide quantum well photodiode by the curing of silver epoxy.
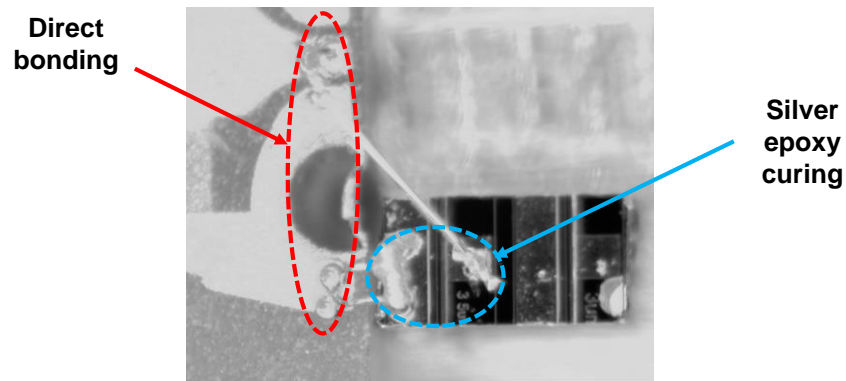
Figure 5.7: *Microscope image of the connection between the ridge waveguide quantum well photodetector and the transmission line.*

For assembling all parts of the module, the submout (heat sink) was first fixed on the bottom of the module cell by silver epoxy curing together with K connector. The same method was applied to the following cases of fixing the ceramics circuits on the submount, connecting the ceramic transmission line with the pin of the K connector on the package, and gluing the ground plane of the chip (backside) withthe submount. Then, the chip was connected with the transmission line by the above-mentioned hybrid bonding method. Finally, the 2 micron lens-ended fibre was laser-welded on the same submount after optimizing the coupling efficiency. All of the details of the assembled package module are displayed in Fig. 5.8.
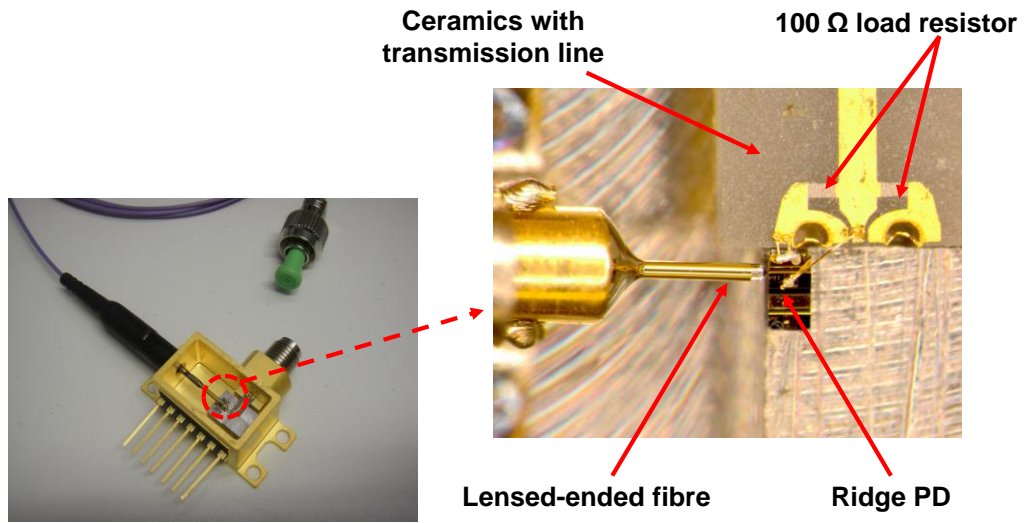
Figure 5.8: *Inside view of the final package for the high-speed ridge waveguide quantum well photodetector* [3].

5.3 Package module of the high-speed surface normal photodiode

Considering the horizontal operation function of the fibre alignment machine, a ~45° titled facet fibre was applied to bend the light path from horizontal direction to the vertical direction so as to illuminate it on the absorption aperture of the top-illuminated photodetector. This is demonstrated in Fig. 5.9 as below.
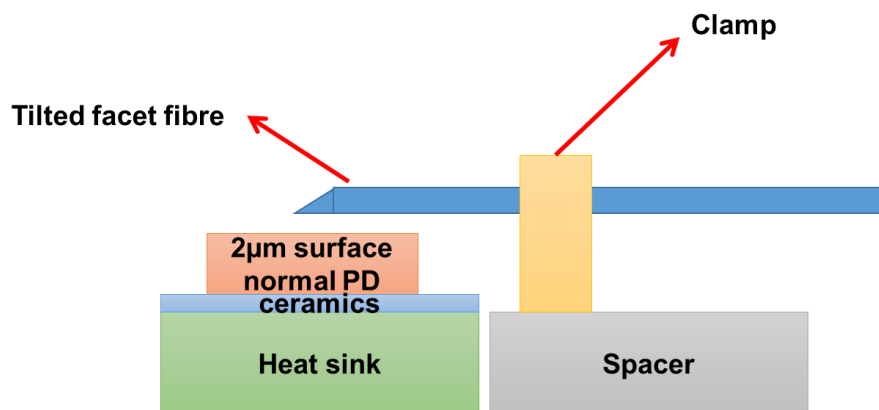
Figure 5.9: *Light coupling scheme for the packaged 2 µm high-speed surface normal photodiode in bulk material.*

In addition, with the consideration of using the existing photodiode RF characterization submount (see section 3.3.4) to save the total production time, the related space arrangement within the package module should be adjusted. To hold this fibre at a proper vertical position, a clamp was welded to fix the fibre, then both (fiber with clamp) were laser-soldered on top of a spacer which is used to provide another stage beside the RF characterization submount to compensate the height difference between the absorption window and soldered fibre. Such arrangement can be seen from Fig. 5.10. and Fig. 5.11.
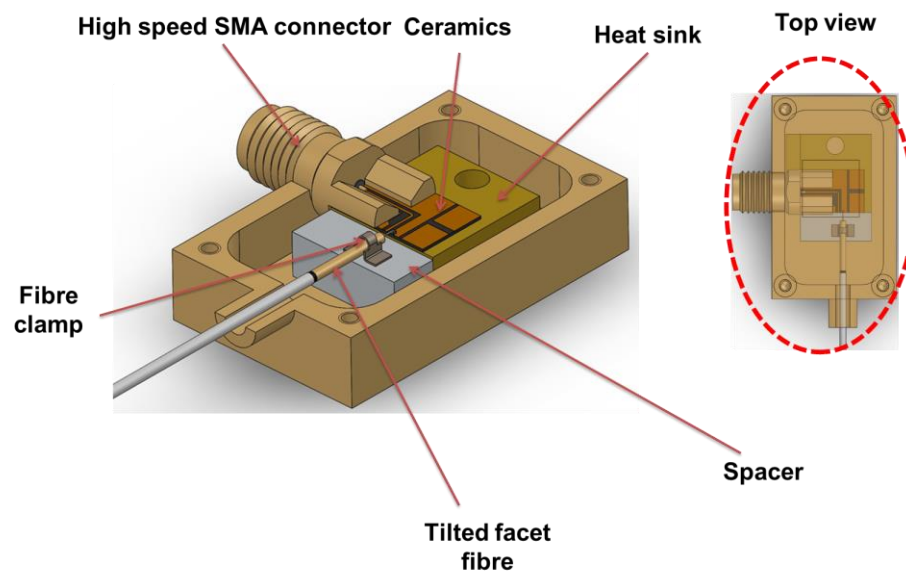
Figure 5.10: *3D schematic of the inside structure for the high-speed surface-normal photodiode package module.*

The assembling process started from fixing the photodetector test module as well as the spacer on the bottom of the protection cell by the curing of silver epoxy. After hybrid bonding the chip on the transmission line of the ceramic, optimized fibre alignment was done for at the best coupling efficiency through the monitoring of the photocurrent under zero bias. Then, the fibre was laser-welded on the spacer and finalized with manual adjustment similar to the process of packaging for the high speed ridge waveguide laser. The whole views of the module inside is displayed in Fig. 5.11 after the completion of the assembling.

As it is mentioned before, the stability of the connection between the high-speed SMA connector suffers from the low mechanical strength of silver epoxy in the case of the twisting operation to fasten the cable with the connector. As it can be seen from Fig. 5.12, a modification of cell design introduced a protrusion square on the inner surface of the top cell cover to further tighten the connector-ceramic connection by adding extra pressure on the connector arm when it is closed.
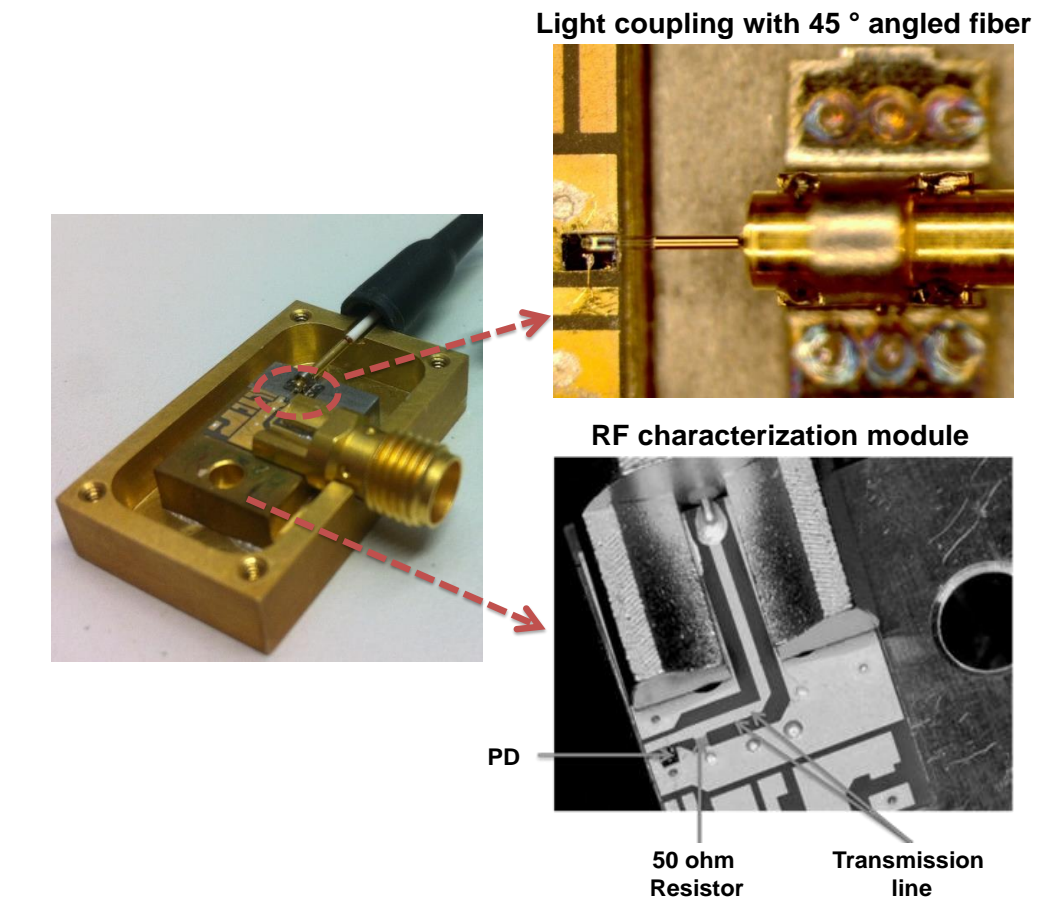
Figure 5.11: *Graph of the inside for the 2 µm high-speed surface-normal photodiode packaged module* [4]

Considering that a slight touching force between the closed top cell and the fibre clamp may shift the optimum coupling point, four screws were adjusted to tune the best position back to maintain the maximum coupling efficiency in the final stage of covering the top cell (Fig. 5.12 (c)).
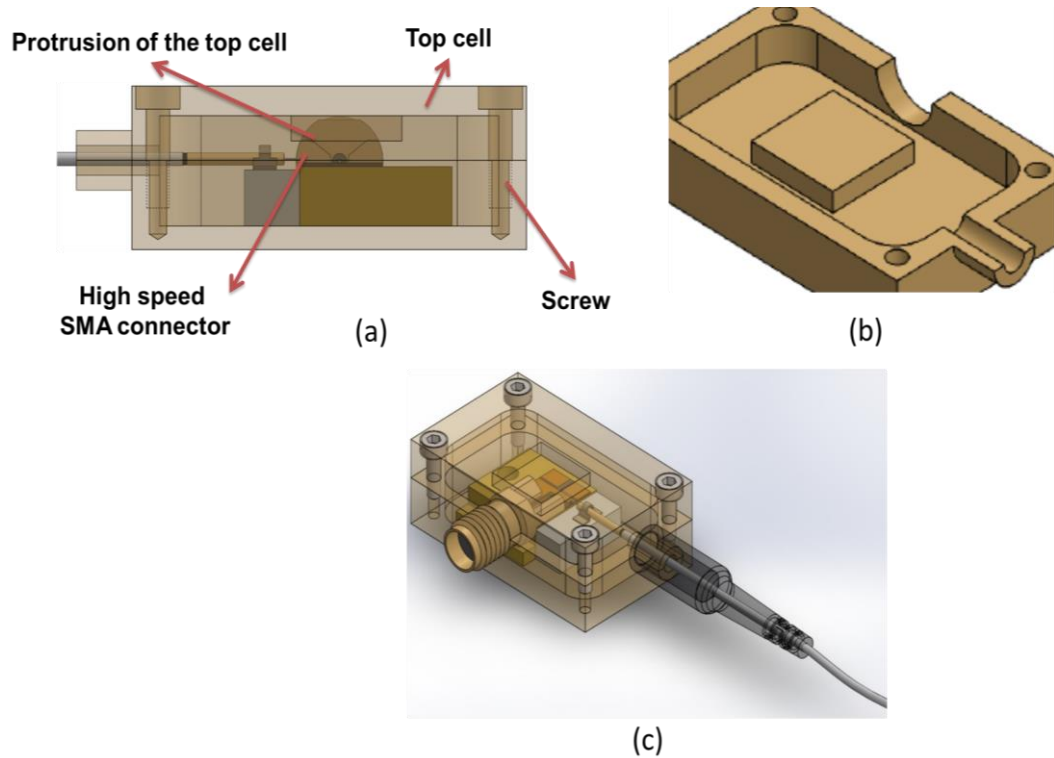
Figure 5.12: *3D view of the module cell design modification for tightening the connector-ceramics connection of the 2 µm high-speed surface normal photodiode in bulk material. (a) View of the tightening function of the top cell protrusion in the case of transparent cell; (b) View for the inside of the top cell; (c) View of the whole package module in the case of transparent cell.*

5.4 Large signal characterization results and analysis for the packaged 2 µm high-speed photodiode.

In order to prove the capability to work in an optical communication system, the eye diagram for the photodiode needs to be tested by use of high-speed optical signal loaded on the input light and visualized by the electrical setups involving electrical amplifier and oscilloscope after the recovering of the photodiode. Here we present the large signal characterization results for the ridge waveguide quantum well photodiode at 1.55 µm and surface normal type bulk material photodetector at 2 µm.

5.4.1 Characterization of the packaged 2 µm ridge photodiode

As it is shown in Fig. 5.13, the internal clock signal generated by the pulse pattern generator (PPG) is loaded by an electrical driver and converted into the optical On-Off-Key (OOK) using an 1.55 µm $LiNO_3$ intensity modulator at the transmission side. The output signal from the photodiode is amplified and then presented as an eye pattern on the oscilloscope. Between the photodetector and electrical amplifier, a Bias-T is used to separate the DC bias and RF signal so the voltage could be biased on the device while the high-speed signal is delivered in to the amplifier with no extra crosstalk to the DC channel. The setup was calibrated by a 40 GHz commercial 1550 nm photodiodes to prove the working ablity for our characterization.
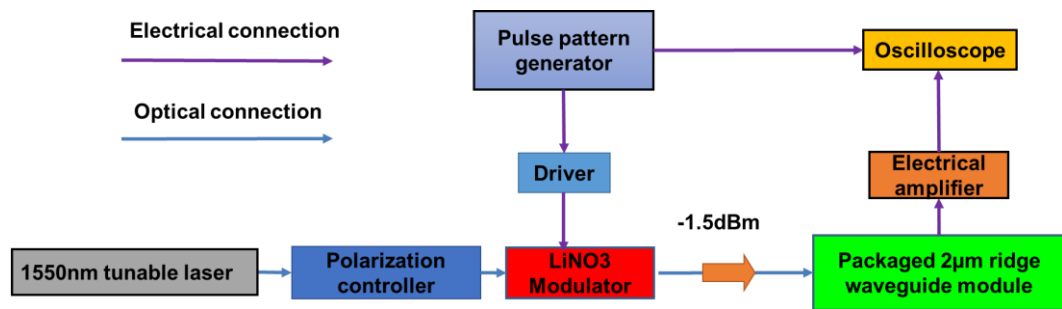
Figure 5.13: *Test system for the 2-µm ridge waveguide quantum well photodiode module in 1550 nm*

Manual optimization of the polarization at the input port of the modulator and fibre bending before the tested photodiode have been done to achieve the best signal quality and absorption efficiency.
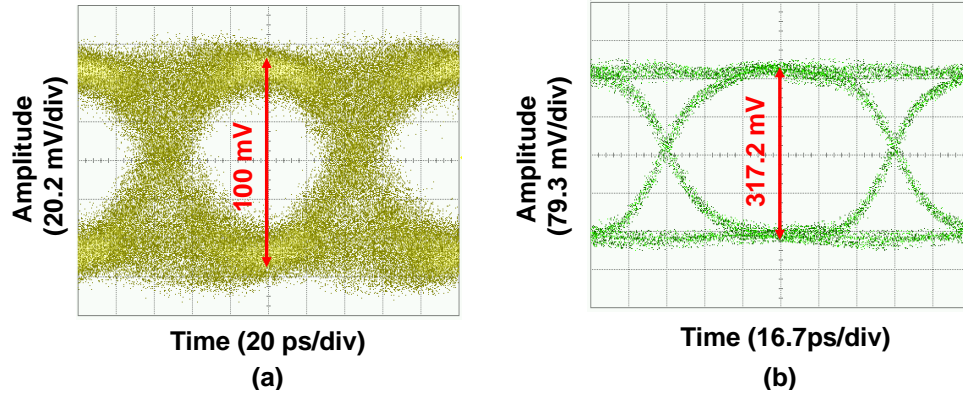
Figure 5.14: *1.55 µm eye diagram test results at the modulation speed of 10 Gbit/s with -1.5 dBm input power for the ridge waveguide quantum well photodetector module biased at -5 V*. (a) *Output from the photo-detector module (b) Output from the amplifier at the driving side of the modulator(original signal).*

It can be seen from Fig. 5.14 that the output signal coming from our photodiode (Fig. 5.14 (a)) was so much smaller than the original un-amplified one (Fig. 5.14 (b)) from the PPG that the electrical signal amplitude is around 100 mV (V_{pp}) which is too low to show a result with an acceptable SNR. That resulted from the low photoresponsivity of the photodiode, which was reduced from 0.3A/W to 0.14 A/W at 0 V bias due to the shift of the best coupling position resulting from the cooling of the clamp after the laser-soldering. Low light-coupling tolerance of this type of the detector can be seen from the dropping of photoresponsivity after the completion of the whole packaging process. Correspondingly, output electrical signal amplitude from our packaged photodiode was much smaller than the expected. While, the heating of the resistor due to the direct-biased voltage put on itself will increase the thermal noise level contributing to the degradation of the eye pattern quality further (see Section 5.5).

5.4.2 Characterization of the packaged surface normal type photodiode

Due to the high photoresponse and large RF bandwidth, the 50-µm diameter device from Design-2 material with BCB was packaged in a module with a ~45° angled fiber welded in the packaged module to illuminate the light on the absorption window of the device (Fig. 5.10, 5.11, 5.12). Then, the system as Fig. 5.15 was built to characterize the large signal performance of this package module at 2 µm wavelengths.
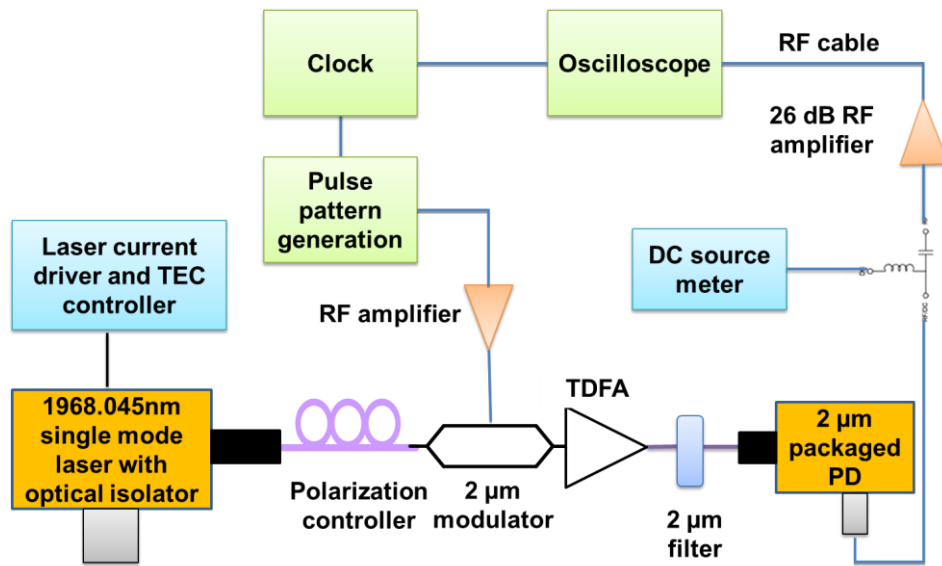
Figure 5.15: *Test setup structure for the packaged 2-µm high-speed photodiode in bulk material (Design-2, with BCB).*

At the transmission side, a laser showing a peak wavelength of 1968.045 nm is used to provide the light source. Similar to the 1.55 µm setup, optical signal is generated by a 2-µm Mach–Zehnder Modulator (MZM) driven by the amplified RF signal from the PPG. In the receiving end, we use the TDFA to achieve the light signal amplification at 2-µm wavelengths following with a 2-µm filter to suppress the additional broad band self-emitting noise. An independent electrical amplifier was used after the connector to amplify the recovered signal instead of an inner TIA inside the package module.

With a reverse bias of 7 V, input power of -0.05 dBm, we are able to see from Fig. 5.16 that a clearly-opened eye could still be obtained even at modulation speeds up to 15.7 Gbit/s. This proves the ability for the packaged module to work in a real 2 µm optical communication system which typically focuses on the SNR performance.

From Fig. 5.17 , we find the effective photoresponsivity (at 2 µm wavelength) of the packaged devices is reduced from 0.93 A/W (coupled by the 2 µm lens-ended fibre) to 0.52 A/W at -10V due to the lack of antireflection coating on the tilted facet which is designed for the applications in 1.55 µm wavelengths, fiber connector loss and alignment mismatch between the device and angled fiber during the packaging process.
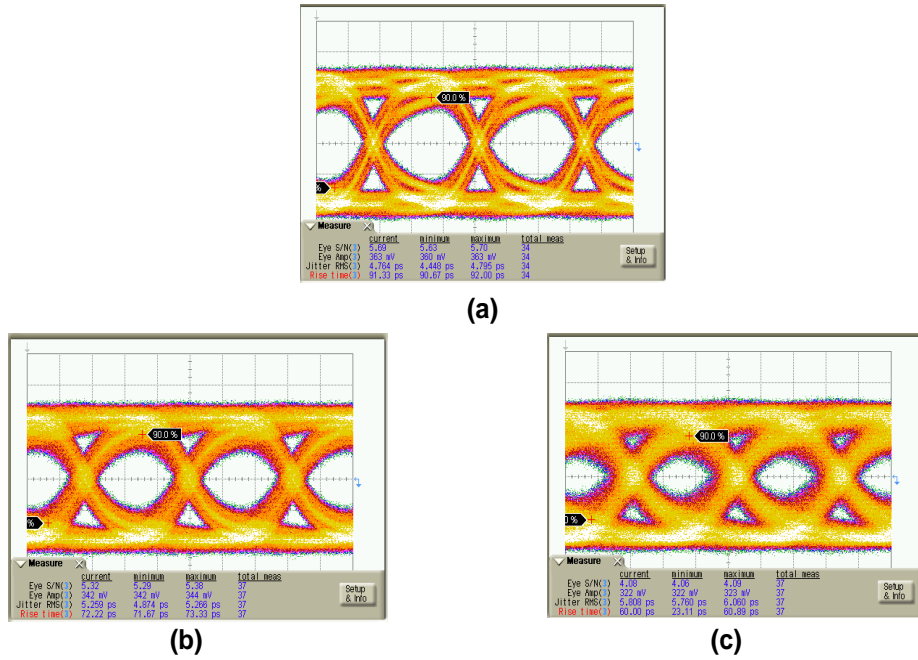
Figure 5.16: *Eye pattern characterization results for the 2 micron high speed surface normal photodiode module at the modulation speed of 10 Gbit/s (a)，12.5 Gbit/s (b) and 15.7 Gbit/s (c) (Bias voltage: -7 V, Input power: -0.05 dBm).*

This would highly affect the SNR of the output signal even in the case of higher input power by increasing the gain of the TDFA due to that the ASE noise would arise to degrade the Optical Signal to Noise Ratio (OSNR). As it is shown in Fig. 5.18, an open eye with an effective amplitude of 363 mV (V_{PP}) was obtained at a bias of -7 V by increasing the input light power to -0.05 dBm at 10 Gbit/s (Fig. 5.18 (a)), which is comparable with the results from the device in the same pattern and structure coupled by flat facet fiber with the input power of -3.07 dBm based at -10 V at the same speed (Fig. 5.18 (b)). While, it could also be indicated from Fig. 5.18 that the SNR of the packaged photodiode is degraded though the total amplitude has reached around 400 mV (V_{PP}) with the additional noise when the input power is increased by ~3 dB. In addition, applying a larger bias voltage may increase the photoresponse of the device corresponding to a larger eye amplitude while increasing noise due to the thermal heating of the parallel resistor on the ceramics circuit is proportional to the biased voltage (See section 5.5).
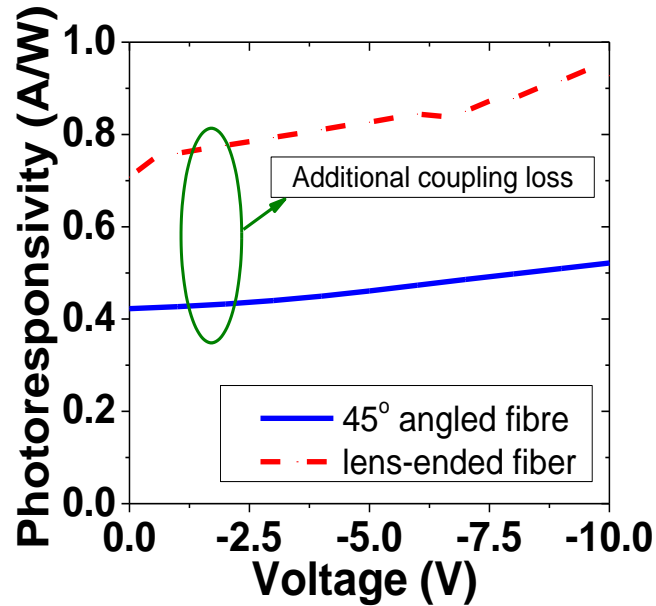
Figure 5.17: *Photoresponsivity at 2 µm wavelength for the packaged high speed surface normal photodiode based on Design-2 material with BCB.*

Due to the compromised OSNR from the excess optical loss, limited frequency response of the package circuit, impedance mismatch between the packaged PD and the RF amplifier, the eye diagram of the packaged surface normal detector is degraded, clearly showing varied rise and fall transitions as Fig. 5.18 (a). To improve the packaged device performance, optimizations would be focused on improving the coupling efficiency by the deposition of the aluminum film on the angled facet, suppressing the impedance mismatch in the connection of the chip to the transmission line and ceramic circuits to the following RF cable, as well as introducing a TIA to the packaged module [4].
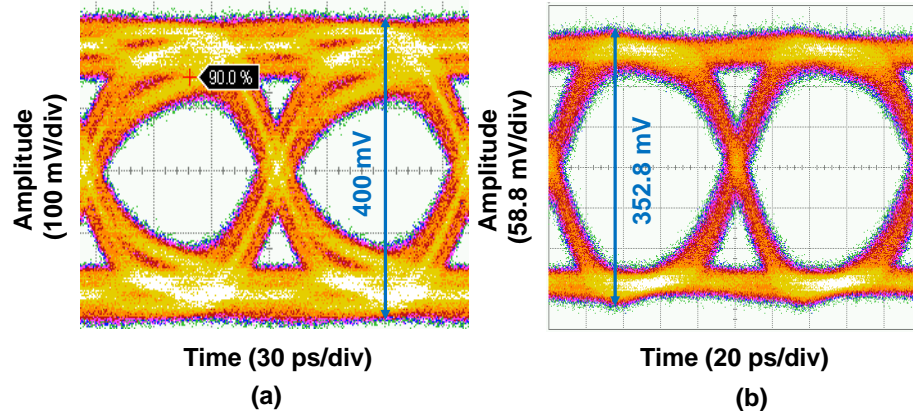
Figure 5.18: *Eye pattern for the 50 μm surface normal photodiode in Design_2 material coupled with an angled fiber (designed for 1.55 μm applications) without anti-reflection coating in the package module at the input power of -0.05 dBm (-7 V) (a) and with a flat facet fiber at the input power of -3.07 dBm (-10 V) (b). The fiber used here was a single mode fibre for the 1.55 μm wavelengths.*

5.4.3 Comparison between different packaged photodetector modules.

With the same modulation rate of 10 Gbit/s, the optimum eye patterns of the packaged modules for the ridge waveguide quantum well photodiode and surface normal type detector in bulk material have been obtained as those demonstrated in Fig. 5.19.

Though the data for the ridge PD was obtained at 1550 nm, it is still able to indicate the signal recovery quality of the photodetector such as SNR because of the ridge waveguide geometry is able to absorb all the light shorter than the photoresponse spectral edge of the intrinsic layer. Obviously, the eye amplitude of the ridge waveguide type (Fig. 5.19 (a)) is around 100 mV (Vpp) which is much smaller than the output from the surface-normal PD (Fig. 5.19 (b)) which is around 400 mV (Vpp) even though the former input light power is 1.45 dB larger than the latter and using the electrical amplifer with a gain of ~30 dB (26 dB for the surface normal type detector). Therefore, due to the high SNR quality benefiting from the highly efficient absorption aperture, the surface-illuminated type photodiode in bulk material is more appropriate for the applications in the real 2-µm optical communication system, which needs high signal quality at the receiving end.
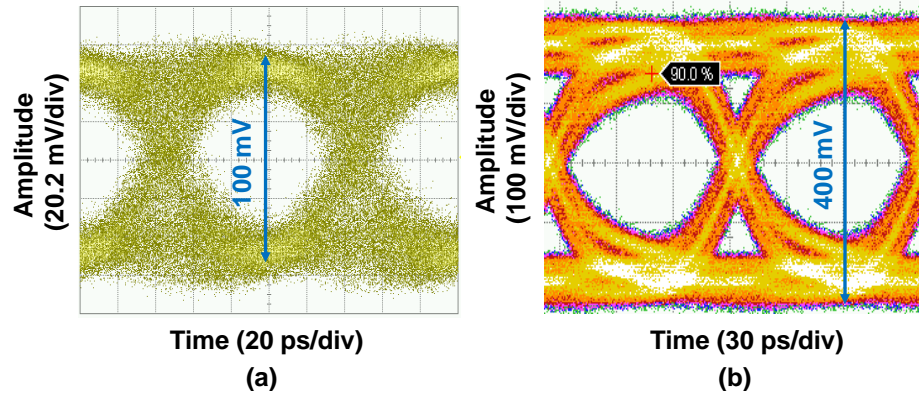
Figure 5.19: *10 Gbit/s eye pattern test results of the packaged module for the ridge waveguide quantum well photodiode based in -5 V with the input power of -1.5 dBm at 1550 nm wavelength (a) and surface-normal bulk material detector based in -7 V with the input power of -0.05 dBm at 1968.045 nm (b).*

5.5 Optimization on the circuit design to improve the SNR

For the package modules of both devices mentioned-above, more attention should be paid on the problem of the thermal noise from the heating of the resistor in parallel with the photodiode at high reverse bias voltage on the ceramics circuits. It would further degrade the signal quality especially in the case of small input light power.

This could be solved by considering the isolation of DC bias and RF output during the internal circuit design within the modulator.
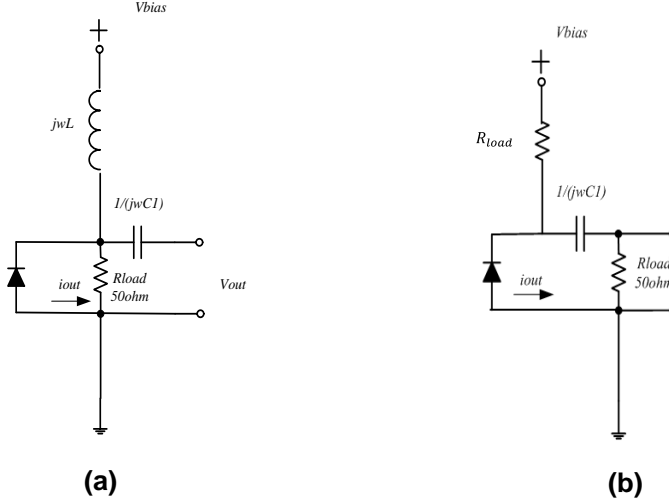
Figure 5.20: *Equivalent circuit for the design of parallel load resistor in front of external Bias-T for the current package module (a) and after internal Bias-T for an optimized package module* (b).

When it is connected with the external Bias-T in the access network of the electrical test system, the equivalent circuit of the high-speed package modules for both types of photodiodes could be simplified as it is shown in Fig. 5.20 (a). It can be deduced that the DC-bias voltage of the detector is also put on the impedance matching resistor due to the parallel connection scheme, this results in a thermal noise increasing due to the heating of the resistor. Though this heat could be released by using a high thermal conductivity metal sub-mount under the device, it is still not solved probably in principle. Here, we propose a simple adjustment of the circuit as which is shown in Fig. 5.20 (b) to isolate the DC bias on the resistor from the RF output of the device. Due to DC isolation character of the capacitance in the circuit, the resistor is only in the high-speed signal circuit in parallel with the photodetector. In the DC bias access port, a resistor is used to isolate the RF signal considering the detector as an alternatively variated current source. To achieve this circuit scheme, an internal bias system would be introduced into the circuit design instead of using the external Bias-T device, which means both of the matching resistor and the capacitance should be set within the ceramic circuit.

5.6 Conclusions

In this chapter, we introduced the package design as well as the assembly process for both of the ridge waveguide quantum well and surface normal bulk material photodiodes at 2-µm wavelengths. Characterization systems have been built to evaluate the large signal performance of the former in the wavelength of 1.55 µm at 10 Gbit/s and the latter at 2 µm with different bit rates up to 15.7 Gbit/s. Comparison between the 10 Gbit/s eye pattern results of the two packaged devices indicates the high signal recovery efficiency of the surface-illuminated type detector which is more appropriate for the system level applications. Analysis is undertaken on the reasons for the degradation of the eye diagram after packaging process. To suppress the thermal noise for further improving the SNR, it is suggested to apply the internal Bias-T to build the isolation referring to the DC voltage biased on the photodiode instead of using the external Bias-T in between the packaged module and electrical access network of the electrical test system, which may require more work on the ceramic circuits design.

5.7 References

[1] http://cxfiber.com/en/

[2] J. H. Song, P. O'Brien, F.H. Peters *et al*, "Optimal laser welding assembly sequences for butterfly laser module packages," *Optics Express*, vol.17, no.19, pp.16406-16414, Aug., 2009.

[3] H. Yang, N. Ye, R. Phelan, *et al*, "Butterfly packaged high-speed and low leakage InGaAs quantum well photodiode for 2000nm wavelength systems," *Electronics Letters*, vol.49, no.4, pp.281-282, Feb. 14, 2013.

[4] N. Ye, H. Yang, M. Gleeson *et al*, "InGaAs Surface Normal Photodiode for 2 µm Optical Communication Systems," *Photonics Technology Letters IEEE*, vol.27, no.14, pp.1469-1472, Jul.15, 2015.

Chapter 6 Summary and further work

6.1 Summary of this thesis work

At wavelengths of 2 µm, we have achieved both ridge waveguide/surface-normal type high speed photodiodes. An 90° optical hybrid have also been demonstrated for coherent detection. Electrical, optical and subsystem-level tests have been fully carried out to prove their ability to work in a real optical communication system. Here, we would like to summarize all the above-mentioned work and propose some suggestions regarding the further improvement on those devices as well as schematics on the integration of the two devices to establish the 2-µm optical coherent receivers for demodulating advanced modulated formats such as QAM or QPSK.

A ridge-waveguide photodetector is realised by use of four strained quantum wells on n-type InP substrate demonstrating a dark current as small as 2.55 nA at -1 V. A photoresponse of 0.38 A/W turns to be almost in-sensitive to the reverse bias voltage at the wavelength of 2 µm. Benefitting from the small area and thin active region of the device, a 3dB- cut-off frequency up to 12.9 GHz has been achieved. The 10 Gbit/s eye diagram tested on the packaged device shows an open eye as well as degraded SNR due to the low coupling efficiency of the waveguide geometry window as well as the thermal noise under high voltage directly biased on the parallel resistance in the package. To solve this natural problem of the waveguide type quantum well photodetector, a spot converter with a taper structure would be useful to address the mode mismatch between the small acceptable aperture of the detector and relative large spot size of the single mode fibre. As a result, a higher light coupling efficiency corresponding to larger SNR could be expected.

A high-speed surface-normal photodiode based on strain-relaxed $In_{0.72}Ga_{0.28}As$ sandwiched by AlInGaAs cap layer has been fabricated on n-doped InP substrate. A parabolic grading scheme was applied on the buffer layer to accommodate the lattice mismatching between the intrinsic layer and the substrate in the thickness of 0.5 micron to reduce the total epitaxial growth time and thus the cost. An unintentional background doping level of 1×10^{15} cm^{-3} in the centre indicates the threading location defects have been mainly suppressed as deduced from the CV measurement on large

mesas with diameters varying from 100 to 500 µm. By optimizing the thermal control of passivation as ramping from room temperature (20 °C) until the normal deposition temperature of 300 °C, the leakage of 50-µm diameter mesa has been suppressed to ~0.5 µA displaying a dark current density level comparable to the commercial products. The small signal characterization of the device shows that the RF bandwidth reaches up to around 10 GHz. In addition, with the photoresponse up to ~1 A/W from the large round-circle aperture and aluminium coating on the tilted facet of the angled fibre in the module, an error-free (EBR≤10^{-9}) eye pattern characterized at the modulation speed of 10 Gbit/s has been achieved for the packaged photodetector even at the input power down to -9.9 dBm. With the technical assitance from the package group in Tyndall, package modules of all the photodiode devices have been optimically designed as well as assembled for the system test applications.

According to the evaluated characters of the surface-normal type photodetector, a 2 µm balanced photodiode was then fabricated based on the same epitaxial layer structure of the surface-normal high speed photodiode on the SI substrate by serially connecting two photodiodes in the way of n-p-n-p. A dry-etching scheme of etching through the intrinsic layer as well as the n contact region in the same process following the first pre-etching to form a larger size mesa on the top of n-contact layer was utilized to avoid the potential failure of the sidewall passivation by using the same layer of silicon-dioxide hard mask within the two dry-etch steps. For the single mesa of the paired balanced photodiode (diameter-50 µm), the leakage is ~11 µA acceptable in the system application mainly focusing on the SNR character while the photoresponsivity is 1.2 A/W due to the unexpected over-thick intrinsic absorption layer. To eliminate the potential leakage/extra charge generation resulting parasitic capacitance due to the surface roughness and additional doping during the dry-etch process, a selective wet etching following the depth-optimized dry etching should be introduced to make sure that the finial position can be just stopped at the top surface of the semi-insulating substrate.

By use of the large spot size diluted waveguide, an optical hybrid at 2 µm has been fabricated based on the 4×4 Multimode Interference (MMI) coupler structure. 4 pairs of InGaAsP/InP created a waveguide with a mode size of more than 3 µm while maintaining the single mode character with the ridge width of 4 µm and etching depth of 5.5 µm. Benefitting from the large acceptance window of this kind of waveguide,

the coupling loss between the waveguide and the lens-ended fibre is less than 0.9 dB per facet. Considering the self-imaging properties of the MMI waveguide, the device length has been optimized around 1629 µm with the width of 32 µm to obtain an acceptable power imbalance for both polarization status. The waveguide width was adiabatically tapered from 4 µm to 3.5 µm to filter other high- order modes and tapered back to 4 µm at the input of the MMI waveguide to provide a larger imaging tolerance. To accommodate those deviations during the fabrication and simulation, samples with varied length within 1629-60 µm and 1629+60 µm were adopted into the masks design.

   With the monolithic integration of MZI combining 1×2 MMI and the delay line with the hybrid device, phase-related transmission spectrum from each output port was then characterized by delivering the broad band light from 2 µm TDFA into the test structure and visualizing by OSA at each of the output ports through lensed-ended fibre with specific design at this wavelength. By fitting the test results with the transmission function of 90° optical hybrid, an estimated CMRR of more than 15.6 dB, phase error of ± 10° from the quadrature condition, and excess loss of 2.2 dB involving the MZI are deduced for the optimum device with the length of 1644 µm. In the future, increasing the effective index-refractive index difference relative to the substrate as well as shrinking the width of the multimode waveguide should be considered on the optimizations regarding the material and mask design to minimize the power imbalance and phase deviation errors.

6.2 Further work

We can realize the coherent receiver at 2 µm wavelengths based on the two above-mentioned devices by directly assembling the optical hybrid and the balanced photodiode in one package module with the consideration of light coupling between the passive and active devices as well as electrical connection within and outside the package module.

As it is shown in Fig. 6.1, the ceramic with electrical circuits patterns would be first glued on the heat sink using silver epoxy then followed by the fixing of the high-speed SMA connectors in the same method. Two pairs of serially-connected photodiodes would be vertically set on the ceramics with suitable contact to the circuits. Then, the hybrid can be placed adjacent to the illumination window of the balanced photodiodes with the flat-facet fibre array at another input end (from the left out of the region of Fig. 6.1). After optimizing the coupling efficiency as well as the output balance of the hybrid device, all of the passive components would be glued on the same submount by using UV-sensitive epoxy. A metal protection cell would enfold all of the assembled parts to maintain the device stability as well as protect against the risk of breakage during other operations around the devices.
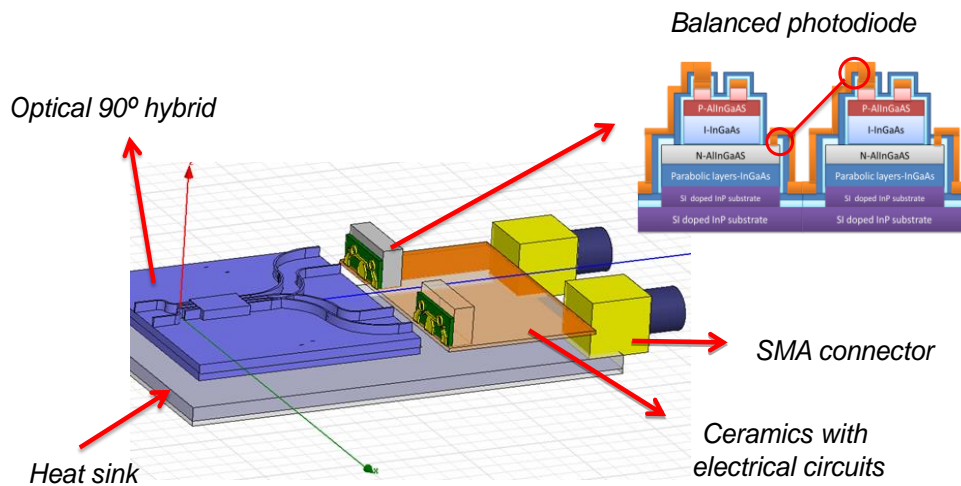
Figure 6.1: *Schematic of the package module for the 2 µm optical coherent receiver.*

For the light coupling between the balanced photodiode and the output waveguide of the hybrid, vertically setting the active devices could help to obtain the optimum

coupling by taking advantage of the large absorption aperture (diameter: 20 µm ~30 µm) of the surface normal photodetector as well as the large-size light spot from the output of the diluted waveguide (Fig. 6.2). High accurate alignment between the hybrid and photodiodes by use of the light coupling system in fine steps is necessary to get the best balancing point between the output electrical signals of all the photodetectors.

A transfer step needs to be concerned to achieve the rotated connection between the detector and the ceramics. The balanced photodetectors would be fixed on a small sub-mount, which has the transmission line bended to the attached surface matching with the contact points of the package ceramic circuits underneath. Direct wire-bonding would be used for the connection between the coplanar electrodes of the device and the transmission line of the small submount. In addition, more attention needs to be paid for the connection of the small submount and the following ceramics, such as the potential short circuit due to the flowing of silver epoxy, flatness after the soldering, etc..
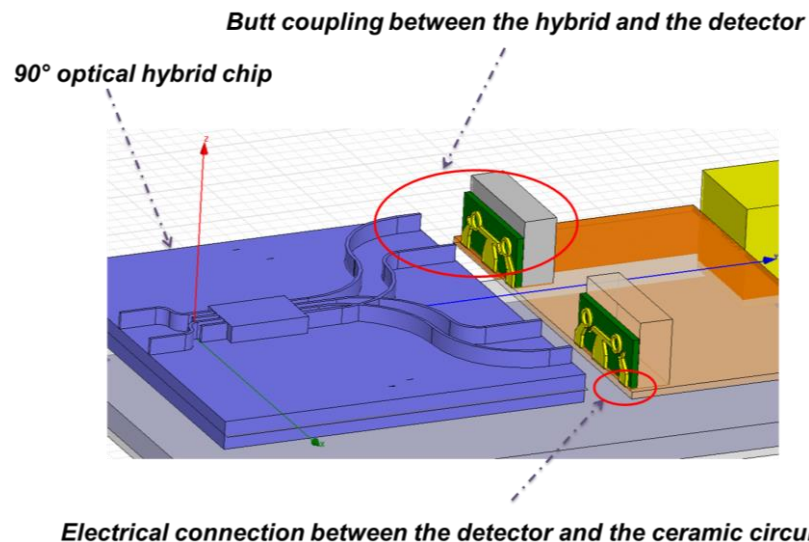
Figure 6.2: *Schematic for the light coupling and electrical connection inside the 2µm optical coherent module.*

For the ceramic circuits, the Direct Current (DC) and Radio Frequency (RF) signal paths should be isolated due to the static-voltage-biased source and high speed output characters of the detector in the serially paired balanced photodiode. From Fig. 6.3, a

bias-T is used to separate the voltage bias and high speed output. The resistance would protect the RF signal but let the DC bias go through while the capacitance would limit the transmission of the DC bias but let the high speed output pass through. This structure can be designed and fabricated on a ceramic base or integrated on the same semiconductor chip as it is shown in Fig. 6.3. In order to suppress the electrical reflection from the device side, the matching resistance of R_L could be 100 ohm in parallel with each of the detector so that the final effective impedance approaches to the 50 ohm microwave transmission line. While, the effective bandwidth of the whole packaged structure is approximated to half of the single photodiode due to that the total effectivecapacitance would be the double of one single photodiode from the view of the output port [1].
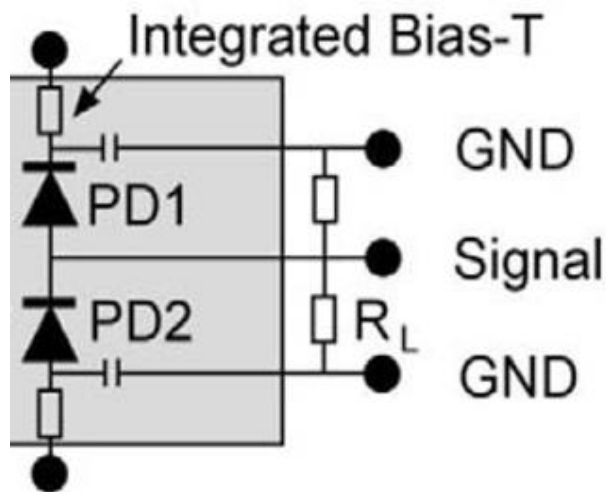
Figure 6.3: *Schematic for the ceramic circuits inside the coherent receiver package module* [1].

6.3 References

[1] H. G. Bach,"Ultra-broadband photodiodes and balanced detectors towards 100 Gbit /s and beyond," in *Optics East*, *International Society for Optics and Photonics*, 2005.

Appendix

1. Process flow for the high speed surface normal photodiode at 2 μm wavelengths

Wafer:

Type 2 on N-doped substrate- A quarter wafer,

Mask:

HIGHSPEEDPDMODEGAP1

1. Photo-lithography (Layer 1: Ring-metal)

□ Clean the mask

□ Clean and bake the wafer on the hot plate at >100 °C for more than 5 mins

□ Blow dry with N_2 gas

□ Spin on HMDS at 4000 rpm for 60 s

□ Spin on AZ5214E at 4000 rpm for 60 s

□ Edge bead removal EBR [wipe paper + acetone]

□ Soft bake on hotplate at 100 °C for 50 s

□ Exposure : Machine–MA1006, Vacuum contact, 2 s

□ Reverse bake on hotplate at 120 °C for 1 min 45 s

□ Flood exposure: 25 s

□ Develop with developer MF 26A for 22 s. A few seconds more if it is not clear.

□ Rinse with DI and dry with N_2 gun

□ Use O_2 plasma Asher for 2~3 mins at 50 W or 100 W

2. Flat p-metal evaporation

□ BOE: DI (1:10) dip for 10 s before p-metal evaporation.

□ Evaporation of Ti:Au=20:320 or Ti: Pt: Au =30: 50: 300

3. P-metal lift-off

□ Leave the sample in 1165 at 90 °C for at least half an hour

□ Lift-off

□ DI rinse + N_2 blow dry

4. P-metal annealing

□ Anneal at 420 °C for 3~5 mins at the neck of furnace (1.5 sccm - 5% H_2 / 95% N_2)

□ Anneal at 420 °C for 5 mins at the middle of furnace (1.5 sccm - 5% H_2 / 95% N_2)

  Thermal couple readout was 390~400 °C during annealing

□ TLM test

5. Wet etch – Removal of 100 nm- InGaAs

□ First check the metal thickness with profiler.

  Thickness: sample-340~400 nm, average-370 nm; silicon test piece-360 nm.

□ H_3PO_4: H_2O_2: H_2O = 1:1:8 wet etch for more than 5 s.

  Make sure it is over-etched to 150 nm.

□ Check the etched thickness with profiler.

  Thickness of Medal+ etched contact: 507~522 nm, average: 515 nm

  Thickness of etched contact: 145 nm, Time: 15 s, Etch rate: 9~10 nm/s

□ TLM test

6. SiO_2 hard mask deposition

□ Standard SiO_2 PECVD with recipe HFSIO. Include 3~4 Si monitor pieces.

□ Aimed thickness: 550 nm, Deposition time: 16 mins, Speed: 34.4 nm/min

□ Test the thickness

  Real thickness: 570 (Centre) to 590 (Edge) nm on the Si test piece

  Time: 16.5 mins, Deposition rate: 35.15 nm/min

7. Photo-lithography (Layer 2: Mesa definition)

□ Clean the mask

□ Clean and bake the wafer on the hot plate at >100 °C for more than 5 mins

□ Blow dry with N_2 gas

□ Spin on HMDS at 4000 rpm for 60 s

□ Spin on S1813 at 4000 rpm for 60 s

□ Edge bead removal (EBR) [wipe paper + acetone]

□ Bake on hotplate at 115 ˚C for 2~3 mins

□ Expose with MA1006: Vacuum contact, 7 s,

□ Develop in MF319 for 20 s

□ DI rinse

□ Blow dry with N_2 gas

□ Oven baking at 90 ˚C for 30 mins

□ Use O_2 plasma Asher for 60 s at 50 W or 100 W

8. ICP – SiO_2 etch

□ Use CHF_3/CF_4 plasma in STS ICP system

□ Recipe: OXIDEETCH

□ Aimed etch thickness: 550 nm, Time: 2 mins,

   Etch rate: 250~280 nm/min

□ Select several points on the wafer with no PR and Si test piece.

   Check the etched thickness, Real etch thickness: 570 nm

   Average time: 2 mins+30 s, Etch rate: 285 nm/min

9. Remove PR

□ O_2 plasma Asher for 2~3 minute at 50 W or 100 W.

□ Dip in solvent 1165 at 90 °C for at least half an hour.

   (Repeat the last two steps several times until it is fully cleaned).

□ DI rinse

□ Check the left SiO_2 thickness with the profiler.

□ Calculate the SiO_2 etch rate with the protection of PR:

   Thickness of SiO_2 left: 605 nm (sample) and 580 nm (InP test piece).

10. AlInGaAs and InGaAs etch (dry and wet etch)

□ $Cl_2/CH_4/H_2$ plasma in Oxford ICP system.

□ Recipe: Hua etch recipe.

□ Aimed etch thickness: 2.6~3 microns.

  Etch rate: 0.825-0.85 micron/minutes for InP

□ Test the etch thickness with profiler:

Remember to test the thickness of SiO_2 and remove it every time!

Real etched thickness+SiO_2 hard mask:

2.83 (Centre mesa) ~ 3 microns (Edge TLM).

Time: 4 mins+38 s for sample, 2 mins+20 s for InP.

□ Record the thickness of SiO_2 after dry etch: 170 nm (sample), 282 nm (InP test piece)

Etch rate: 97 nm/min.

□ Calculate the etched thickness and eth rate:

Real etch thickness:

Sample - 2.66 (centra mesa)~2.83 microns (edge TLM), InP test piece-2.62 microns

Etch rate:

Sample - 591 (centra mesa)~628 nm/min(edge TLM),

InP test piece-1.05 micron/min

Surface roughness: Sample-50~60 nm,

□ Dip in diluted BOE (BOE:DI=1:4) for 5 s to remove the oxidation on the sidewall.

□ Dip in H_3PO_4: H_2O_2: H_2O = 1:1:8 for 5 s to remove the polymer on the sidewall

and polish the surface due to dry etch.

Surface roughness: nearly the same as the case before wet etch

11. Strip SiO_2 hard mask

□ Diluted BOE (BOE:DI=1:4) for tens of seconds.

Make sure the etch rate then add 10 s at each etch step.

Etch rate: 2 or 3 nm/s (10 nm/s at first time). If use pure BOE, the speed is 9 nm/s.

□ Test the thickness (Sample and Si test piece).

Real etch thickness:

Sample-2.77 (centre mesa) ~ 2.99 microns (Edge TLM), InP-2.61 microns

Time:

Sample-2 mins+5 s. InP-4 mins.

SiO_2 etch rate: 3 nm/s

Sheet resistance orders: 10^{-8}~10^{-6}

Roughness: 40 nm

12. Deposit SiN_x and SiO_2 with PECVD

□ Load sample at 20 °C then ramp to 300 °C with 4 piece of Si test piece.

□ Recipe: standard MFSIN.

□ Aimed thickness:

   SiN_x-100 nm, SiO_2-100 nm

   Deposition Time: SiN_x-10 mins, SiO_2-2 mins+51s

   Speed: SiN_x-10 nm/min, SiO_2-35 nm/min

□ Test the thickness (Wafer and Si test piece).

   Temperature: SiN_x-250 °C, SiO_2-275 °C

   Real deposition thickness: SiN_x-99 nm, SiO_2-103 nm

   Time: SiN_x-10 mins, SiO_2-2 mins+51 s

   Speed: SiN_x-10 nm/min, SiO_2-35 nm/min

13. BCB spinning and curing

□ BCB- CYCLOTENE 3022 - 57

   Non-photosensitive (Thickness: 8.0 micron after spinning at 2500 rpm and curing)

□ Dehydrate bake on hotplate at 150 °C for more than 10 mins.

□ Spin on adhesion promoter (AP3000) at 300 rpm for 5 s then at 3000 rpm for 20 s

□ Spin on BCB at 500 rpm for 7 s then at 2000 rpm for 40 s,

□ EBR using T1100 (BCB solvent).

   Ensure that the backside of the wafer is completely cleaned.

□ Put the sample which has a silicon piece underneath on the centre of the silicon

   carrier in the oven.

□ Pump down the chamber to a few mili-torr.

□ Isolate the chamber and vent it with N_2 to 0.8 ATM. Then, start the full cure process.

□ Ramp from 150 to 250 °C by 25 °C per step.

□ Switch off the oven when the temperature drop to the case smaller than 150 °C.

   If it is necessary, leave the sample in the oven for over-night cooling.

   Use the profiler to figure out the step after planarization

   Target-500 nm minimum. Maximum-600 nm.

□ Record image

14. BCB etch-back

□ ICP etch by using STS machine

Chemistry: SF_6+O_2, Recipe: BCB ETCH

Etch time: 6 mins+35 s, Etch rate: Around 800 nm/min

□ Record image

15. Photo-lithography (Layer 3: Oxide opening)

□ Clean the mask

□ Clean and bake the wafer on the hot plate at >100 °C for more than 5 mins

□ Blow dry with N_2 gas

□ Spin on HMDS at 4000 rpm for 60 s

□ Spin on S1813 at 4000 rpm for 60 s

□ Edge bead removal (EBR) [wipe paper + acetone]

□ Bake on hotplate at 115 ˚C for 3 mins

□ Expose with MA1006: Vacuum contact, 6.7 ~7 s,

□ Develop in MF319 for 16~25 s

□ DI rinse

□ Blow dry with N_2 gas

□ Oven baking at 90 ˚C for 30 mins

□ Use O2 plasma Asher for 2~3 mins at 50 W or 100 W.

16. BCB Etch

□ ICP etch by using STS machine

□ Chemistry: SF_6+O_2, Recipe: BCB ETCH

□ Record image

Etch time: 1 min+30 s

Etch rate: Around 800 nm/min

17. SiN_x and SiO_2 etch.

□ CF_4 plasma with Asher.

Not etch though conditional run was operated for 18 mins.

It seems work if use10 mins O_2 plasma first.

Should use BOE to remove the SiO_2 first due to that CF_4 would not etch SiO_2.!!

□ Test the thickness. (Wafer and Si test piece).

   Time: more than 15 minutes

   Power: 100 W

   Etch rate: not stable but smaller than 25 nm/min.

18. Quick TLM measurement

   Only one TLM sample can be fully opened.

   Sheet resistance orders: 10^{-5}

19. Remove PR:

□ O_2 plasma Asher for 2~3 minute at 50 W or 100 W.

□ Solvent 1165 in 90˚C for at least half an hour.

   Repeat the last two steps several times until it is fully cleaned.

   If still not clean, use woollen stick to gently remove the left PR while keeping the

   sample at solvent 1165.

□ DI rinse and dry with N2.

20. Photo-lithography (Layer 4: Bond-metal)

□ Clean the mask

□ Clean and bake the wafer on the hot plate at >100 °C for more than 5 mins

□ Blow dry with N_2 gas

□ Spin on HMDS at 4000 rpm for 60 s

□ Spin on AZ5214E at 4000 rpm for 60 s

□ Edge bead removal (EBR) [wipe paper + acetone]

□ Soft bake on hotplate at 100 degree for 50s

□ Exposure with mask aligner MA1006: Vacuum contact 2s

□ Reverse bake on hotplate at 120 °C for 1min 45s

□ Flood exposure for 25s

□ Develop with develop MF 26A: 22s. A few seconds more if it is not clear.

□ Rinse with DI and dry with N2 gun

□ Use O2 plasma Asher for 2~3mins at 50W or 100W.

21. Further window open

   Hard bake should be carried on in the oven at 90 °C for at least half an hour first.

□ Diluted BOE (BOE:DI=1:4) dip.

   Time: 10 s first to remove the SiO_2.More than 2mins to remove the SiN_x

   Etch rate:

   SiN_x—1 nm/s, SiO2—2 to 3 nm/s

□ Record images.

Note: This step could be after CF_4 plasma if some PR is still left.

22. P-metal evaporation with 360° rotation

□ BOE: DI (1:10) dip for 10 s

   Not necessary after further window opening with diluted BOE

□ Evaporation of Ti:Au=20:320.

23. P-metal lift-off

□ Leave in 1165 solvent at 90 °C for half an hour or leave it overnight on the hotplate
   switched-off.

   If it is still not clean, use woollen stick to gently remove the left PR while keep the
   sample at the solvent of 1165.

□ Lift-off

□ DI rinse + N_2 gas blow dry

24. Backside N-metal evaporation

□ Polish the wafer backside first if necessary. Fix the wafer top side on a glass with
   black wax. Dip the back side in HCL for 2 or 3 mins to make the backside clean
   and smooth.

□ Evaporation of Ti:Au=20:320 or N metal- Au: Au: Ge: Ge: Au: Au: Ni: Ni: Au: Au.

□ Remove the sample from the glass and make it clean with TCE.

□ DI rinse + N_2 gas blow dry

25. Quick IV and CV measurement

   Windows had been opened within most of the area of the wafer. The dark current

is ok though some area leakage is close to the order of mA.

Capacitance is 0.32 pF for the mesa with 60 µm diameter.

26. Substrate thinning

□ Polish the wafer backside

□ Thin the substrate with bromine and clean with methanol

□ Aimed thickness: 120 microns,

Time: 8mins. Etch rate: 30~40 micron/min

Real left thickness:120~140 nm, Time:14 mins, Speed:16 microns/min

27. Backside N-metal evaporation

□ BOE: DI (1:10) dip for 10 seconds

□ Evaporation of Ti:Au=20:320 or N metal- Au: Au: Ge: Ge: Au: Au: Ni: Ni: Au: Au.

□ Remove the sample from the glass and make it clean with TCE.

□ DI rinse + N_2 blow dry

28. Cleave and test

□ Quick IV test on the wafer for selecting the good bars

□ Quick CV test on the wafer to estimate the maximum working speed

□ Cleave single devices from the bars.

□ IV test to select the best devices for packaging.

2. Process list for the balanced photodiode at 2 μm wavelengths

Material:

Type-2 on semi-insulating (SI) substrate

Mask:

2 micron Tyndall BPD Plate 1 and 2

1. Photo-lithography (Layer:P METAL L0)

□ Clean mask with 1165 (90 °C) and then dip in mask cleaning sink (H_2SO_4 and H_2O_2).

□ Clean the mask with N2 gas

□ DI rinse the wafer

□ Machine-MA1006; Photoresist-1 layer of AZ5214E (Image reverse)

□ Clean and bake wafer on hot plate (>100 °C, >5 mins)

□ Clean the wafer with N2 gas

□ Spin on HMDS at 4000 rpm for 60 s

□ Spin on AZ5214E at 4000 rpm for 60 s

□ EBR [wipe paper + acetone]

□ Soft bake on hotplate at 100 °C for 50 s

□ Exposure with mask aligner MA1006: Vacuum contact, 2s

□ Reverse bake on hotplate at 120 °C for 1 min 45 s

□ Flood exposure for 25 s or longer

□ Develop with developer of MF 26A for 22 s. A few seconds more if it is not clear.

□ Rinse with DI and dry with N_2 gun

□ Use O_2 plasma Asher for 2~3 mins at 50 W or 100 W to clean

2. Flat P-metal evaporation

□ BOE: DI (1:10) dip for 10 s

□ Flat evaporation of Ti: Pt: Au =20: 50: 500

3. P-metal lift-off

□ Left in 1165 at 90 °C for at least half an hour

□ Lift-off

□ DI rinse + N_2 blow dry

□ Observe under the microscope and record the image

Thickness: 619 nm, surface roughness: 81.99 nm

4. P-metal annealing

□ Anneal at 420 °C for 3 minutes at the neck of furnace (1.5 sccm - 5% H2 / 95% N2)

□ Anneal at 420 °C for 5 minutes at the middle of furnace (1.5 sccm - 5% H2 / 95% N2)

Thermal couple readout was 390 ~ 400 °C during annealing

5. Wet etching – Removal of 100 nm InGaAs

□ First check the metal thickness with profiler.

Thickness: 585.93~590 nm, surface roughness: 173 nm

□ Dip in H_3PO_4: H_2O_2: H_2O = 1:1:8 for more than 5 s.

Make sure it is over-etched to 150 nm.

□ Check the etched thickness with profiler.

Thickness of medal+ etched contact:

Sample: 808 nm (average)

Thickness of etched contact:

Sample: 218-(centre ring)~200 nm (edge TLM)

Real Time: 20 s, Etch rate: 9~10 nm/s

□ TLM test

Sheet resistance order: $2{\sim}3{\times}10\text{-}4$ Ω/cm^2

6. SiO_2 hard mask deposition

□ Standard SiO_2 PECVD with recipe HFSIO. Include 3~4 Si monitor pieces.

□ Aimed thickness: >1200 nm, Deposition Time: > 35 mins,

Deposition rate: 34.4 nm/min~32 nm/min

□ Test the thickness

Real thickness: 1263.4 nm; Real Time: 40 mins; Deposition rate: 31.59 nm/mins

After this, for the semi-insulating (SI) substrate sample, remember to sputter metal on the backside of the substrate (Total-90s)

7. Photo-lithography (Layer: N MESA L1)

□ Clean mask with 1165 (90 °C) and then dip in mask cleaning sink.

□ Clean the mask with N_2 gas

□ DI rinse the wafer

□ Prebake at >100 °C for more than 5 mins.

□ Clean the wafer with N_2 gas

□ Spin on HMDS: 4000 rpm for 60 s

□ Spin on S1813: 4000 rpm for 60 s

□ EBR [wipe paper + acetone]

□ Bake on the hotplate at 115 °C for 2 mins.

□ Expose with MA1006: Vacuum contact, 6 s or with MA06, 10 s

□ Develop in MF319 for 14~15 s, which should be divided by several steps

□ DI rinse

□ Blow dry N_2.

□ Use O_2 plasma Asher for 60 seconds at 50W or 100W

Resolution:

If it is necessary to use O2 plasma to clean the surface, it is better to be carried on after hard baking.

8. ICP – SiO_2 etching

□ CHF_3/CF_4 plasma in STS ICP system

□ Recipe: OXIDEETCH

□ Aimed etch thickness: >1263.4 nm, Time: >4 mins+30s

Etch rate: 250~280 nm/min

□ Select several points on the wafer with no PR and Si test piece to check whether there is SiO_2 left.

□ Test the sample surface roughness.

Final etch time: 5 mins

9. Remove PR

□ O_2 plasma Asher for 2~3 minute at 50 W or 100 W.

□ Put in solvent of 1165 at 90 °C for at least half an hour.

　Repeat the last two steps several times until it is fully cleaned.

□ DI rinse

□ Check the left SiO_2 thickness with profiler.

　Real etch thickness: 1270 nm (Centre ring) ~ 1302 nm (Edge TLM)

□ Calculate the SiO_2 etch rate.

　Etching rate: 270 nm/min

10. AlInGaAs and InGaAs etch (dry etch)

□ $Cl_2/CH_4/H_2$ plasma in Oxford ICP system.

□ Recipe: InP 4 micron JOC EF or Hua recipe

□ Aimed etch thickness: 2.5~3 microns

□ Estimated etch time: 3 mins~3 mins+30s, Start at 2 mins+30 s, Add 30 s, then add another 30 s.

　Estimated etch rate: 0.5~1.0 micron/min, 90 nm/s (PEVCVD SiO2)

□ Test the etch thickness with profiler:

　Remember to test the thickness of SiO2 substrate every time!

□ Test the surface roughness after etch:

11. Photo-lithography (Layer: I MESA L2)

□ Clean mask with 1165 (90 ˚C) and then dip in mask cleaning sink.

□ Clean the mask with N_2 gas

□ DI rinse the wafer

□ Prebake on >100 ˚C for more than 5 mins

□ Clean the wafer with N_2 gas

□ Spin on HMDS: 4000 rpm for 60 s

□ Spin on S1828: 2000 rpm for 60 s

□ EBR [wipe paper + acetone]

□ Bake on the hotplate at 115 ˚C for 2 mins

□ Expose with MA1006:Vacuum contact, <=18 s

□ Develop: MF319 for 35~47 s, which should be divided by several steps

□ DI rinse

□ Blow dry by N_2 gas

□ Oven baking at 90 ˚C for 30 mins

□ Use O_2 plasma Asher for 60 s at 50 W or 100 W

Resolution: < 2 μm

If it is necessary to use O2 plasma to clean the surface, it is better to be carried on after hard baking.

12. ICP-SiO2 etching

□ CHF3/CF4 plasma in STS ICP system

□ Recipe: OXIDEETCH

□ Aimed etching thickness: >600 nm, Time: 2mins+45s

Etching rate: around 250~280 nm/min

□ Select several points on the wafer with no PR and Si test piece to check whether there is SiO2 left

13. Remove PR

□ O2 plasma Asher for 2~3 minute at 50W or 100W.

□ Leave in solvent of 1165 at 90 °C for at least half an hour.

Repeat last two steps several times until it is fully cleaned.

□ DI rinse

□ Check the SiO2 thickness with profiler.

□ Calculate the SiO2 etching speed with the protection of PR:

□ Test the sample surface roughness.

14. Etch of AlInGaAs and InGaAs (dry etch and wet etch)

□ Cl_2/CH_4/H_2 plasma in Oxford ICP system.

□ Recipe: InP 4 micron JOC EF

□ Aimed etching thickness: 2.6~3 microns (N contact mesa). >2.4 microns (Intrinsic mesa), Estimated time: > 3 mins

for sample, Start at 2 mins+30s, then another 30 s

Esitmated etching rate:

0.825-0.85 micron/minutes (Typically 0.8-0.9 micron per minutes for InP),

0.5~1.0 micron/min (sample on SI substrate),

90 nm/s (PEVCVD-SiO$_2$)

□ Test the etch thickness with profiler

□ Record thickness of SiO$_2$ after semiconductor etch

□ Quick dip in diluted BOE (BOE: DI=1:4) for 5 s to remove the oxidation on the sidewall and N contact surface.

□ Dip in H$_3$PO$_4$: H$_2$O$_2$: H$_2$O = 1:1:8 for 15 s to remove the polymer on the sidewall and polish the side wall and bottom surface.

□ Dip in HCl:H$_3$PO$_4$=1:4 for more than 1 min to remove part of InP to making sure that the substrate is fully isolated.(This step could be moved after the N metal deposition)

15. Strip SiO$_2$ hard mask

□Diluted BOE (BOE:DI=1:4) for tens of seconds.

Make sure the etch rate then add 10 s at each step.

Etch rate: 2 or 3 nm/s (10 nm/s at first time).If use pure BOE, the speed is 9 nm/s.

□Test the thickness.

□Test the sample surface roughness

16. Photo-lithography (Layer: N METAL N L3)

□ Clean mask with 1165 (90 °C) and then dip in mask cleaning sink.

□ Spin on HMDS at 1000 rpm for 1 min

□ Spin on LOR10A at 1000 rpm for 1 min

□ EBR [wipe paper + acetone]

□ Soft bake at 50 °C for <5 mins

□ Spin on HMDS at 2000 rpm for 60 s

□ Spin on AZ5214E at 2000 rpm for 60 s

□ Soft bake on hotplate at 90 °C for 1 min

□ Spin on HMDS at 2000 rpm for 60 s

□ Spin on AZ5214E at 2000 rpm for 60 s

□ Soft bake on hotplate at 90 °C for 1 min+30 s

□ Spin on HMDS at 2000 rpm for 60 s

□ Spin on AZ5214E at 2000 rpm for 60 s

□ EBR [wipe paper + acetone]

□ Soft bake on hotplate at 90 °C for 3 mins

□ Exposure with mask aligner MA1006: Vacuum contact，1.8 s

□ Reverse bake on hotplate at 120 °C for 2 mins.

□ Flood exposure: 70 s

□ Develop with developer MF 26A for 25~30 s.

□ Observe at the microscope to check

□ Develop with MF319 for 1 min, 10 s more if that is not so clear.

□ Use O_2 plasma Asher for 2~3 mins at 50 W or 100 W.

17. N metal evaporation

□ BOE: DI (1:10) dip for 10 s before n-metal evaporation!!

□ Flat evaporation of n metal

18. N-metal lift-off

□ Leave in 1165 at 90 °C for at least half an hour

□ Lift-off

□ DI rinse + N_2 blow dry

□ Observe under the microscope and record the image

□ Dip in $HCl:H_3PO_4=1:4$ for more than 1 min to remove part of InP to make sure
the substrate is fully isolated.

19. Deposit SiNx with PECVD

□ Load sample at 20 °C then ramp to 300 °C for deposition
Real load temperature: 30~35 °C,

□ Recipe: mfsin, Temperature: 300 °C

□ Aimed thickness: ~190 nm,
Deposition Time: 19 min, Speed: ~10 nm/min,

□Test the film thickness
Real deposition thickness:
SiNx-169 nm~159 nm (Edge alignment mark)
Time: 16 mins, Average rate: 10.25 nm/min

20. Photo-lithography (Layer: N WINDOW L4)

□ Clean mask with 1165 (90 °C) and then dip in mask cleaning sink.

□ Clean the mask with N_2 gas

□ DI rinse

□ Prebake at >100 ˚C for a 2 or 3 minutes

□ Clean the wafer with N2 gas

□ Spin on HMDS at 4000 rpm for 60 s

□ Spin on S1828 at 1000 rpm for 60 s

□ EBR [wipe paper + acetone]

□ Bake on hotplate at 115˚C for 5 minutes+10s

□ Expose (MA1006): Vacuum contact, 30 s,

□ Develop: MF319 for 23~25 s

□ DI rinse

□ Blow dry N2

□ Oven baking: 90˚C for 30 minutes

□ Use O2 plasma Asher for 2~3mins at 50 W or 100 W.

21. SiNx etch

□ Use CF_4 plasma Asher.

□Test the thickness. (Wafer and Si test piece).

   Etch rate: 20~70 nm/min.

□ Diluted BOE (BOE:DI=1:4) or BOE dip.

22. Remove PR:

□ Use O_2 plasma Asher for 2~3 mins at 50 W or 100 W.

□ Dip in the solvent of 1165 in 90 ˚C for at least half an hour.

   Repeat the last two steps several times until it is fully cleaned.

   If it is still not clean, use woollen stick to gently remove the left PR while keep the

   sample at the solvent of 1165.

□ DI rinse and dry with N_2 gas.

   Repeat from Step 20 to Step 22. The mask layer should be (Layer: P WINDOW L5),

   Adjust the exposure time to be 20 s and then reduce the development time as well.

23. Photo-lithography (Layer: BOND PAD)

□ Clean mask

□ Spin on HMDS at 1000 rpm for 1 min

□ Spin on LOR10A at 1000 rpm for 1 min

□ EBR [wipe paper + acetone]

□ Soft bake at 50 °C for 5 mins

□ Spin on HMDS at 2000 rpm for 60 s

□ Spin on AZ5214E at 2000 rpm for 60 s

□ Soft bake on hotplate at 90 °C for 1 min

□ Spin on HMDS at 2000 rpm for 60 s

□ Spin on AZ5214E at 2000 rpm for 60 s

□ Soft bake on the hotplate at 90 °C for 1min+30s

□ Spin on HMDS at 2000 rpm for 60s

□ Spin on AZ5214E at 2000 rpm for 60s

□ EBR [wipe paper + acetone]

□ Soft bake on hotplate 90 °C for 3mins

□ Exposure with mask aligner MA1006: Vacuum contact, 1.8s

□ Reverse bake on hotplate at 120 °C for 2mins.

□Flood exposure: 70 s

□Develop with develop MF 26A: 25-30 s. (Very clear under-cut)

□ Observe at the microscope to check

□ Develop with MF319 for 1 min, 10 s more if that is not so clear.

□ Use O2 plasma Asher for 2~3 mins at 50 W or 100 W.

24. Bond metal evaporation in 360° rotation

□ Diluted BOE: DI (1:10) dip for 10 s.

□ 360° rotation evaporation of Ti:Au=20:500.

25. Bond-metal lift-off

□ Leave the sample in 1165 solvent at 90 °C for 0.5 hour or leave it overnight with the hotplate switched off.

□ DI rinse + N$_2$ blow dry

26 .Quick IV

□ Quick IV test to check the diode junction quality

3. List of publications

Journal:

- Nan Ye, Michael R. Gleeson, *et al*., "InP Based Active and Passive Components for Communication Systems at 2μm". *Journal of Lightwave Technology*, vol. 33, no. 5, pp.971-975. 2014. (cited by Nature Photonics)
- Nan Ye, Michael R. Gleeson, *et al.*, "InGaAs Surface Normal Photodiode for 2 μm Optical Communication Systems". *Photonics Technology Letter,* vol. 27, no. 14, pp.1469-1472, 2015.
- Hua Yang, Nan Ye, R. Phelan, *et al.*, "Butterfly Packaged High-Speed and Low Leakage InGaAs Quantum Well Photodiode for 2000nm Wavelength Systems". *Electronics Letters*, vol. 49, no. 4, pp.281-282, 2013.
- Muhammad Usman Sadiq, Michael R. Gleeson, Nan Ye, *et al.*, "A 10 Gbit/s InP-based Mach-Zehnder modulator for operation at 2 μm wavelengths". *Optics Express*, vol. 23, no. 9, pp.10905-10913, 2015.
- Hongyu Zhang, Michael Gleeson, Nan Ye, *et al.*, "Dense WDM transmission at 2 μm enabled by an arrayed waveguide grating". *Optics letters*, vol. 40, no. 14, pp. 3308-3311, 2015.
- Hongyu Zhang, Niamh Kavanagh, Zhihong Li, Jian Zhao, Nan Ye, *et al.*, "100 Gbit/s WDM Transmission at 2 μm: Comparison Transmission Studies between Low-loss Hollow Core Photonic Bandgap Fiber and Solid Core Fiber". *Optics Express*, vol. 4, no. 23, pp.4946-4951, 2015.

Conference:

- Nan Ye, Michael Gleeson, *et al.*, "Demonstration of 90° Optical Hybrid at 2 μm Wavelength Range Based on 4×4 MMI Using Diluted Waveguide," in *European Conference on Optical Communications (ECOC)*, Cannes, France, 2014, p.2.14.
- Nan Ye, Michael Gleeson, *et al.*, "1×4 MMI Coupler Using Diluted Waveguide at 2μm," in *Compound Semiconductor Week*, Montpellier, France,2014.
- Nan Ye, Hua Yang, Michael Gleeson, *et al.*, "AlInGaAs surface normal photodiode for 2 μm optical communication systems," in *IEEE Photonics Conference (IPC)*, USA, 2015, pp. 456-459.
- Hua Yang, Nan Ye, *et al.*, "High speed AlInGaAs/InGaAs Quantum Well Waveguide Photodiode for Wavelengths around 2 microns," in *Indium Phosphide and Related Materials (IPRM), International Conference on IEEE.,* Santa Barbara, CA,USA, 2012, pp.221-224.
- Hongyu Zhang, Zhihong Li, Niamh Kavanagh, Jian Zhao, Nan Ye, *et al.*, "81 Gb/s WDM Transmission at 2μm over 1.15 km of Low-Loss Hollow Core Photonic Bandgap Fiber", in *European Conference on Optical Communications (ECOC)*, Cannes, France, 2014, p.5.20.
- Muhammad Usman Sadiq, Hongyu Zhang, Michael R. Gleeson, Nan Ye, *et al.*, "40 Gbps WDM transmission over 1.15 km HC-PBGF using the first InP-based Mach Zehnder modulator at 2 μm", in *European Conference on Optical Communication (ECOC)*, Valencia, Spain, 2015, pp. 1-3.
- J. Baig, B. Roycroft, J. O'Callaghan, C. Robert, N. Ye, M. Gleeson, *et al.*, "Quantum Well Intermixing in 2 μm InGaAs Multiple Quantum Well structures", *Conference on Lasers and Electro-Optics* (CLEO), Optical Society of America, 2016, pp. SM4R-4，.